Study of substorm onset processes in the magnetosphere and the ionosphere using satellite and ground-based observations

Heqiucen XU

Department of Electrical Engineering

Graduate School of Engineering

Nagoya University

2020

Acknowledgements

I would like to thank Professor Kazuo Shiokawa in Nagoya University for his patient and brilliant instruction to my five-year graduate course. I benefited a lot from his noble personality and wide knowledge in geophysics. I am grateful to Dr. Shin-ichiro Oyama for his great help in the research of high-latitude thermosphere. I really appreciate Dr. Yuichi Ostuka for his important advice in writing journal paper. I also thank Dr. Satonori Nozawa for his instruction in wind study at Tromsø, Norway. Many thanks for the help from Martinez-Calderon, Früahauff, Miyashita, Yamada, Asai, Nishioka and other staffs and classmates during my study life in Nagoya.

Special thanks to the members of review committee on this doctor thesis, Professor Kazuo Shiokawa, Professor Yoshizumi Miyoshi, Associate Professor Nozomu Nishitani, Professor Noriyasu Ohno, and Professor Tomohiko Watanabe.

Thanks to Professor Hui Li in Chongqing University, I learnt precious knowledge about electric machine which helps me a lot in my future career as an engineer. Friendly support from my senior Haiting in his laboratory also impressed me a lot. I am indebted to my mom and dad for their selfless and perennial care. I am full of gratitude to my wife Mumei and daughter Yuner for their spiritual support and continuous effort in our private life. I am also grateful for the encourage given by Claire in the past years.

SuperDARN is a collection of radars funded by national scientific funding agencies of Australia, Canada, China, France, Italy, Japan, Norway, South Africa, United Kingdom, and the United States of America. We are indebted to the director and staff of EISCAT for operating the facility and supplying the data. EISCAT is an international association supported by research organizations in China (CRIPR), Finland (SA), Japan (ISEE and NIPR), Norway (NFR), Sweden (VR), and the United Kingdom (STFC). We are indebted to Drs. H. Miyaoka and Y. Ogawa for operating the NIPR all-sky camera at Tromsø and supplying the data. We also thank the institutes who maintain the IMAGE Magnetometer Array. We used the IDL Geopack Dynamic Link Module (DLM) routines provided by H. Korth to run the Tsyganenko magnetospheric magnetic field model. This model was developed by N. A.

Tsyganenko. We thank Vassilis Angelopoulos for his helpful suggestions and Yukinaga Miyashita for his support in SPEDAS/TDAS operation. We acknowledge the NASA contract NAS5-02099 and V. Angelopoulos for the use of data from the THEMIS mission. We specifically acknowledge C. W. Carlson and J. P. McFadden for the use of ESA data and K. H. Glassmeier, U. Auster, and W. Baumjohann for the use of FGM data provided under the lead of the Technical University of Braunschweig and with financial support through the German Ministry for Economy and Technology and the German Center for Aviation and Space (DLR) under contract 50 OC 0302.

The wind data of FPI used in this paper are available at ISEE, Nagoya University. We thank Prof. Mike Kosch as the owner of the hut where the FPI is operated. The AU, AL, AE, Kp, Ap, and Dst indices were provided by the WDC for Geomagnetism at Kyoto University. The OMNI data were obtained from the GSFC/SPDF OMNIWeb interface. The HWM14 model is available online at Drob et al. [2015]. The online tool of SuperDARN data is hosted by the Virginia Tech SuperDARN group.

I am grateful for the support of the Leadership Development Program for Space Exploration and Research in Nagoya University. Most descriptions in Chapters 1-5 are based on the works of Xu et al. [2017a], Xu et al. [2017b], Xu et al. [2019a] and Xu et al. [2019b].

Abstract

Substorms are fundamental geomagnetic and auroral disturbances with time scales of 2–3 h. Among various substorm models, the location and mechanism of substorm onsets are still under debate. In this thesis, we focused on the onset mechanisms of substorms in the magnetosphere and the ionosphere, as well as how the Earth's upper atmosphere can be affected at substorm onsets. We analyzed data obtained from satellite and ground-based instruments, and applied various empirical models. The contents can be divided into the following four topics.

Firstly, we focused on the substorm onset mechanism in the magnetosphere. For the first time, we statistically studied severe magnetic fluctuations ($\sigma_B/\bar{B} > 0.5$, where σ_B and $\bar{B}$ are the standard deviation and the average value of magnetic field intensity during the time interval of the local proton gyroperiod) in the near-Earth magnetotail at 6–12 R_E, which may cause substorm-associated tail-current disruption. We used the magnetic field data with a sampling rate of 4 Hz obtained by the Time History of Events and Macroscale Interactions during Substorms E (THEMIS-E) satellite for 2013–2014. We identified 3322 severe magnetic fluctuation events, and found that their occurrence rates are 0.00312 %, 0.0312 %, and 0.0675 % at 6–8, 8–10, and 10–12 R_E, respectively in the near-Earth tail. These severe magnetic fluctuations occurred near the substorm onsets or during the expansion phase of substorms. We also found that the speed of plasma flow increases before the severe magnetic fluctuations. We discussed how both the inside-out and outside-in substorm models can explain these features.

Second, we investigated the spectral property of these severe magnetic fluctuations. We used the measurements of THEMIS-D and E for 2008–2018. Because magnetic field dipolarization is a signature of substorm onset, we further extracted 36 dipolarization events with severe magnetic fluctuations. We calculated the power spectral density (PSD) of magnetic fluctuations during these dipolarization events, and found that the steepness of the spectral slope increases with increasing frequency for almost all the events. We showed the average PSDs of magnetic fluctuations sorted by (a) the distance to the neutral sheet and (b) ambient magnetic field intensity.

In all groups, the slopes of average PSDs become steeper abruptly from below ~$10^{-1.3}$ Hz to above ~$10^{-1.3}$ Hz (0.05 Hz). We also see a clear increase of the slope at 0.05–0.1 Hz in case of larger ambient magnetic field intensity, implying that the magnetic fluctuations have a relatively strong power near the ion gyrofrequency and may contribute to the non-magnetohydrodynamics (non-MHD) effect in ion motion.

Thirdly, we focused on the ionospheric and thermospheric processes at substorm onsets. We studied the high-latitude thermospheric wind variations at local substorm onsets at Tromsø, Norway. We obtained four events, whose wind measurements were obtained at altitudes of 200–300 km by a Fabry-Perot interferometer (FPI). All events showed eastward increases of zonal winds at local substorm onsets. For meridional winds, these events showed southward increases except for those at midnight. The observed wind variations (< 49 m/s) were much smaller than the typical plasma convection speed in the auroral zone. Therefore, we speculate that the wind-induced ionospheric current at local substorm onsets does not provide strong feedback to the development of substorm expansion phase in the magnetotail. We then discussed the possible causes of the observed wind variations.

Finally, we also investigated the average winds in the thermosphere during geomagnetically quiet times. We used wind measurements for 2009–2015 obtained by the same FPI at Tromsø. On average, the zonal wind shows a westward increase before the midnight compared with winds expected from diurnal tides. A maximum speed of 100 m/s occurs at both the dusk and dawn sides. The meridional wind has a diurnal-tide structure with a minimum value of -130 m/s near the midnight. We also reported occasional large wind deviations (> 100 m/s) from the average winds even during geomagnetically quiet time. We then applied these quiet-time average winds to the previous event study in the third topic, and concluded that the substorm-associated winds with shorter time period are the main contributors to the observed thermospheric wind variations at local substorm onsets.

The results of these four topics indicate: (1) Substorm onset is unlikely to be caused by severe magnetic fluctuations in the near-Earth magnetotail or thermospheric wind variations at high latitudes, although we did not completely deny the scenarios of substorm onset by inside-out and magnetosphere-ionosphere coupling (MIC) substorm models. (2) At local substorm onsets, high-latitude thermospheric wind can be affected by various phenomena, and is dominated by substorm-associated energy input from the magnetosphere, such as plasma convection.

Contents

Chapter 1
Introduction

This chapter first reviews the history of substorm study and importance of the substorm onset mechanism. One controversy in various substorm models is the onset location of substorm. The popular considerations of substorm onset locations include the near-Earth region in the magnetotail, and the Earth's ionosphere at high latitudes. Severe magnetic fluctuations in the near-Earth magnetotail and thermospheric wind variations at high latitudes are two possible candidates to trigger substorm onset. This chapter introduces the research history of these two phenomena, and points out the importance of further investigation about them. At the same time, we note that it is necessary to study the influence caused by substorms, such as the ionospheric and thermospheric responses to substorm onset at high latitudes. Some contents in this chapter are based on Xu et al. [2017a, 2017b, 2019a, 2019b].

1.1 Auroral and Magnetospheric Substorms

Substorms, which are elementary geomagnetic and auroral disturbances with timescales of 2–3 hours, are first identified as the auroral substorm by Akasofu [1964]. The detailed description of substorms in that paper triggered a tremendous upsurge in related studies. As shown in Figure 1.1, Akasofu [1964] divided a whole auroral substorm into quiet, expansive and recovery phases, which consist of seven stages with different timescales. If the auroras in the polar region are free from activity for ~3 h, most of auroras around the midnight would occur as quiet and homogeneous auroral arcs. This is called the quiet phase (Figure 1.1a). The expansive phase (Figures 1.1b–1.1d) has three stages. A sudden brightening in one of the quiet auroral arcs with a length of few thousand kilometers at the midnight meridian would indicate the start of expansive phase. For most cases, such a brightening auroral arc would move to the polar region rapidly, and arrive at the poleward-most point near the midnight meridian. The poleward moving auroral arc during a stronger substorm typically arrives at higher geomagnetic latitude. In the recovery phase (Figures 1.1e–1.1f), the auroral arc which reaches at its poleward-most point would stay here

for ~10–30 min, and then start to recover equatorward. After Akasofu [1964], the growth phase of substorm was also found by e.g., McPherron [1970].

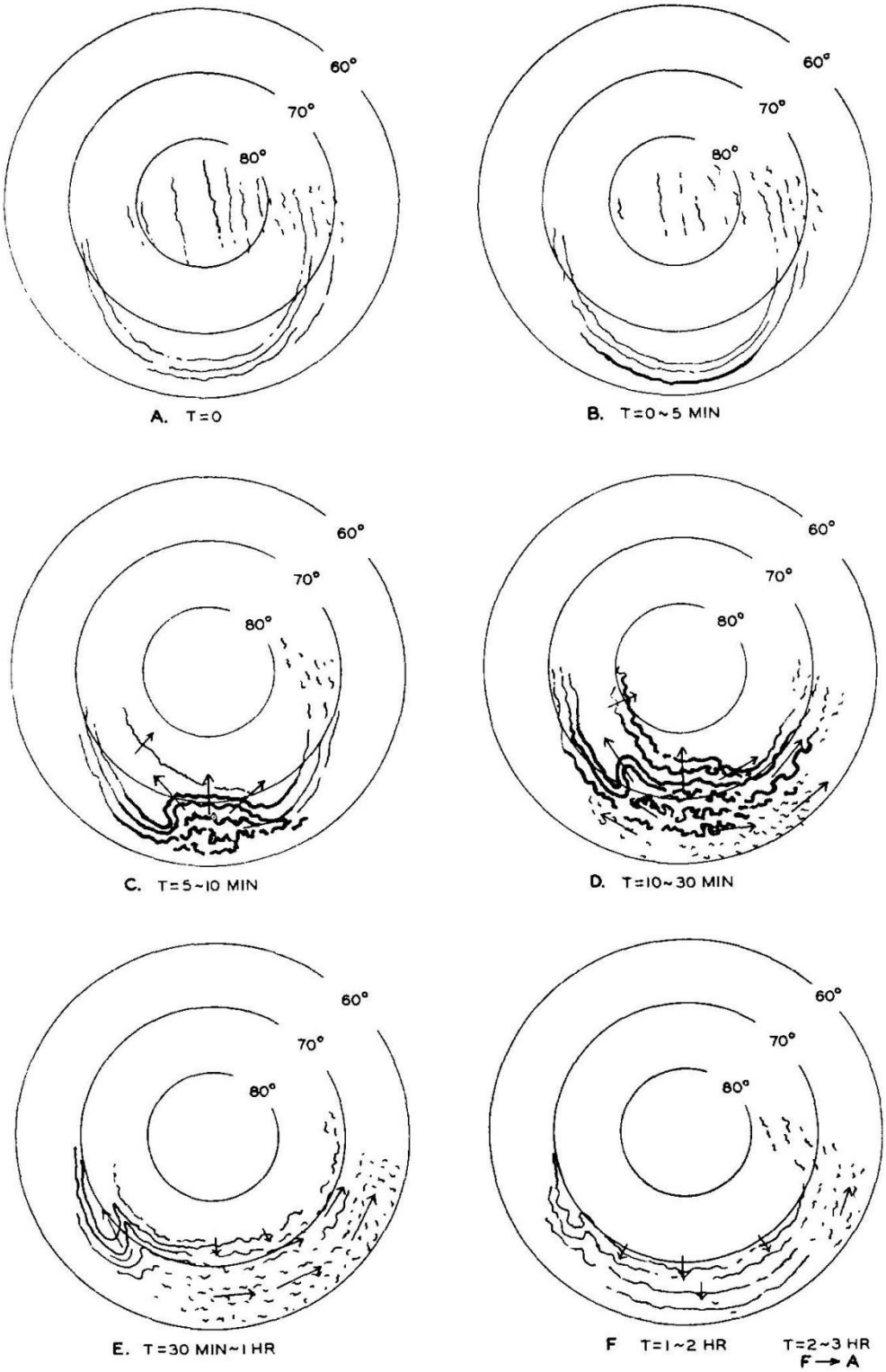

Figure 1.1 Schematic diagram to demonstrate the development of auroral substorm [Akasofu, 1964].

After the identification of auroral substorm, many related studies were conducted using ground-based instruments such as magnetometers and all-sky cameras. With the development of space technology, an increasing number of satellite data had become available for scientific research, and the concept of magnetospheric substorm arose. Hones [1973] showed an important finding of both tailward and earthward plasma flows in the magnetotail, which suggests the formation of two magnetic neutral lines located in the near-Earth and far-tail regions in the magnetotail. This study and following works formed the initial near-Earth neutral line (NENL) substorm model [e.g., Baker et al., 1996]. Shiokawa et al. [1997, 1998] further clarified the time sequence of substorm-associated phenomena in the magnetotail, such as the appearance of a new X-type NENL, the formation of a substorm current wedge resulted from earthward bursty bulk flow (BBF), and the auroral initial brightening at the plasma flow braking point. As shown in Figure 1.2, the substorm onset is considered to be caused by the magnetic reconnection which occurs at 20–30 R_E. The substorm-associated phenomena in the magnetotail occur in sequence from the far-tail to near-Earth regions. Eventually, the NENL substorm model was also named as the outside-in substorm model.

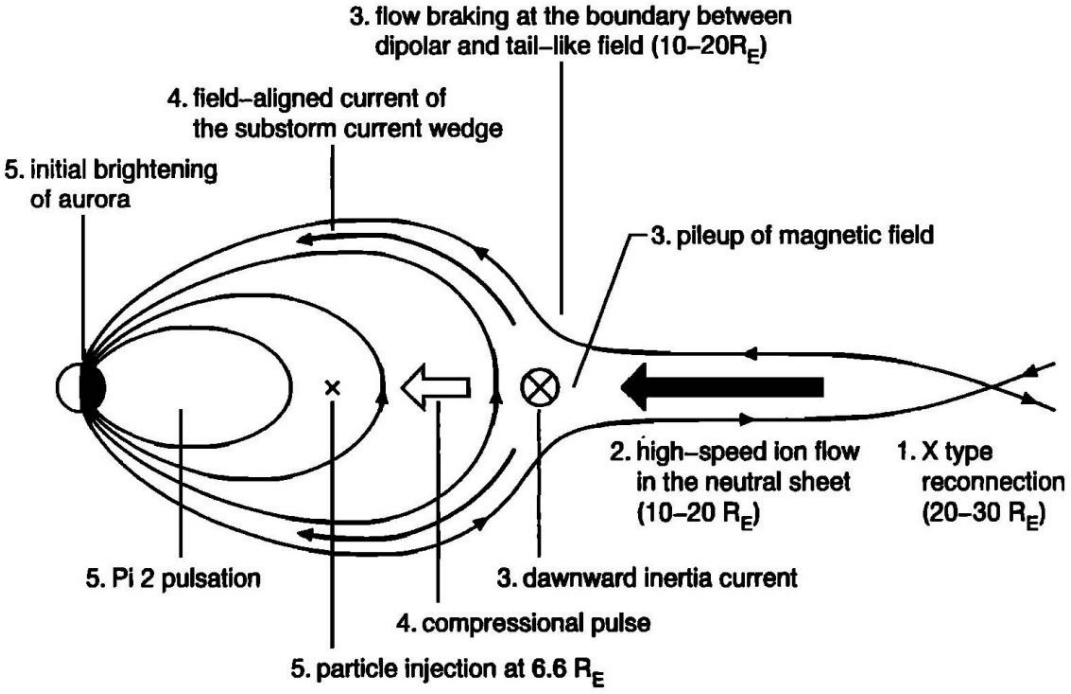

Figure 1.2 A diagram which shows the time sequence of substorm-associated phenomena in the magnetotail according to the outside-in substorm model [Shiokawa et al., 1998].

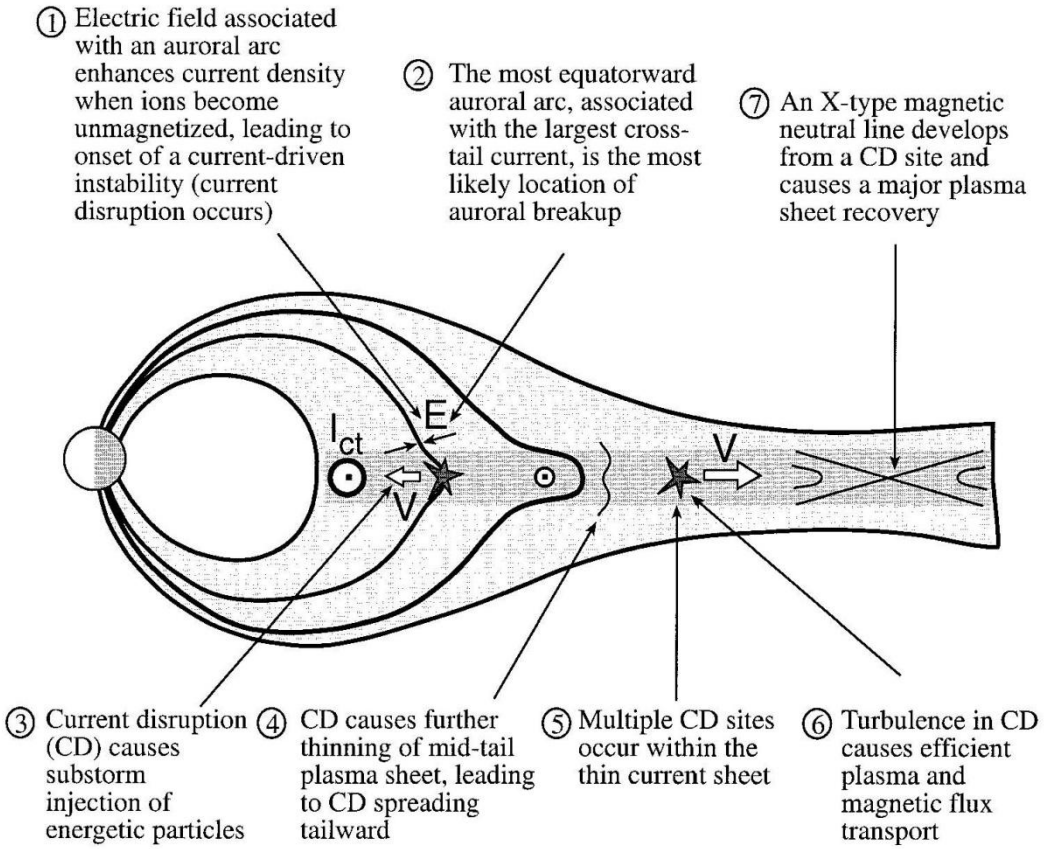

Figure 1.3 A diagram which shows the time sequence of substorm-associated phenomena in the magnetotail according to the inside-out substorm model [Lui, 2001].

On the other hand, some researches focused on the current disruption in the near-Earth region in the magnetotail when exploring the origin of substorm onset [Lui, 2001]. Lui et al. [1990] pointed out that kinetic cross-field instability can occur in the near-Earth magnetotail before the substorm expansion phase. This instability can cause the formation of a substorm current wedge by reducing the cross-tail current. Lui [1991a, 1991b] further proposed the current disruption substorm model in which instabilities in the near-Earth magnetotail are the initial trigger of substorm onset. Some substorm-associated features, including pseudo-breakups and the localized region of substorm initiation, could be explained by this model [Lui et al., 1991c]. As shown in Figure 1.3, the substorm-associated phenomena in the current disruption substorm model occur in sequence from the near-Earth to far-tail regions, which is named as the rarefaction wave. Thus, these considerations about substorms came to be known as the inside-out substorm model.

The formation of a new NENL (outside-in model) and the occurrence of current disruption (inside-out model) have become the two dominant considerations when discussing the onset mechanisms of substorms. Recognizing the importance of both down-tail and near-Earth activities may become a feasible approach in future studies [Henderson, 2009]. In both of two models, magnetic fluctuation in the near-Earth region is an important phenomenon, which will be introduced in Subsection 1.2.

Besides, there are some other hypotheses about substorm onset mechanism rather than the two substorm models raised above. One of them is the MIC substorm model proposed by Kan [1993]. This model focuses on the MIC process, and suggests that substorm onset can be caused by a newly developed ionospheric current system, the so-called cowling electrojet current loop (CECL). Kan [1993] showed that substorms can occur without a new X-type neutral line in the near-Earth magnetotail, which is considered necessary in the outside-in model. Kan et al. [2011] demonstrated this model in more detail, including the development of the CECL. As shown in Figure 1.4, the CECL can propagate from the ionosphere to the magnetosphere. The current disruption occurs when the CECL encounters cross-tail current in the near-Earth region. Then, the following substorm-associated phenomena in the magnetotail are similar to that in the inside-out model. In the MIC model, the cause of CECL which initiates substorm onset is still unknown. The ionospheric conductivity change is one possibility. In Subsection 1.3, we will introduce another candidate to cause CECL, the thermospheric wind variations at high latitudes.

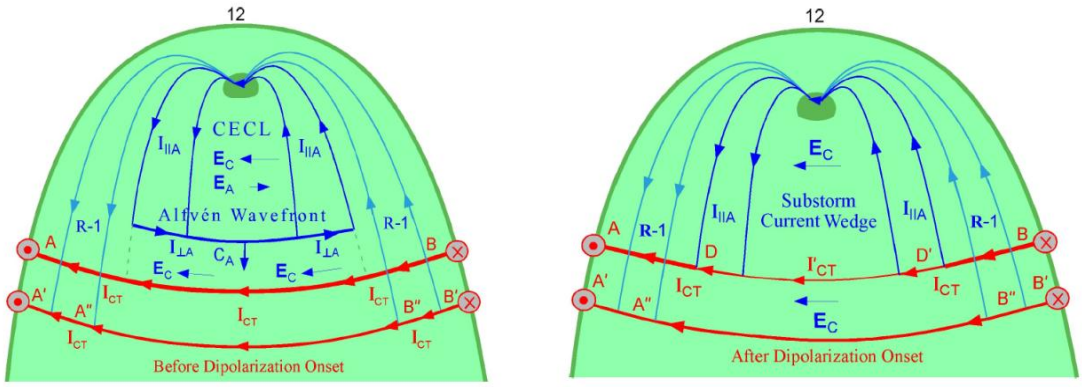

Figure 1.4 A diagram which shows the development of CECL during substorms according to the MIC substorm model [Kan et al., 2011].

1.2 Substorm-associated Magnetic Fluctuations

As one approach to understand substorm onset, magnetic fluctuations are regarded as one of the possible instabilities to trigger substorms in the near-Earth magnetotail. According to the inside-out substorm model, these strong magnetic fluctuations can cause the current disruption at substorm onset, and typically occur close to the neutral sheet in the magnetotail [Lui, 2001]. In the outside-in substorm model, the magnetic fluctuations caused by earthward plasma flow are also one phenomenon involved in the substorm process [Shiokawa et al., 1998].

As shown in Figure 1.5, Takahashi et al. [1987] firstly reported such strong magnetic fluctuations in the magnetotail at $|X| = 8\ R_E$. These magnetic fluctuations had amplitudes from 10 nT to more than 40 nT. Ohtani et al. [1995] pointed out that the typical timescale of these magnetic fluctuations is several times the proton gyroperiod. Ohtani et al. [1995, 1998] used Active Magnetospheric Particle Tracer Explorers/Charge Composition Explorer (AMPTE/CCE) data and fractal analysis to investigate substorm-associated magnetic fluctuations. They concluded that these magnetic fluctuations are strongly related to plasma instabilities and current disruption. Ono et al. [2009] showed that ions in the near-Earth plasma sheet are non-adiabatically accelerated due to the electric field induced by magnetic fluctuations during the dipolarization. Nosé et al. [2010] revealed that dipolarization is often accompanied by the appearance of magnetic fluctuations with a timescale of 3–5 s. These researches of magnetic fluctuations in the near-Earth magnetotail contributed to our understanding of substorms and their onsets.

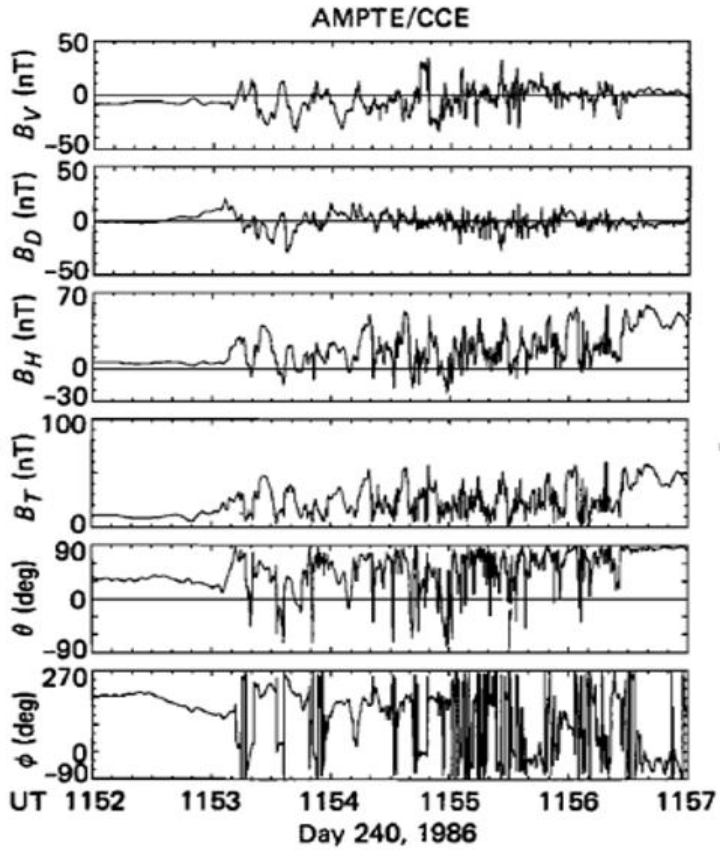

Figure 1.5 The strong magnetic fluctuations reported in the magnetotail at $|X| = 8\ R_E$ [Takahashi et al., 1987].

The importance of studying these magnetic fluctuations in the near-Earth magnetotail also lies in the fact that they are strongly related to non-MHD processes of ions in the magnetotail, during which the kinetic effect of ions plays an important role [Consolini et al., 2005]. The MHD simulation has been proved by previous studies as a useful tool to understand plasma motion in the magnetotail [e.g., Birn et al., 1996; Wiltberger et al., 2000]. However, Lui and Najmi [1997] showed that during the current disruption, the spectrum of substorm-associated magnetic fluctuations can become intermittently broad, including the ion gyroperiod. In such a case, the collapse of the MHD condition can cause difficulty for the study of magnetotail dynamics.

For these magnetic fluctuations in the near-Earth magnetotail, some previous studies also reported their spectral properties [e.g., Nishitani and Oguti, 1988; Lui et al., 1992; Ohtani et al., 1998]. The AMPTE/CCE and Spacecraft Charging at High Altitude (SCATHA) satellites used in their studies had an apogee of ~8.8 R_E and ~7.8 R_E, respectively. Shiokawa et al. [2005a] showed the spectra of some magnetic

fluctuation events, and found that the slope of PSD tends to become steeper at higher frequency range at radial distances of 8–11 R_E in the tail. Kozak et al. [2018] chose three magnetic fluctuation events during dipolarization, and found the similar kink point in PSD curve after dipolarization. These studies promoted our understanding of the spectral properties of magnetic fluctuations and their implication with non-MHD plasma motion.

Despite the above studies about magnetic fluctuations in the near-Earth magnetotail, there have been no comprehensive statistical analyses of these magnetic fluctuations. Besides, the spectral analysis of these magnetic fluctuations at $|X| > 11$ R_E, and the dependence of occurrence rates of magnetic fluctuations on solar activity have not been done yet. In this study, we investigated these topics as shown in Chapters 2 and 3.

1.3 Thermospheric Wind at Substorm Onset

As described in Subsection 1.1, Kan's substorm model focuses on the MIC processes and suggests that the origin of substorm onset can be located in the ionosphere, where the ionospheric conductivity change can cause a new ionospheric current system. In the ionosphere, it is well known that the thermospheric neutral wind can also contribute to the current generation. At high latitudes, the neutral number density and electron number density at an altitude of 250 km are ~10^{15} m^{-3} and ~10^{11} m^{-3}, respectively [Brekke, 1997]. Because the neutral number density is much larger than the plasma number density, the effect of ion-neutral collisions can strongly affect the plasma motion. An example is the "flywheel" effect at high latitudes [e.g., Lyons et al., 1985; Deng et al., 1991], where the neutral circulation can strongly contribute to the Hall current system for several hours after a geomagnetic storm. Along the magnetic field line, plasma motion driven by neutral particles could also cause the reconfiguration of ionospheric structure, as shown in Figure 1.6. Therefore, we consider that the wind-induced ionospheric current at substorm onsets may contribute to the CECL described in the MIC substorm model, and affect plasma dynamics in the magnetosphere through geomagnetic field line.

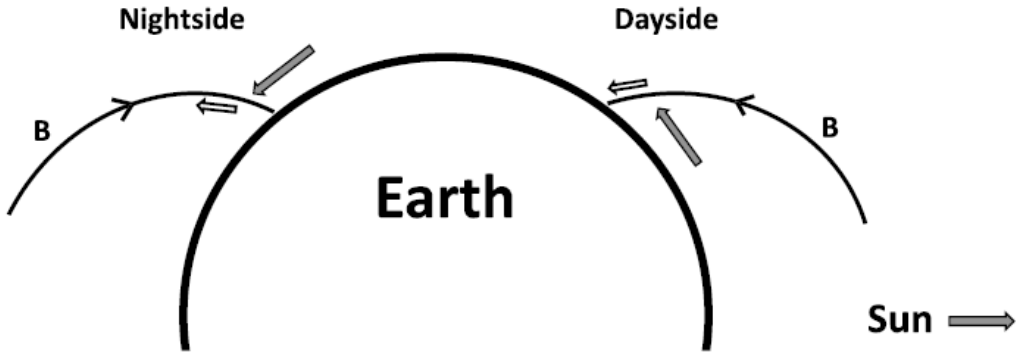

Figure 1.6 The horizontal thermospheric wind could affect the F-layer of ionosphere by pushing charged plasma along the magnetic field line [David et al., 2016].

On the other hand, huge energy input from the magnetosphere during substorms can strongly affect the high-latitude thermosphere. In previous studies, the FPI which measures the Doppler shift of emission lines from aurora and airglow is a widely used instrument for wind measurement. The atoms and molecules in the thermosphere cause line emissions, which are excited by phenomena such as auroral electron bombardment and solar ultraviolet (UV) absorption. These atoms and molecules move with the thermospheric wind. Therefore, the FPI obtains thermospheric wind velocities through measuring the Doppler shift of these line emissions. At ionospheric F-region altitude, FPIs have been used to measure the thermospheric wind through red-line emission at a wavelength of 630.0 nm from atomic oxygen.

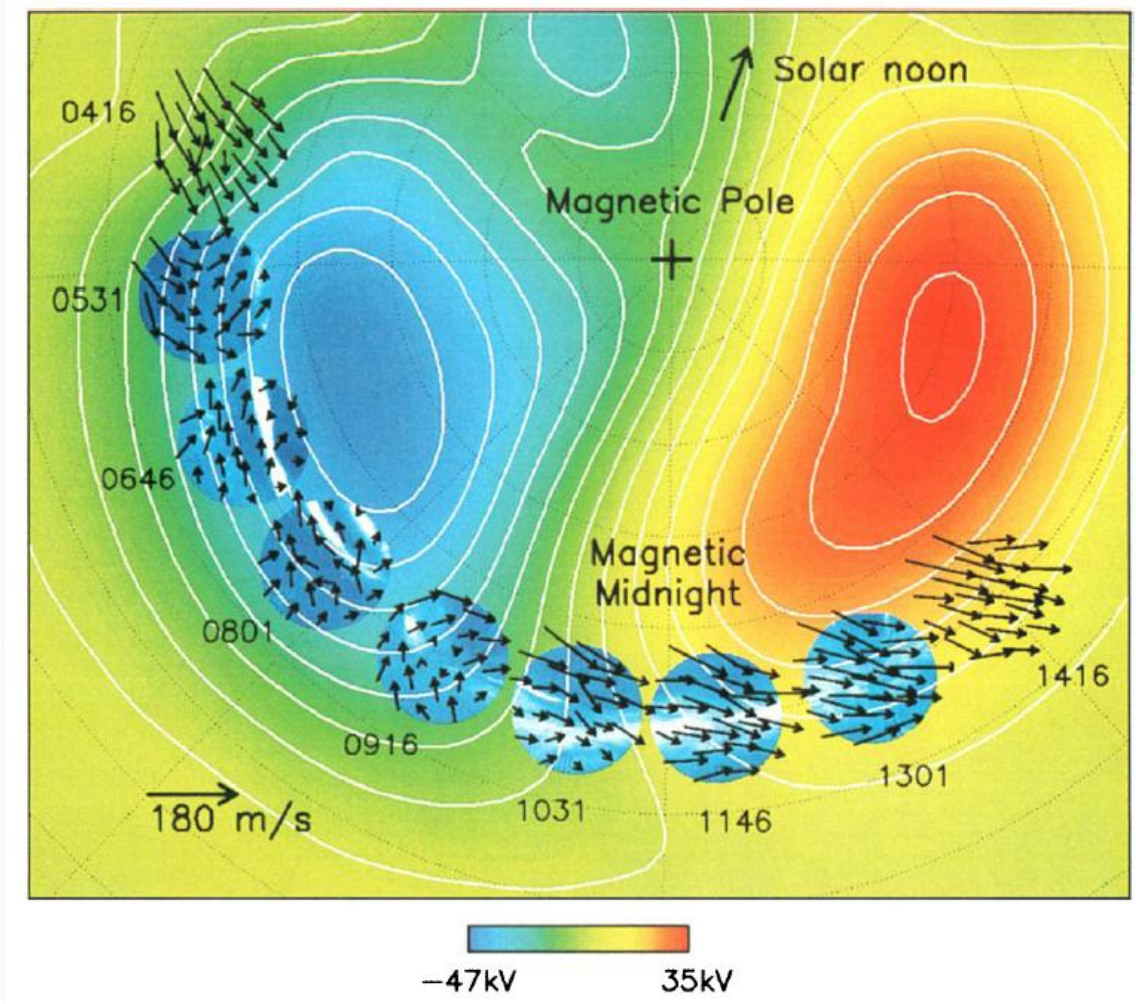

Figure 1.7 Thermospheric wind observation obtained by an FPI at high latitudes. Background shows the plasma convection model and electric potential map [Conde et al., 2001].

At high latitudes, thermospheric response to substorms and auroral activities have been investigated in many previous studies using FPIs. Some studies used FPI measurements and focused on the relationship between thermospheric wind variations and auroral activities [e.g., Conde and Smith, 1998; Conde et al., 2001; Ishii et al., 2001, 2004]. As shown in Figure 1.7, Conde et al. [2001] found clear relationship between F-region wind field, plasma convection, and the spatial structure of aurora. The black arrows overplotted on the all-sky camera image in each circle demonstrate the complete sky map of wind field as a function of time. This plot provides a panoramic view of the evolution of thermospheric wind field. Background rainbow image indicates a map of the ionospheric electric potential using the ionospheric electric field model of Weimer [1995]. The white contours describe the

two-cell plasma convection status at northern hemisphere. The plasma convection shows a clear influence on the thermospheric wind. At 0531–0801 universal time (UT), wind field changes into sunward from anti-sunward, indicating the ion drag effect on neutral particles at the duskside. Near Tromsø, an FPI at Kiruna, Sweden, has been used in related studies as well [e.g., Rees et al., 1984; Aruliah et al., 1991, 1999].

Some other studies using FPIs focused on the thermospheric wind during specific substorm phases [e.g., Ritter et al., 2010; Oyama et al., 2016; Cai et al., 2019]. Using an FPI at Tromsø, Norway, Oyama et al. [2016] studied lower thermospheric wind variations in auroral patches during the substorm recovery phase. Ritter et al. [2010] analyzed the wind data of Challenging Minisatellite Payload (CHAMP) satellite at an altitude of 400 km, and statistically studied the thermospheric response to substorm onsets. They found that the perturbation of thermospheric wind caused by substorms is weak (< 20 m/s).

Despite these previous wind studies at high latitudes, thermospheric wind variations at local substorm onsets using an FPI have not been reported. And no study has discussed their possible contribution to substorm onset. These contents will be reported in Chapter 4.

1.4 Average Thermospheric Wind during Geomagnetically Quiet Time

The thermospheric responses to substorm activities at high latitudes are important, as we introduced in Subsection 1.3. The average winds during geomagnetically quiet times at high latitudes are also worth researching, because they provide a baseline for studies of geomagnetically disturbed times in the upper atmosphere.

The high-latitude thermospheric wind can be affected by localized geomagnetic activities such as particle precipitation and ion drag [e.g., Batten and Rees, 1990; Oyama et al., 2009]. Under geomagnetically quiet times, the wind pattern at high latitudes can still be affected by geomagnetic activities, although Kp and Ap indices are used to ensure the globally quiet condition in many previous studies. Previous studies reported the quiet-time wind patterns in F region at high latitudes [e.g., Witasse et al., 1998; Emmert et al., 2006a, 2006b]. As shown in Figure 1.8,

Aruliah et al. [1999] investigated the Kp dependence of thermospheric winds at Kiruna in Sweden using an FPI via the 630 nm airglow/auroral emission. Dhadly et al. [2017] focused on the seasonal dependence of the quiet-time thermospheric winds in the northern high latitudes using measurements obtained from ground-based FPIs, as well as the Upper Atmosphere Research Satellite (UARS), Gravity Field and Steady-State Ocean Circulation Explorer (GOCE), and Dynamic Explorer 2 (DE2).

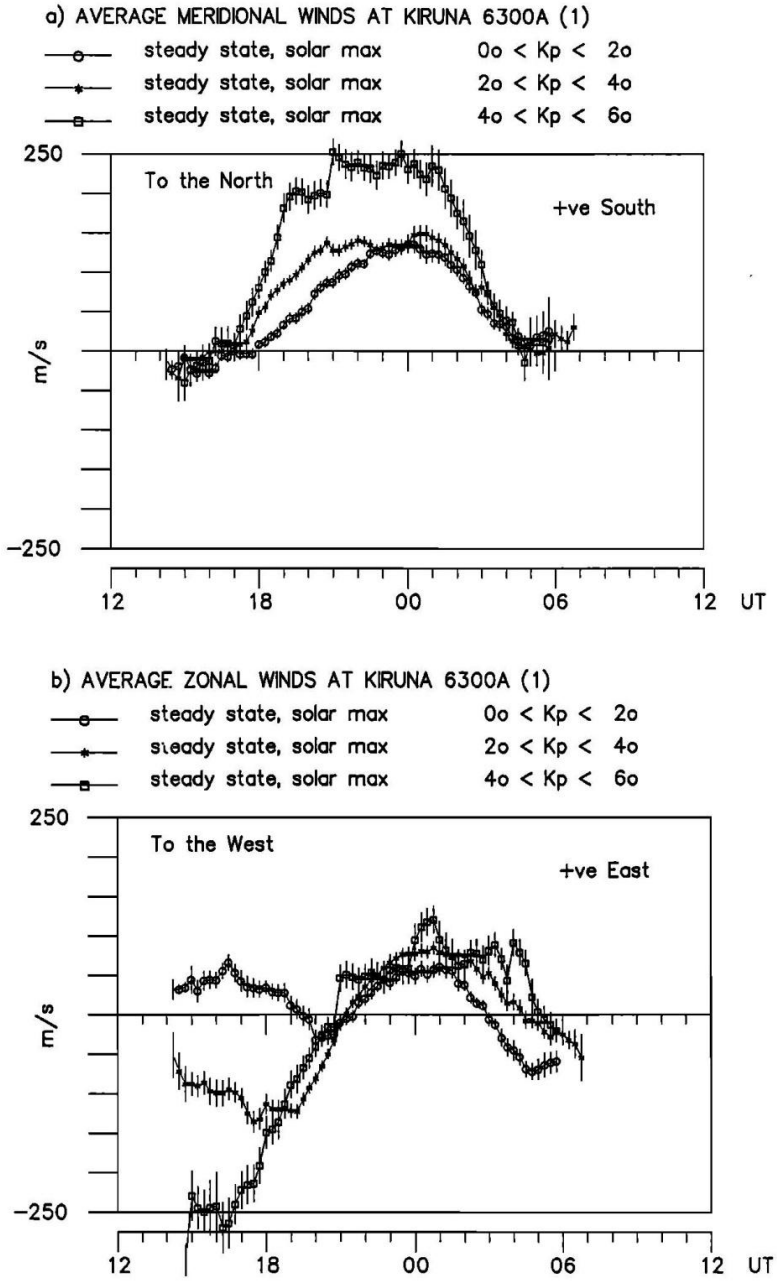

Figure 1.8 Average wind under different geomagnetic conditions at Kiruna, Sweden shown in Aruliah et al. [1999].

Despite of these previous studies, the quiet-time thermospheric wind pattern at Tromsø has not been investigated using ground-based FPI. Such a study at Tromsø is important and constructive for future studies of thermospheric dynamics, because Tromsø is the European Incoherent Scatter (EISCAT) radar site. In Chapter 5, we will report a study of quiet-time average winds at Tromsø, as well as how it contributes to the event study at local substorm onsets shown in Chapter 4.

1.5 Purpose of Study

In this chapter, we reviewed three typical substorm models which have different considerations about substorm onset. The origin of substorm onset in the outside-in and inside-out models are considered to be located at far-tail region at $|X|$ = 20–30 R_E and near-Earth magnetotail at ~10 R_E, respectively. The MIC model believes that the ionospheric activities can trigger substorm onset. Based on the background introduced above, we focus on the mechanisms at substorm onsets in both the magnetosphere and the ionosphere, and investigate phenomena that may trigger substorm onsets or associated with it. The contents in this study are divided into four topics.

For the first topic in Chapter 2, we focus on the substorm onset mechanism in the magnetosphere, and conduct a statistical analysis of substorm-associated severe magnetic fluctuations in the near-Earth magnetotail. These magnetic fluctuations have periods shorter than the local ion gyroperiod, and occur at substorm onset or expansion phase. We want to show the spatial distribution of the occurrence rates of these magnetic fluctuations, and their relationship with earthward plasma flow. We use THEMIS satellite observations, solar wind data, as well as ground-based geomagnetic indices. We also discuss how both the inside-out and outside-in substorm models can explain the observation results. There have been no statistical analyses of these magnetic fluctuations before.

For the second topic in Chapter 3, we investigate the spectra of severe magnetic fluctuations using the THEMIS data at 8–12 R_E based on our previous statistical study in the first topic. The THEMIS data provide larger coverage in radial distances compared with previous studies. At the same time, we also show the relationship between severe magnetic fluctuations and solar activity in a complete solar cycle. These works have not been done before and will further contribute to our knowledge about severe magnetic fluctuations in the near-Earth magnetotail.

For the third topic in Chapter 4, we focus on the substorm onset mechanism in

the ionosphere and thermosphere, and show the characteristics of thermospheric wind variations at local substorm onsets at Tromsø, Norway. We discuss how thermospheric wind variations can provide a feedback to the development of substorm expansion phase in the magnetotail. We also discuss all possible causes of the observed wind variations. The wind data at F-region height obtained by a ground-based FPI provide both the zonal and meridional winds. To our knowledge, such study has not been done before.

For the fourth topic in Chapter 5, we investigate the average thermospheric winds at Tromsø during geomagnetically quiet times. This is an expanded study based on the results of the third topic, because we want to subtract the deviations due to quiet-time average winds from the observed wind variations at local substorm onsets in the event study. We also compare the observed quiet-time average winds at Tromsø with the results at nearby station, and report two events during geomagnetically quiet times with occasional large wind deviations (> 100 m/s) from the quiet-time averages.

Finally in Chapter 6, we will summarize general conclusions of this thesis, and provide possible future directions of the related research.

Chapter 2
Statistical Analysis of Severe Magnetic Fluctuations in the Near-Earth Magnetotail

This chapter focuses on the substorm onset mechanisms in the magnetosphere, and presents the first statistical analysis of substorm-associated severe magnetic fluctuations ($\sigma_B/\bar{B} > 0.5$, where σ_B and $\bar{B}$ are the standard deviation and the average value of magnetic field intensity during the time interval of the local proton gyroperiod) in the near-Earth magnetotail. The observed severe magnetic fluctuations had periods shorter than the local ion gyroperiod, and occurred at substorm onset or during substorm expansion phase. We calculated the spatial distribution of the occurrence rates of severe magnetic fluctuations. We also discussed the relationship between these fluctuations and earthward plasma flow on the basis of the inside-out and outside-in substorm models. The contents described in this chapter have been published by Xu et al. [2017b].

2.1 THEMIS Data Set and Criteria of Severe Magnetic Fluctuation Event

In this study, we used 2-year magnetic field data from 2013 and 2014 (sampling rate: 4 Hz) obtained by the fluxgate magnetometer (FGM) aboard the THEMIS-E satellite [Angelopoulos, 2008; Auster et al., 2008]. The plasma flow data were obtained by the electrostatic analyzer (ESA) aboard the THEMIS-E satellite [McFadden et al., 2009]. Figure 2.1 shows the three subregions chosen in this analysis, which is located in the near-Earth magnetotail at (X_{GSM}, Y_{GSM}, Z_{GSM}) = (-9 ±3, ±5, ±3) R_E in the geocentric solar magnetospheric (GSM) coordinate system. As introduced in Chapter 1, the magnetic fluctuations that trigger substorm onsets are expected to occur in such region in the near-Earth magnetotail [e.g., Lui et al., 1991a; Ohtani et al., 1995]. We set three subregions because we expected to observe some dependences of the phenomena on the radial distance in the magnetotail.

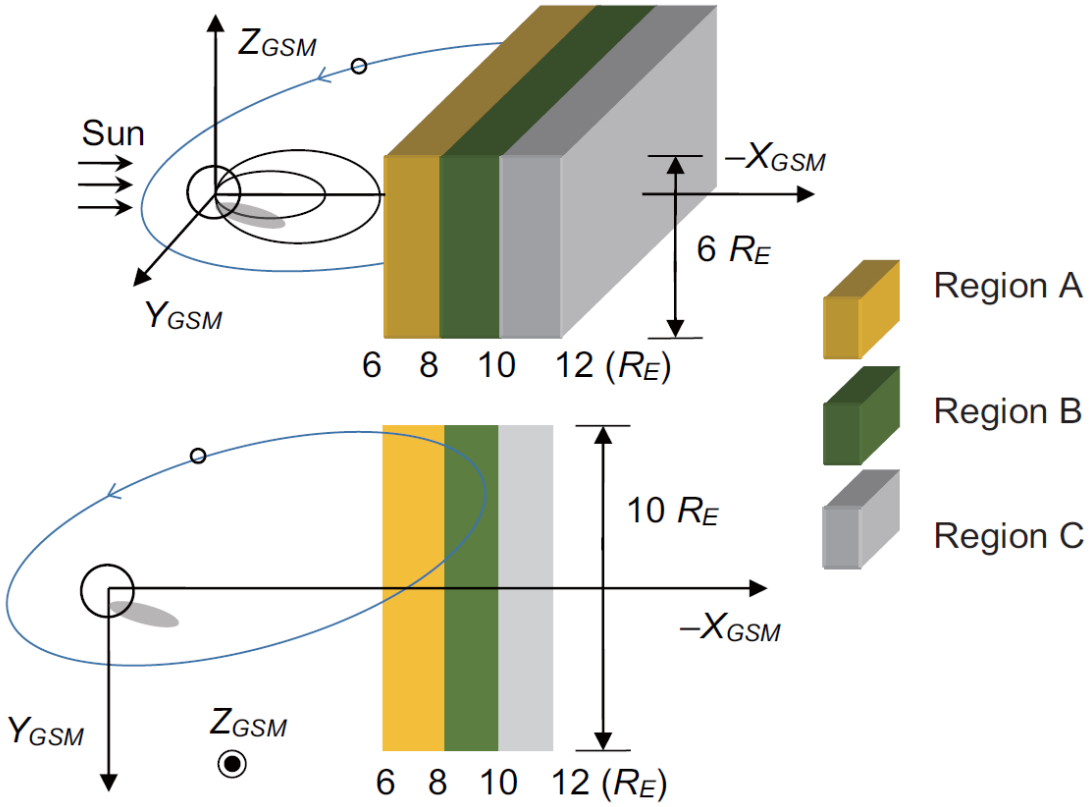

Figure 2.1 The magnetic field data observed in three subregions were analyzed. The three subregions are divided according to the X_{GSM} coordinates. The top and bottom parts show three subregions in GSM coordinates and in the GSM-*XY* plane, respectively.

Figure 2.2 shows the two-step calculation we used to identify severe magnetic fluctuation events. In the first step, we calculated the average ambient magnetic field intensity (*B*) for a 1-s time interval, as indicated by the light blue rectangle in Figure 2.2a. Then, we calculated the local gyroperiod of proton T_g as

$$T_g = \frac{2\pi m_p}{qB}, \tag{2.1}$$

where T_g, m_p, and q are the gyroperiod, mass, and charge of the proton, respectively [Chen, 1983]. In the second step, we calculated the ratio *R* based on Hendricks and Robey [1936] as

$$R = \frac{\sigma_B}{\bar{B}}, \tag{2.2}$$

where σ_B and $\bar{B}$ are the standard deviation and average of magnetic field intensity for the time interval T_g, as shown in the yellow rectangle in Figure 2.2b. Then we moved to the next adjacent 1-s time interval and applied the same two-step calculation, as shown in dark blue rectangle in Figure 2.2c. By repeating this

calculation, each 1-s time interval with $R > 0.5$ was defined as one severe magnetic fluctuation events. Note that we calculated the ratio R based on every 1-s time interval from the total magnetic field intensity data, and the time intervals of calculations in two steps had the same central time. Based on this criterion, we focused on the magnetic fluctuations that can violate ion gyromotion, which may further contribute to ion kinetic effects such as current disruption at substorm onset.

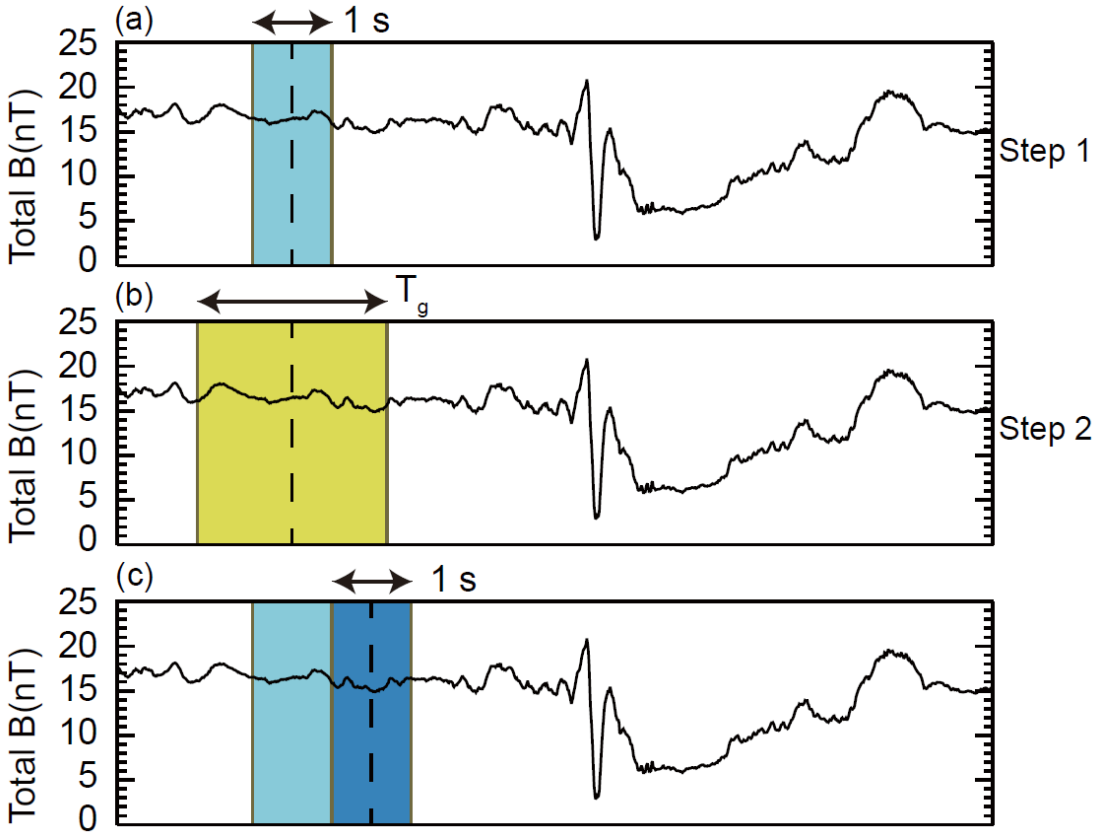

Figure 2.2 The two-step calculation to identify severe magnetic fluctuation event.

Because relatively long-lasting magnetic fluctuations are more relevant to substorm onset [Lui, 1991a], we also defined three continuous severe magnetic fluctuation events that occur within 10 min as one multiple-fluctuation event. Besides, in the calculation of the ambient magnetic field intensity during the first step, we abandoned the time sections with $B > 65.5$ nT (= $2\pi m_p/(4T_s)q$, where T_s is the sampling period of the magnetic field data with a value of 0.25 s). This is because that we wanted to guarantee the reliability of calculation in the subsequent second step.

We should note that the applied criterion can include all kinds of magnetic fluctuations with amplitudes comparable to or larger than the ambient magnetic field

intensity and with periods shorter than the local ion gyroperiod. This means that the observed events can contain both incoherent structures, such as current disruptions caused by waves and instabilities, and coherent structures, such as sharp magnetic field variations during dipolarization fronts [e.g., Runov et al., 2011] or the flapping of plasma sheet. Therefore, the occurrence rates of severe magnetic fluctuations shown in this study might be the possibly maximum values that caused by instabilities.

2.2 Analysis of THEMIS Satellite Data and Discussion

2.2.1 Fluctuation Events and Occurrence Rate

Figure 2.3 shows an example of 11 multiple-fluctuation events, which include 33 severe magnetic fluctuation events (the last severe magnetic fluctuation event in Figure 2.3 was out of the plotted time range). The 33 severe magnetic fluctuation events are indicated by the vertical lines. Note that the severe magnetic fluctuations occurred when the ion velocities were large. In order to show the property of severe magnetic fluctuations in more detail, we enlarged the 1-min time interval from 06:21 UT in Figure 2.4. There were 15 severe magnetic fluctuation events during this 1 min. The total magnetic field intensity showed a strong variation with a maximum amplitude of ~31 nT.

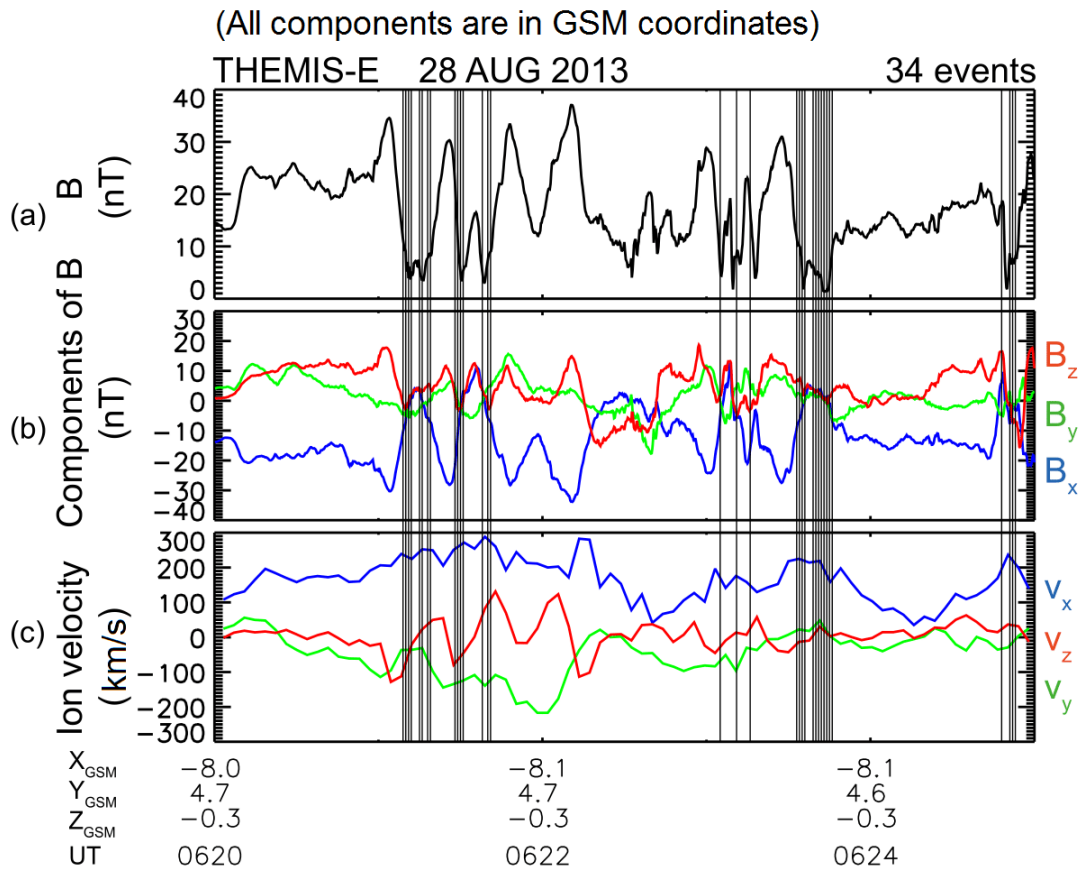

Figure 2.3 Example multiple-fluctuation events on August 28, 2013. There were 33 severe magnetic fluctuation events, which are indicated by the vertical lines.

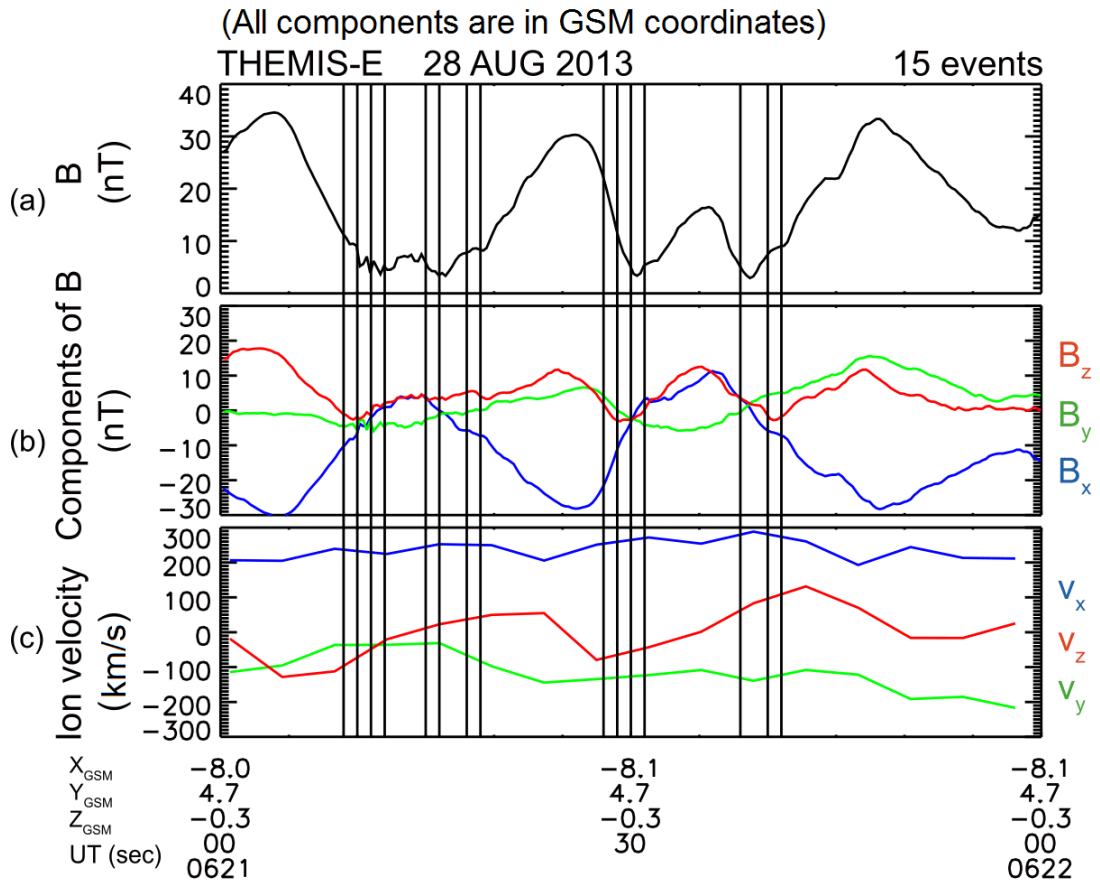

Figure 2.4 Enlarged plot for example multiple-fluctuation events on August 28, 2013. It shows the 1-min time interval after 06:21 UT. There were 15 severe magnetic fluctuation events.

In total, our statistical analysis from 2013 and 2014 selected 3322 severe magnetic fluctuation events. At the same time, 3135 severe magnetic fluctuation events are contained in 1045 multiple-fluctuation events. For all the severe magnetic fluctuation events, 1.2 % of them are located in Region A (6–8 R_E), 22.2 % of them are located in Region B (8–10 R_E), and 76.6 % of them are located in Region C (10–12 R_E). For 99.8 % of the severe magnetic fluctuation events, the plasma beta values were greater than 1 (9.2 % of which were between 1 and 10, and 90.6 % were greater than 10). This indicates that the observed fluctuation events were located in the plasma sheet [e.g., Baumjohann et al., 1990; Schmid et al., 2011]. Figure 2.5 shows the distribution of the duration time of these severe magnetic fluctuations. The duration was defined as the time between the first and last fluctuation events, when the 1 s severe magnetic fluctuation events occurred sequentially. Nearly all severe magnetic fluctuations had duration times of less than 20 s, with only 15 exceptions.

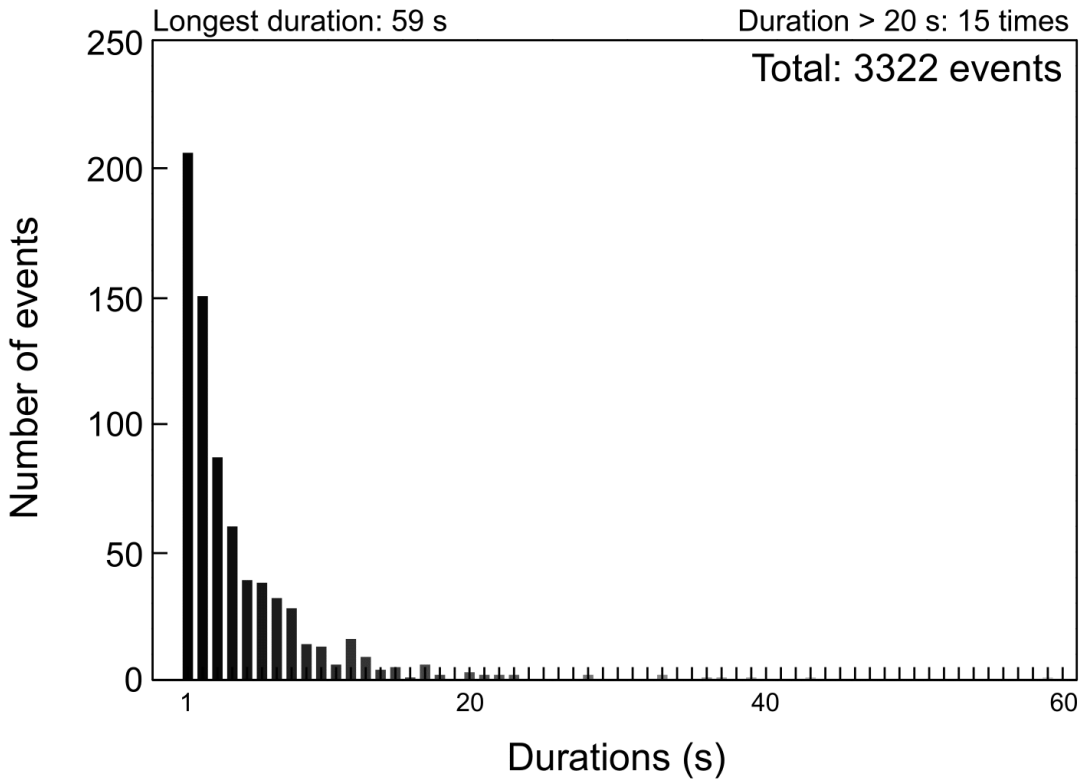

Figure 2.5 Distribution of duration time for severe magnetic fluctuation events.

We then estimated the occurrence rates of severe magnetic fluctuation events and multiple-fluctuation events for the three subregions and the entire analyzed region in the magnetotail. This was done by calculating the ratio between the number of 1-s fluctuation events and the total observation time in seconds in the corresponding region. For example, the occurrence rate of severe magnetic fluctuation events for Region A was calculated as 41 s/1316072 s = 0.00312 %. The occurrence rates are 0.00312, 0.0312, and 0.0675 % at $|X|$ = 6–8, 8–10, and 10–12 R_E, respectively. The occurrence rates show a tendency in decrease when the location becomes closer to the Earth. These results are summarized in Table 2.1.

Table 2.1 Occurrence rates and inferred volumes of the onset regions ($R > 0.5$).

Region	**Number of events (Multiple events)**	**Observation time (s)**	**Occurrence rate (Multiple events)**	**Inferred volume (R_E^3)**
Region A	41	1316072	0.00312 %	0.80
(6–8 R_E)	(36)		(0.190 %)	
Region B	739	2367082	0.0312 %	8.02
(8–10 R_E)	(690)		(1.35 %)	
Region C	2542	3766865	0.0675 %	17.36
(10–12 R_E)	(2409)		(2.42 %)	

The occurrence rates of severe magnetic fluctuations calculated for multiple-fluctuation events are also shown in Table 2.1 (0.190, 1.35, and 2.42 % for Region A, Region B and Region C, respectively). In this calculation, we used the total time interval of multiple-fluctuation event as the numerator, and the observation time of satellite as the denominator. We set the time of the first severe magnetic fluctuation event in one multiple-fluctuation event as the start time, and accumulated the following 10 min in the calculation of the occurrence rate according to the definition of multiple-fluctuation event. We also removed the overlapped time interval between two adjacent multiple-fluctuation events.

Based on these occurrences rates of severe magnetic fluctuations, we made additional two estimations. Firstly, magnetic fluctuation is considered as one possible trigger for current disruption and substorm onset in the inside-out substorm model. According to Borovsky et al. [1993], on average four substorms occur every day. If we assume that each substorm is accompanied by a 5-min current disruption or magnetic fluctuation [e.g., Takahashi et al., 1987; Lui, 1991b], the ratio between the current disruption time (5 min $\times 4$ = 20 min) and the total time in a day (1440 min) is about 1.4 %. From Table 2.1, the occurrence rate of severe magnetic fluctuations for the entire region is 0.0446 %. Considering the inside-out substorm model, our results may indicate that approximately 3.2 % (= 0.0446/1.4) of all substorms are caused by severe magnetic fluctuations.

However, the above estimation of 3.2 % assumed that the current disruption occurs everywhere in the plasma sheet observed by the satellite. In fact, a normal case is that current disruption can be localized in a small region. In such a case, we would miss a lot of fluctuation events during the satellite measurement. If we assume that all

substorms are caused by the severe magnetic fluctuations, we can estimate the scale size of the current disruption region from the ratio between the occurrence rate of severe magnetic fluctuations (0.0446 %) and the occurrence rate of substorms (1.4 %). The estimated scale size of current disruption is 11.47 R_E^3 for the entire region (= 6 R_E × 10 R_E × 6 R_E × 0.0446/1.4). The scale size of BBF is 2–3 R_E in the dawn-dusk direction and 1.5–2 R_E in the north-south direction [Nakamura et al., 2004]. Therefore, the estimation of 11.47 R_E^3 seems to be a reasonable scale size for current disruption at substorm onset in the near-Earth magnetotail. As shown in Table 2.1, similar estimations indicate that such localized volumes are 0.80 R_E^3 (= 2 R_E × 10 R_E × 6 R_E × 3 × 0.00312/1.4) for Region A, 8.02 R_E^3 for Region B, and 17.36 R_E^3 for Region C.

Table 2.2 Occurrence rates of magnetic fluctuations (R > 0.2).

Region	Number of Events	Observation Time (s)	Occurrence Rate
Region A (6–8 R_E)	238	1608118	0.0148 %
Region B (8–10 R_E)	2566	2714082	0.0945 %
Region C (10–12 R_E)	9624	4278838	0.225 %

In order to check the dependence of the occurrence rates of severe magnetic fluctuations on their amplitudes, we also calculated the occurrence rates of magnetic fluctuation events by changing the selection criterion into R > 0.2. These results are summarized in Table 2.2. In such a case, we obtained occurrence rates of fluctuation events nearly 10 times larger than those in Table 2.1 with R > 0.5. This may indicate that the occurrence of magnetic fluctuation events significantly decreases as their amplitudes become larger and approach the level to affect the ion gyromotion.

It should be noted that there is an ambiguity in the relative locations of these fluctuation events with respect to the center of the plasma sheet in the Z_{GSM} direction. According to the inside-out model, magnetic fluctuations that occur in the neutral sheet are responsible for current disruption [Lui et al., 1991a]. The neutral sheet is located in the center of plasma sheet, and has a small ambient magnetic field intensity. Therefore, the above estimation of the occurrence rates of fluctuation events would be affected by this ambiguity. In Subsection 2.2.2, we calculated the distance from the model neutral sheet to the location of these fluctuation events.

2.2.2 Distance to the T01-Based Neutral Sheet

We used the empirical magnetospheric magnetic field model (T01) of Tsyganenko [2002a, 2002b] to evaluate the distance between fluctuation event and the neutral sheet. This T01 model is commonly used and valid at $|X| \leqslant 15\ R_E$ in the inner magnetosphere, which includes the region studied herein. We first defined the Z_{GSM} position of the neutral sheet as the location where the T01-based B_x component changes its sign at a given point in GSM-*XY* plane. Then, we calculated the ΔZ_{NS} (Z_{GSM} distance from the event position to the model neutral sheet) for each severe magnetic fluctuation event. We found that ΔZ_{NS} was less than 1 R_E for nearly all events (3167 events). One event had ΔZ_{NS} with value greater than 1 R_E. Another 154 events were excluded due to the lack of solar wind data necessary for the T01 model.

Note that in order to obtain the spatial distributions of the occurrence rates, we calculated ΔZ_{NS} for all the observation time intervals from 2013 and 2014. To calculate the G1 and G2 parameters in the T01 model, which indicate the 1 h prehistory state of the solar wind, we used the solar wind and interplanetary magnetic field (IMF) data for twelve 5 min time intervals (1 h duration) before the observation times and calculated 1 h averages. However, valid solar wind or IMF data were not available for 8.9 % of the observation times, which were excluded in the calculation. If the 5 min interval data were incomplete during the 1 h, we only used the valid ones to calculate the G1 and G2 parameters.

Figure 2.6 shows the spatial distributions of (a) the number of severe magnetic fluctuation events, (b) observation times, and (c) the occurrence rates of severe magnetic fluctuation events normalized by the observation times in the GSM-*XY* plane. The largest occurrence rate (0.170 %) is located at the dusk side at $|X| = 10$–$11\ R_E$. This result is consistent with the typical locations of dipolarizations and bursty bulk flows, which often occur at the dusk side in the magnetotail [Nagai, 1991; Angelopoulos et al., 1994].

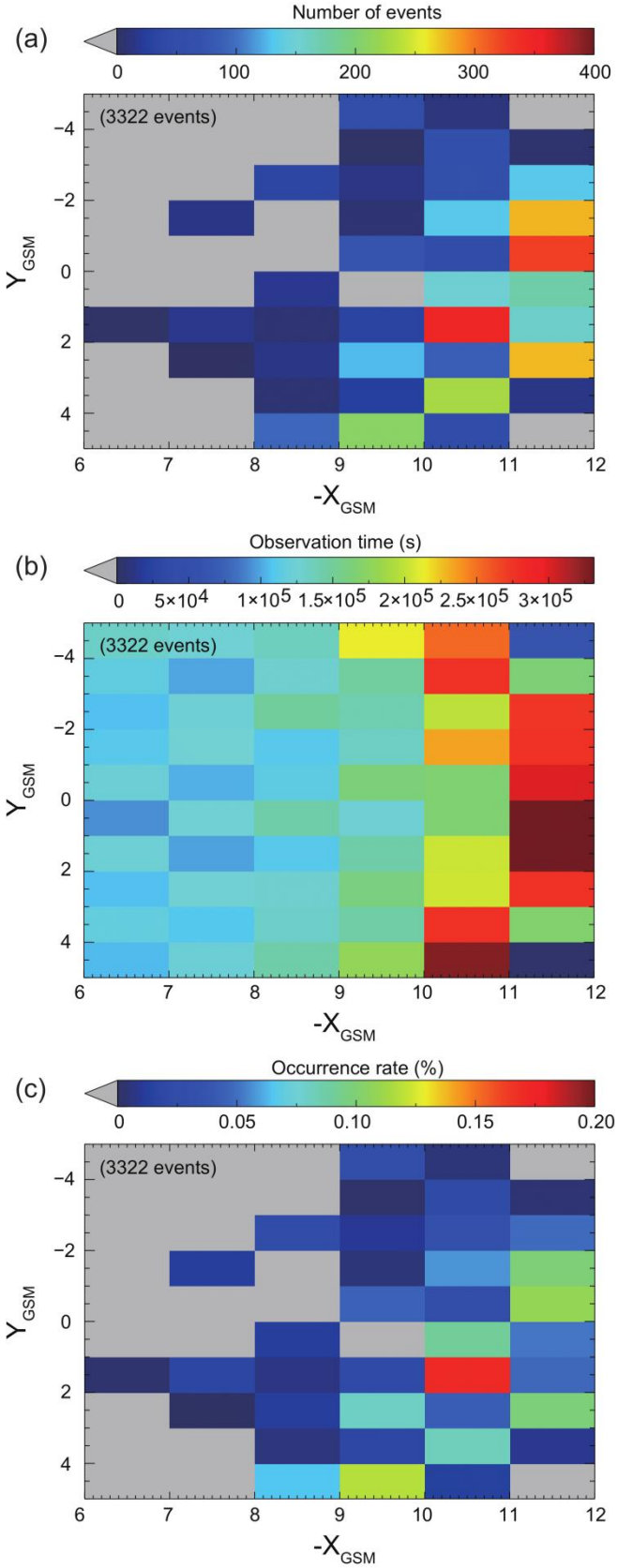

Figure 2.6 The spatial distribution of (a) the number of fluctuation events, (b) observation times, and (c) the occurrence rates of severe magnetic fluctuation events normalized by the observation times in the GSM-*XY* plane.

Figure 2.7 shows the spatial distributions of (a) the number of severe magnetic fluctuation events, (b) observation times, and (c) the occurrence rates of the severe magnetic fluctuation events normalized by the observation times in the X_{GSM}-ΔZ_{NS} plane. The largest occurrence rate (0.361 %) is located at $|X|$ =10–11 R_E, corresponding to a short distance to the neutral sheet at $\Delta Z_{NS} < 0.2$ R_E. In the narrow region with $\Delta Z_{NS} < 1$ R_E, the occurrence rate of fluctuation events tends to increase when it becomes closer to the neutral sheet. The largest occurrence rate was found at the neutral sheet, which is consistent with the typical location of current disruption in both the inside-out and outside-in models. Figure 2.8 shows the occurrence rates of severe magnetic fluctuations according to ΔZ_{NS} and each subregion. We found that fluctuations occur most frequently in Region C ($|X|$ = 10–12 R_E), and the largest occurrence rate in Region C is 0.233 % at $\Delta Z_{NS} < 0.2$ R_E.

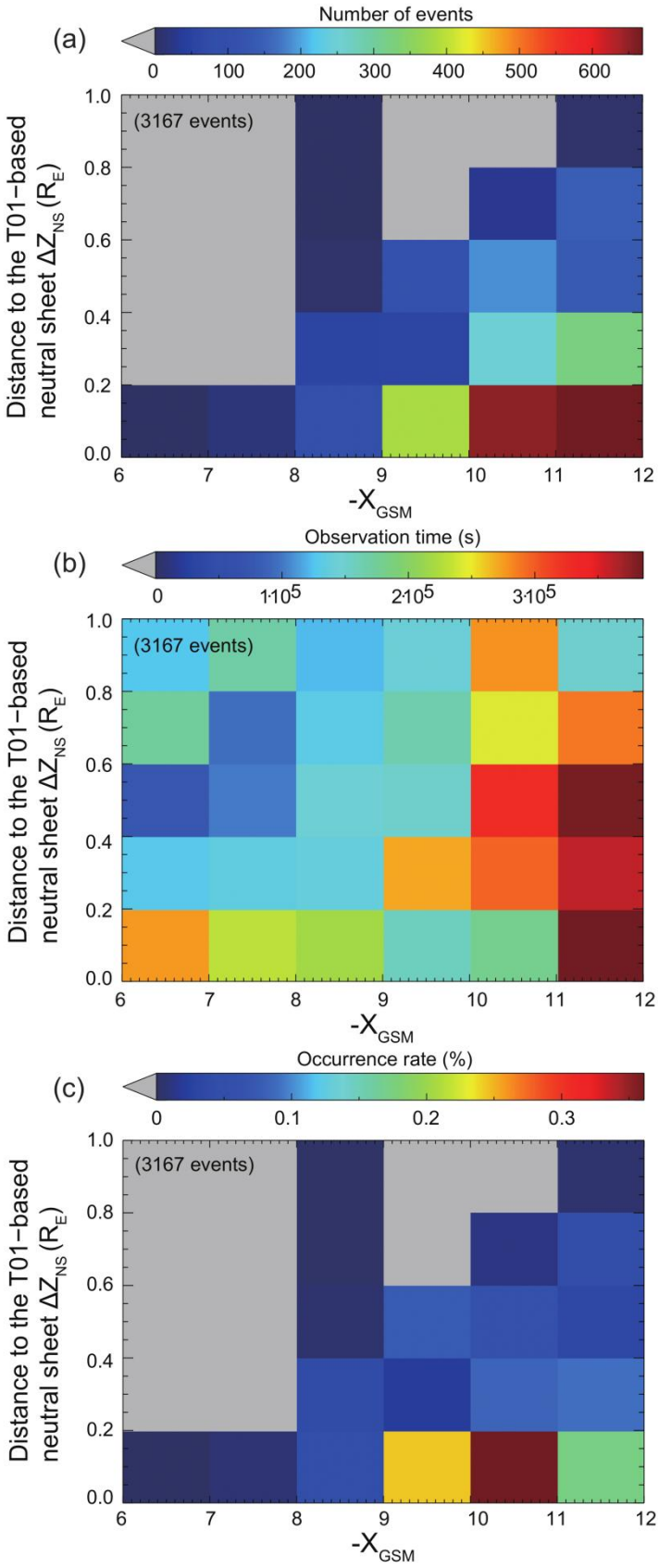

Figure 2.7 The spatial distributions of (a) the number of fluctuation events, (b) observation times, and (c) the occurrence rates of severe magnetic fluctuation events normalized by the observation times in the X_{GSM}-ΔZ_{NS} plane.

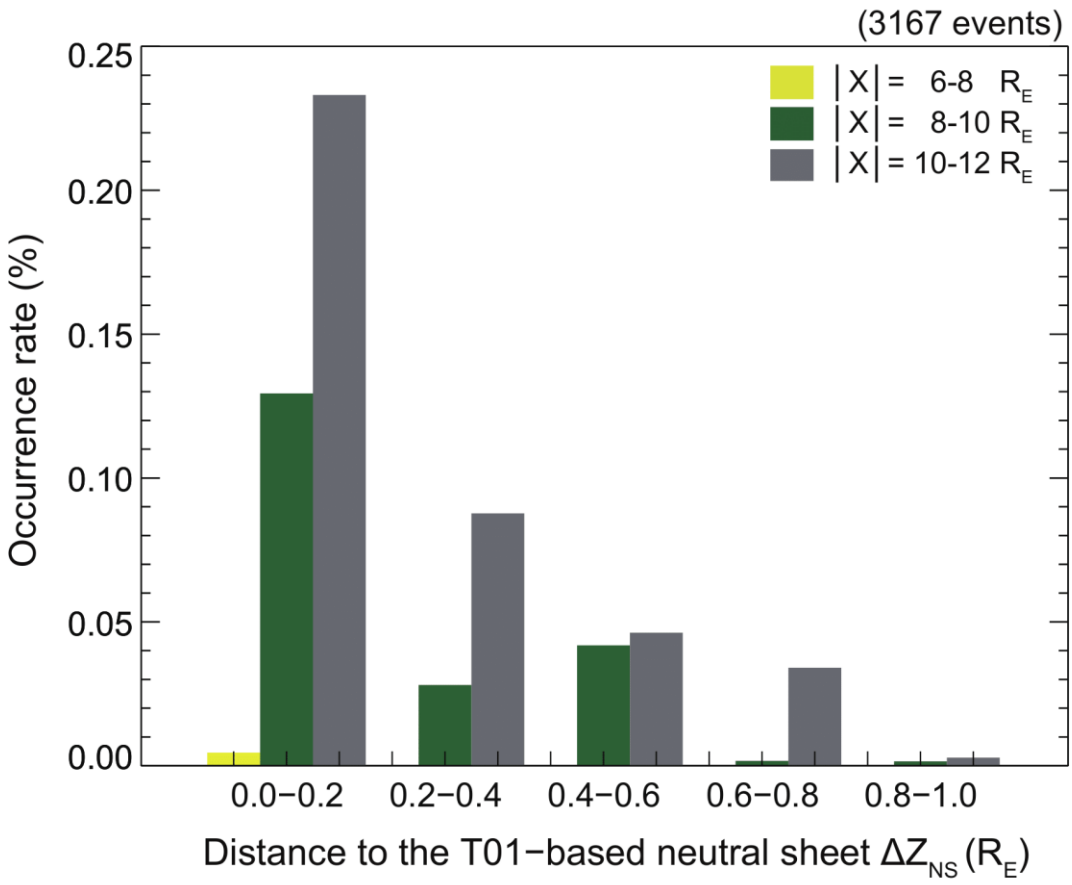

Figure 2.8 Occurrence rates of severe magnetic fluctuation events in three subregions with distance ΔZ_{NS} to the neutral sheet.

2.2.3 Superposed Epoch Analysis of the AL Index and Magnetic Field Variations

The amplitude lower (AL) index is often used to indicate the occurrence of substorms [e.g., Shiokawa and Yumoto, 1993]. In the calculation of the auroral electrojet (AE) index, the lower envelope of the north-south H-component perturbations observed at a series of stations near the auroral zone is defined as the AL index [Davis and Sugiura, 1966]. The AL index indicates the strength of the westward electrojet, because westward ionospheric current causes negative H-component perturbation observed on the ground. Nishida [1968] found that there is no clear relationship between the AE index and substorm onsets, while the AL index can indicate the substorm activity. Figure 2.9 shows the superposed epoch analysis of the AL index 1 h before and after the time of severe magnetic fluctuation events. A clear decrease in the AL index near the event time can be observed, suggesting that the

observed fluctuation events occurred near the substorm onsets or during the expansion phase of substorms. These results may indicate that either (1) these severe magnetic fluctuation events cause the substorms, or (2) these magnetic fluctuations result from the substorms.

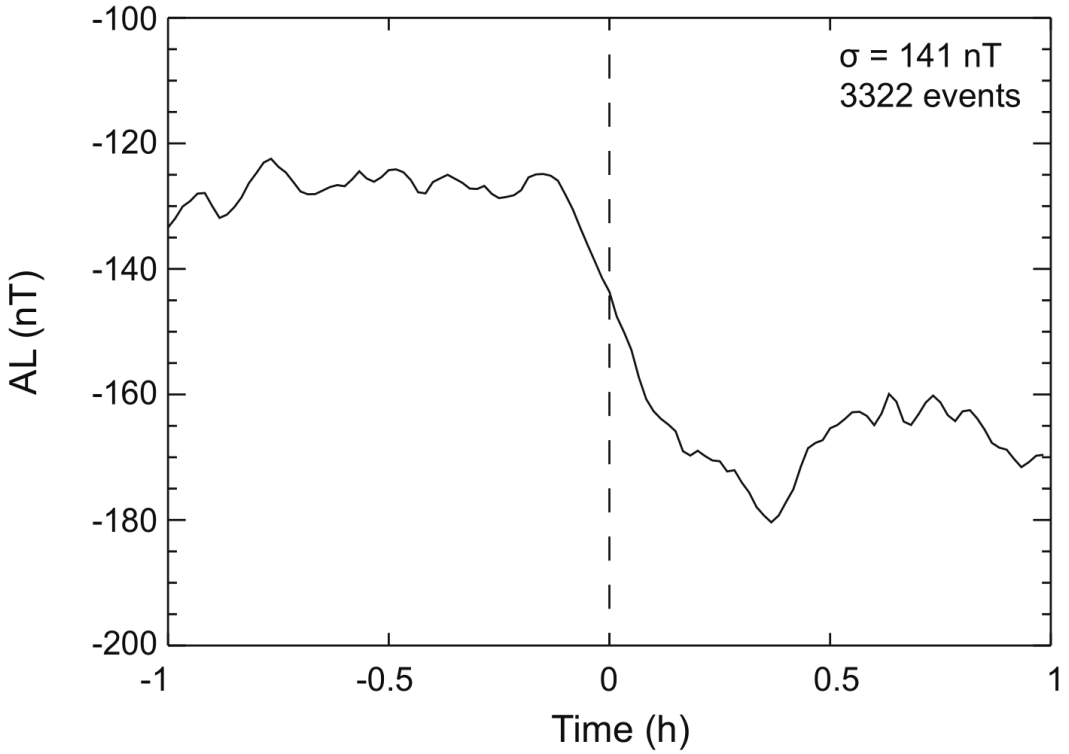

Figure 2.9 Superposed epoch analysis of the AL index for all 3322 events. The zero epoch is the time of each severe magnetic fluctuation event.

Figure 2.10 shows the superposed epoch analyses of magnetic field variations 1 h before and after the time of severe magnetic fluctuation events. The B_T is the total magnetic field intensity, $|B_x|$ is the absolute value of magnetic field component in X_{GSM}, B_y and B_z are magnetic field components in Y_{GSM} and Z_{GSM}, respectively. A clear decrease in $|B_x|$ and an increase in B_z after the fluctuation events can be seen in panels b and d, respectively. These results indicate the occurrence of magnetic field dipolarization near the fluctuation events [e.g., Baumjohann et al., 1999; Shiokawa et al., 2005b]. Figure 2.10 also shows abrupt decreases in B, $|B_x|$ and B_z on a timescale of 1–2 min before the fluctuation events. We defined the fluctuation events as $\sigma_B/\bar{B} > 0.5$. Those magnetic fluctuations with a sudden decrease in B would be selected out easily. The decrease in B_z during the dipolarization has been previously

reported and was attributed to the explosive growth phase [Ohtani et al., 1992], magnetic flux ropes [Slavin et al., 2003], nightside flux transfer events [Sergeev et al., 1992], B_y field accumulation at the flow front [Hashimoto et al., 2005], current disruption or substorm current wedge [Shiokawa et al., 2005b] and the dawnward currents because of the reflection of ions by the dipolarization front [Pan et al., 2015].

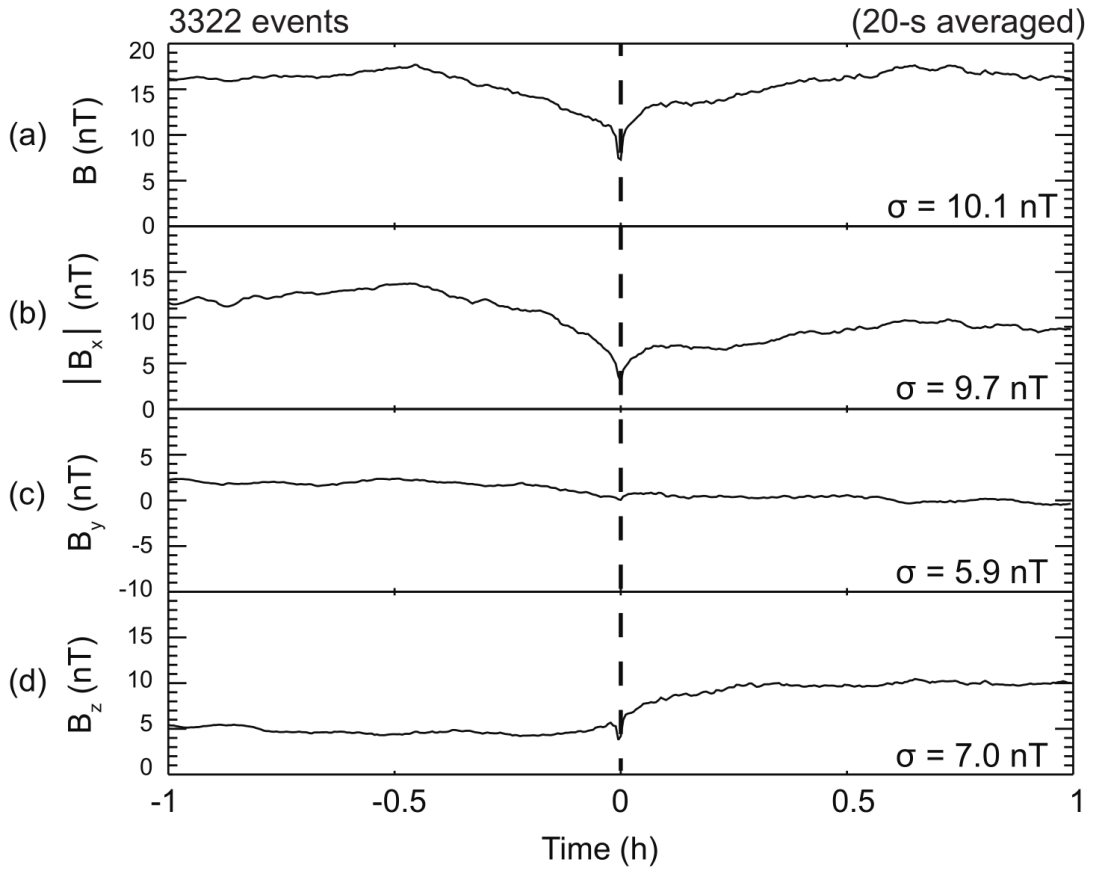

Figure 2.10 Superposed epoch analyses of the magnetic field variations for all 3322 events. The zero epoch is the time of each severe magnetic fluctuation event. This figure shows the results of (a) total magnetic field intensity, (b) absolute value of magnetic field component in X_{GSM}, (c) magnetic field component in Y_{GSM}, and (d) magnetic field component in Z_{GSM}.

2.2.4 Comparison with Plasma Flow Data

The relationship between magnetic fluctuations and fast plasma flows in the near-Earth magnetotail has been previously studied [e.g., Bauer et al., 1995; Vörös et al., 2004; Shiokawa et al., 2005a; Frühauff and Glassmeier, 2016]. In order to investigate the relationship between severe magnetic fluctuations and high-speed ion flow, we checked the plasma flow data obtained by the same THEMIS-E satellite. Figure 2.11 shows the distribution of 10 s averaged total ion speeds V at the times of all severe magnetic fluctuation events. The ion flow data were unavailable for 28 events. We found that 47 % of events are accompanied by ion flow with $V > 100$ km/s. This indicates that for half of cases the violation of ion gyromotion tends to occur during high-speed flow in the near-Earth plasma sheet. We also checked the sign of V_x, where V_x is the ion speed in the X_{GSM}. We found that 69 % of ion flows are earthward. These results suggest that either (case 1) the severe magnetic fluctuations are caused by high-speed ion flow, or (case 2) the magnetic fluctuations cause earthward ion flow by reducing the tailward pressure-gradient force due to current disruption, as suggested by the inside-out model. For case 2, the ion flow should be observed after the severe magnetic fluctuations.

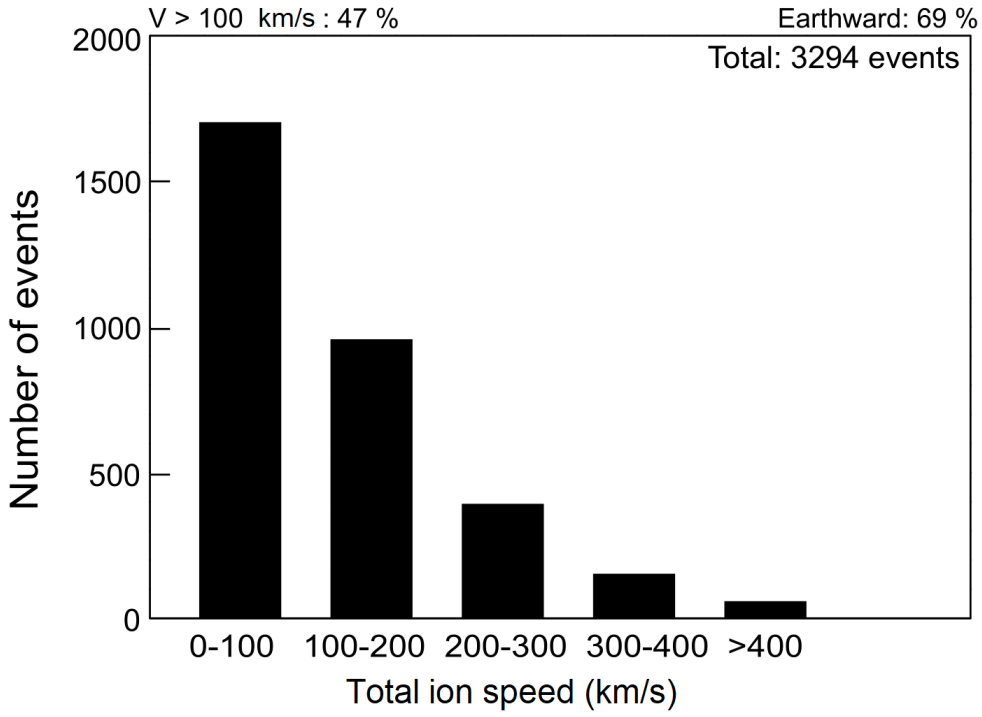

Figure 2.11 Distribution of 10 s averaged total ion speeds during severe magnetic fluctuation events.

Figure 2.12 shows the superposed epoch analysis of total ion speeds 1 h before and after the time of severe magnetic fluctuation events. We can observe an increase in average ion speed from ~10 min before the epoch time. This result indicates that the high-speed ion flow causes the severe magnetic fluctuations (case 1).

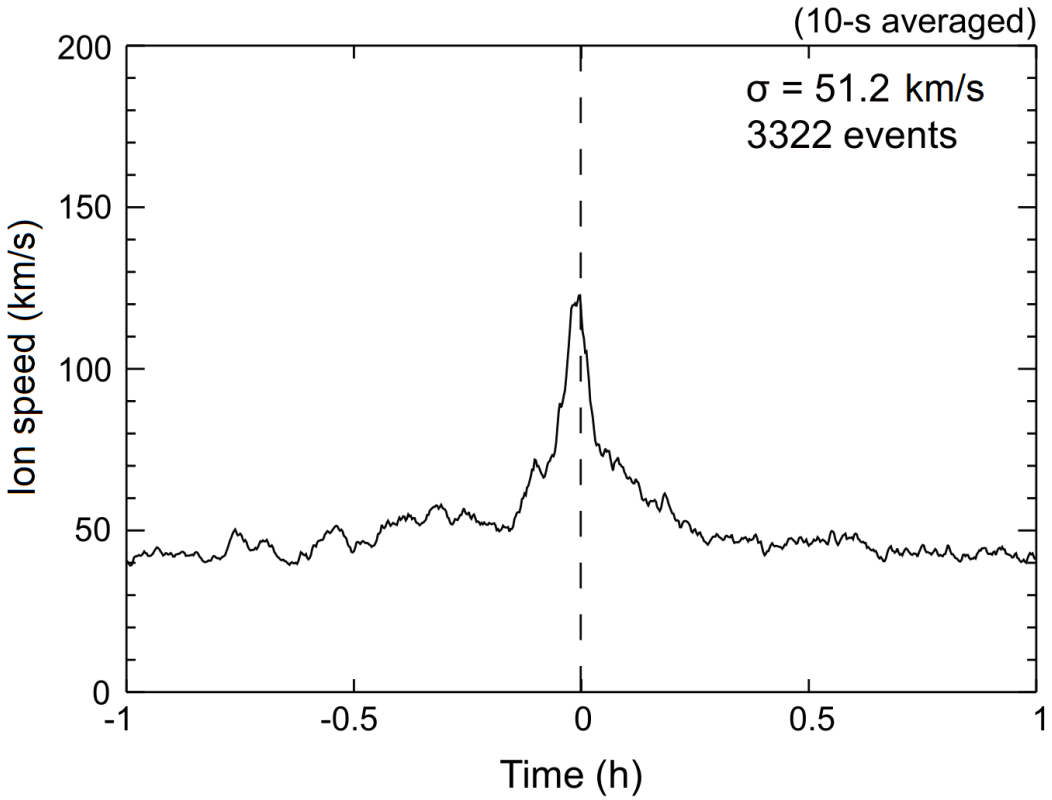

Figure 2.12 Superposed epoch analysis of total ion speeds 1 h before and after the time of severe magnetic fluctuation events.

To determine whether the magnetic fluctuations can cause the high-speed ion flow (case 2), we also made some further analyses. We calculated the average ion speed at 0–1 min before the time of severe magnetic fluctuation event, and selected the events (total 1744 events) for which the 1-min averaged ion speed is greater than the ion speed at the event time. The superposed epoch analysis of ion speeds for these 1744 events using the same format in Figure 2.12 is shown in Figure 2.13a. We can still observe an increase of average ion speed before the severe magnetic fluctuations. Figure 2.13b shows the superposed epoch analysis of ion speeds for 1151 selected events for which averaged ion speed at 0–10 min before the event time is greater than the ion speed at the event time. Again, we found that the average ion speed already increases before the fluctuation events.

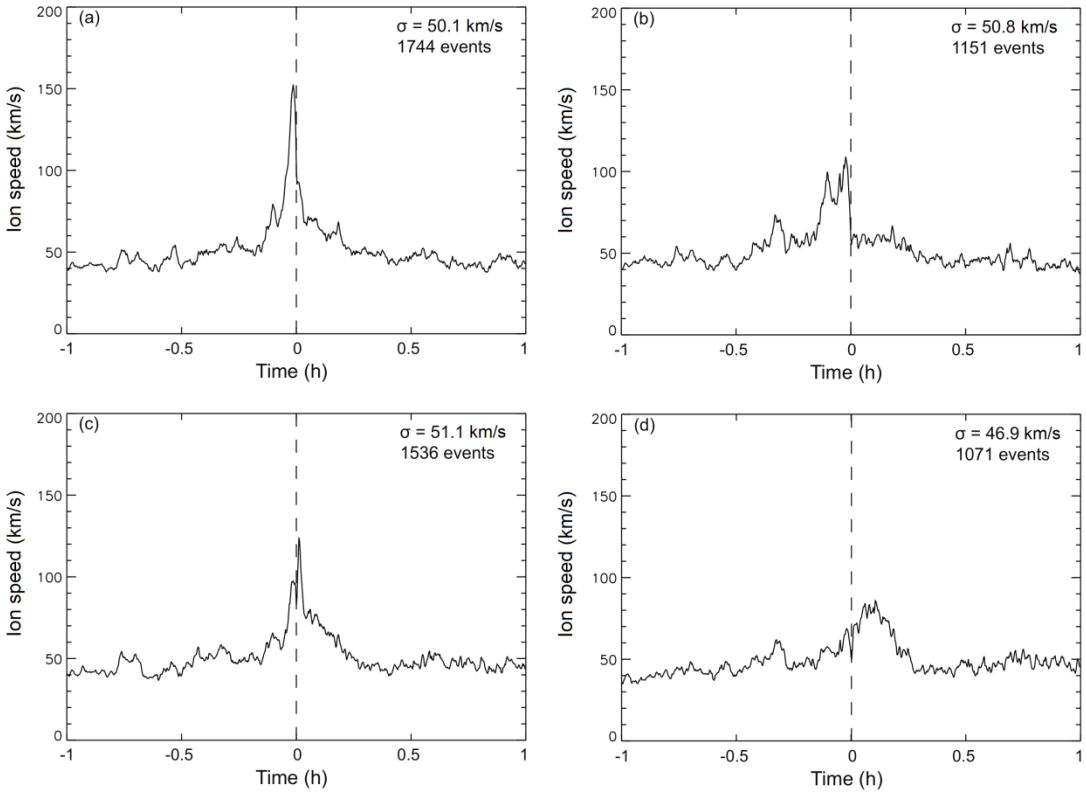

Figure 2.13 Superposed epoch analysis of total ion speeds 1 h before and after the time of severe magnetic fluctuation events. In panel (a), we calculated the average of ion speed at 0–1 min before the event time and then selected those events with a 1 min averaged ion speed greater than the ion speed at the event time. Panels b–d show the results with similar methods by changing the time intervals of average value calculation into 10 min before, 1 min after, and 10 min after the event time.

Figure 2.13c are similar superposed epoch plots of ion speeds for which the averaged ion speed at 0–1 min after the event time is greater than the speed at the event time. Figure 2.13d is for events where the average timescale is changed into 0–10 min after the event time. In these two panels, ion speed keeps in a relatively high level until ~10 min after the event time. The increase of average ion speed before the event time can still be observed. Meanwhile, the amplitude of the average ion speeds at ~1 min (~10 min) after the event time in Figure 2.13c (Figure 2.13d) is relatively small compared with the amplitude at ~1 min (~10 min) before the event time in Figure 2.13a (Figure 2.13b). These results in Figures 2.12 and 2.13 indicate that for most cases the severe magnetic fluctuations cannot be the cause of the high-speed ion flow.

We further discuss the observed increases in ion speeds before the severe magnetic fluctuations. Before a present observed severe magnetic fluctuation event, another fluctuation event (or current disruption) may occur at the tailward side of the satellite. This is because the thinned plasma sheet can be unstable everywhere at the end of the growth phase of substorm. Then, another fluctuation event can cause the observed increase in ion speed before the present severe magnetic fluctuation event. However, we believe that such a possibility is unlikely because the earthward plasma flow is generally accompanied by the dipolar magnetic field that stabilizes the plasma instability due to the thinning of the plasma sheet. Therefore, if the plasma instability that causes the current disruption is caused by the thinning of the plasma sheet, the present observation of ion flow enhancement before the magnetic fluctuation (or current disruption) contradicts the idea that the earthward flow is caused by the current disruption.

On the contrary, another magnetic fluctuation may also occur at the earthward side of the satellite. The current disruption due to another fluctuation event can cause subsequent current disruptions from the present to more tailward locations, even without additional instabilities. That is, the earthward plasma flow associated with the current disruption can cause depletion of the tailward pressure-gradient force at its location. This pressure decrease attracts plasma at the tailward side of its location, causing the plasma to move earthward sequentially as a rarefaction wave [e.g., Haerendel, 1992; Hwang et al., 2014]. Considering that the plasma flow can cause magnetic fluctuations, the possibility that the satellite detects the first severe magnetic fluctuation (or current disruption) without plasma flow may become smaller. In that sense, we cannot deny following possibility according to the inside-out model. The first magnetic fluctuation (current disruption) causes only the initial earthward plasma flow. Other earthward plasma flows and associated severe magnetic fluctuations will then occur subsequently. In such a case, the number of the severe magnetic fluctuation events after the increase of plasma flow speed may become dominant, as observed in Figures 2.12 and 2.13.

2.3 Conclusions

We used magnetic field data (sampling rate: 4 Hz) from 2013 and 2014 obtained by THEMIS-E to analyze severe magnetic fluctuation events in the magnetotail. In total, 3322 severe magnetic fluctuation events were identified with $R = \sigma_B/\bar{B} > 0.5$, where σ_B and $\bar{B}$ are the standard deviation and the average value of magnetic field intensity during the time interval of the local proton gyroperiod. Around 99.8 % of the fluctuation events had plasma beta values of more than 1, indicating that they occurred in the plasma sheet. The results of this chapter can be summarized as follows.

1. The occurrence rates of severe magnetic fluctuation events in the near-Earth magnetotail ($|X|$ = 6–12 R_E) are 0.00312 %, 0.0312 % and 0.0675 % at $|X|$ = 6–8 R_E, 8–10 R_E and 10–12 R_E, respectively. They occurred most frequently in Region C ($|X|$ = 10–12 R_E). The durations of most fluctuation events were less than 20 s. By assuming that four substorms with 5 min intervals of current disruption occur every day, we estimated the possible scale sizes of current disruption by severe magnetic fluctuations as 11.47 R_E^3 for the entire region (0.80, 8.02, and 17.36 R_E^3 at $|X|$ = 6–8, 8–10 and 10–12 R_E, respectively). We also found that the occurrence of magnetic fluctuations significantly decreases as their amplitude becomes larger from $R > 0.2$ to $R > 0.5$.

2. We found that the distances from the locations of severe magnetic fluctuation events to the T01-based neutral sheet are mostly less than 1 R_E. The bin with the highest occurrence rate of fluctuation events is located at $|X|$ = 11–12 R_E in the dusk side with a close distance to the neutral sheet ($\Delta Z_{NS} < 0.2$ R_E). The occurrence rate of fluctuation events is the highest at the neutral sheet, which is consistent with the typical location of current disruption in both the inside-out and outside-in models.

3. We made superposed epoch analysis of various data 1 h before and after the time of severe magnetic fluctuation events. The result of AL index shows an obvious decrease in index value near the event time. An increase in B_z and a decrease in $|B_x|$ are observed during fluctuation events, indicating the occurrence of magnetic field dipolarization. These results suggest that the observed fluctuation events occurred at substorm onset or during the substorm expansion phase. Temporal decreases in B, $|B_x|$, and B_z on a timescale of 1–2 min before the time of fluctuation events are also observed.

4. Forty-seven percent of severe magnetic fluctuation events are accompanied by

ion flow speed with $V > 100$ km/s. This fact indicates that for half of cases the violation of ion gyromotion tends to occur during high-speed ion flow in the near-Earth magnetotail. The superposed epoch analysis of ion flow speed shows an increase in speed value before the magnetic fluctuation events, which suggests that for most cases the severe magnetic fluctuations cannot be the cause of the high-speed ion flow. We discuss how both the inside-out and outside-in substorm models can explain this increase in ion flow speeds before fluctuation events.

Chapter 3
Spectral Analysis of Severe Magnetic Fluctuations in the Near-Earth Magnetotail

This chapter presents the spectral analysis of severe magnetic fluctuations at substorm onsets in the near-Earth magnetotail. This is an expanded study of the results in Chapter 2. We selected magnetic field dipolarization events with severe magnetic fluctuations, and applied Fast Fourier Transform (FFT) to total magnetic field intensity to obtain power spectral densities (PSDs) of magnetic field fluctuations associated with substorms. We discussed the dependence of PSD on distance to the neutral sheet and ambient magnetic field intensity. We also showed the relationship between the occurrence rates of severe magnetic fluctuations and solar activity in a complete solar cycle.

3.1 Selection of Dipolarization Events and Dependence of Magnetic Fluctuations on Solar Activity

Dipolarization can be defined as an increase of elevation angle (= arctan(B_z/B_{xy})) of magnetic field in the GSM coordinates, where B_{xy} is the magnetic component in the GSM-*XY* plane. As one signature of substorm onset, dipolarization is often accompanied by magnetic fluctuation [e.g., Jacquey et al., 1991]. Our method used in the statistical analysis of Chapter 2 already indicated that those magnetic fluctuations at or near substorm onset tend to be selected. In order to focus on those long-lasting and substorm-onset-related fluctuation events, we further selected 36 dipolarization events during the multiple-fluctuation events defined in Chapter 2. The detailed method is described below.

At first, we analyzed the observation data of both THEMIS-D and E probes at 2008–2018 using the definition of severe magnetic fluctuation in Chapter 2. We have found 10848 severe magnetic fluctuation events in total. Here, we compared the occurrence rates of these severe magnetic fluctuations with the averaged $F_{10.7}$ indices, because the analyzed times covered nearly a whole solar cycle. In Figure 3.1a, bars

indicate the occurrence rates of severe magnetic fluctuation events in each subregion, and the red curve shows the $F_{10.7}$ index averaged over 2 years (1 year for 2018). Figure 3.1.b indicates the total observation times in each subregion. We cannot see clear relationship between the occurrence rates of severe magnetic fluctuations and the solar activity.

The dependences of occurrence rates of substorms on solar cycle or solar wind conditions have been investigated by previous studies [e.g., Nevanlinna and Pulkkinen, 1998; Borovsky and Yakymenko, 2017]. Borovsky et al. [1993] speculated that the mean time of 5 h between randomly occurring substorms is related to the solar wind variation with a 5-h timescale. Chu et al. [2015] found that the occurrences of substorms have clear dependence on solar wind speed rather than solar cycle phases. However, some studies pointed out that the occurrences of substorms peak in the declining phase of solar cycle [e.g., Tanskanen et al., 2011; Borovsky and Yakymenko, 2017], which is because the equatorward extension of coronal holes on the Sun during the declining phases can result in long-lasting high-speed plasma at Earth [McAllister et al., 1996]. In Figure 3.1, there is no clear peak in the occurrence rates of severe magnetic fluctuations in the declining phase at 2016–2017. This is reasonable because magnetic fluctuation is only one of various mechanisms to trigger or associate substorm.

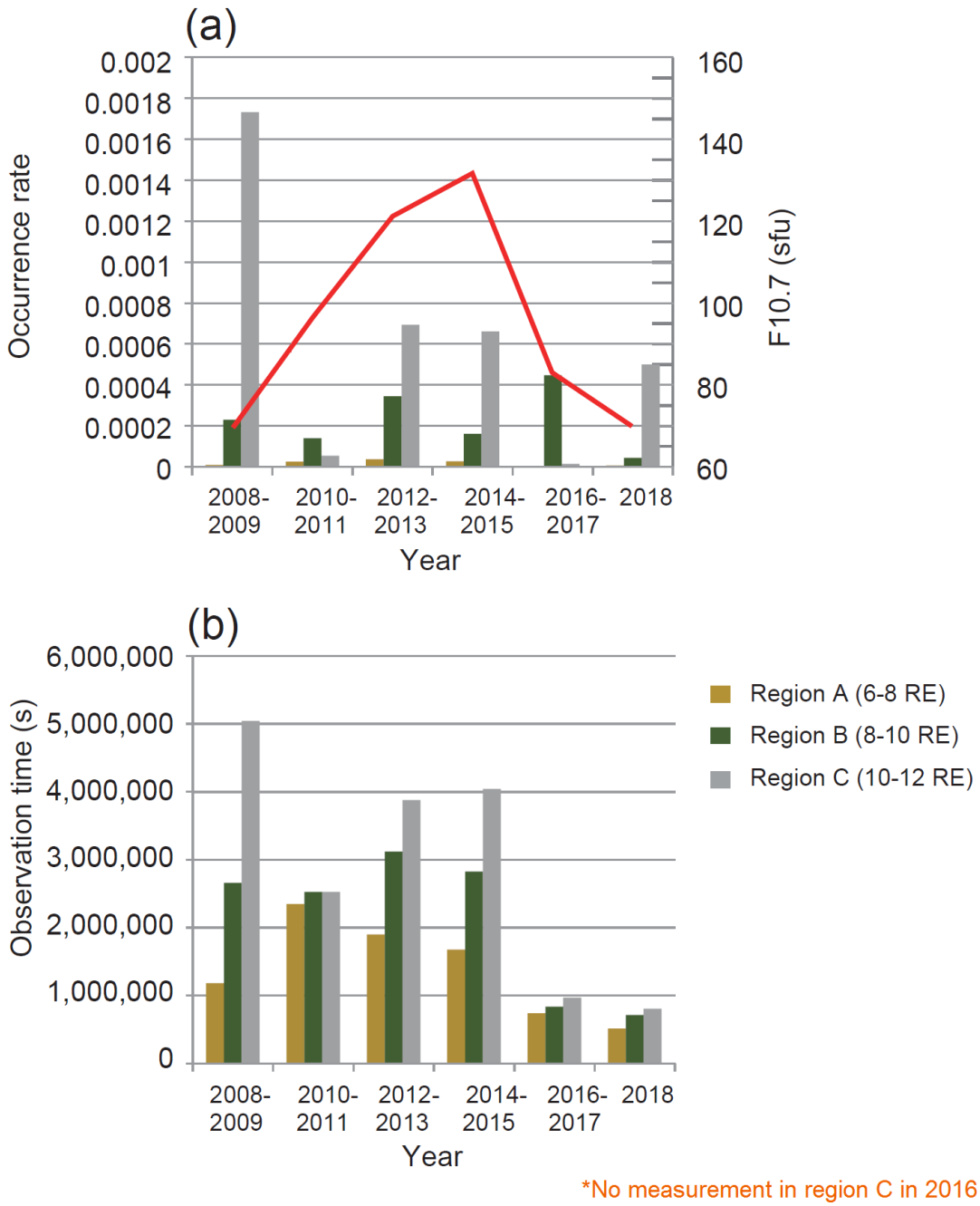

Figure 3.1 Comparison of the occurrence rates of severe magnetic fluctuations and solar activity. (a) Occurrence rates in each subregion and the $F_{10.7}$ index averaged over 2 years except for 2018. (b) Total observation times in each subregion.

Based on these selected severe magnetic fluctuation events, we then applied following criteria to obtain dipolarization events with considering previous studies [e.g., Schmid et al., 2011; Schmid et al., 2016]:

1. Location: Event should be located at (X_{GSM}, Y_{GSM}, Z_{GSM}) = (-9 ±3, ±5, ±3) R_E in GSM coordinates, which was already applied in the initial selection of severe magnetic fluctuation events.

2. Duration: The time difference between first and last severe magnetic fluctuation events is 5–30 min, which is named as the window.

3. Elevation Angle: In the window, at the times of minimum and maximum B_z, the difference in elevation angle and B_z value exceeds 10 °and 4 nT, respectively. The elevation angle is at least in one data point greater than $\theta_{max} \geq 45$ °within the window. Maximum B_z occurs later than the minimum B_z within the window.

4. Additional Criteria: In order to exclude those events with other dipolarization occurs before the window, or severe elevation angle change before the window, we further ensured that the mean elevation angle during the window is 10 degree larger than the mean elevation angle for 30 min before the window, and the standard deviation of the elevation angles for 30 min before the window is less than 15 degree.

From these criteria, we obtained 36 dipolarization events during multiple-fluctuation events. Figure 3.2 indicates the locations of these dipolarization events in GSM-*XY* and X_{GSM}-ΔZ_{NS} planes, where ΔZ_{NS} indicates the distance to the neutral sheet using the T01 model. Most events were located close to the neutral sheet within 1 R_E, which is consistent with the basic assumption of inside-out substorm model as well as our previous statistical analysis in Chapter 2.

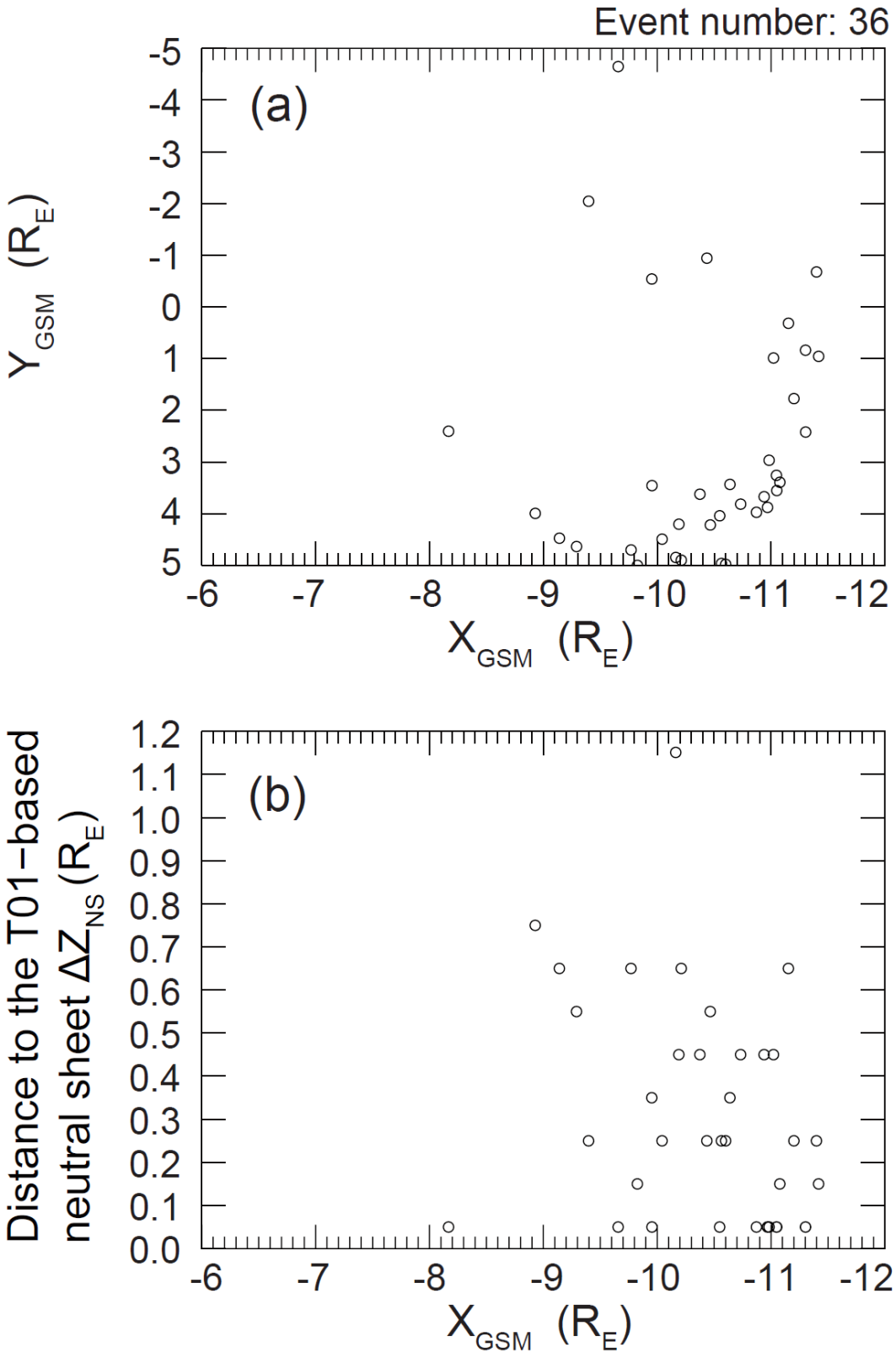

Figure 3.2 Spatial distribution of 36 dipolarization events during multiple-fluctuation events in (a) GSM-*XY* and (b) X_{GSM}-ΔZ_{NS} planes.

In Figure 3.3, we provide variations of the magnetic field intensity for the selected 36 dipolarization events. The data are from -30 to +60 min to the first severe magnetic fluctuation event. The first and last severe magnetic fluctuation events are indicated by the vertical blue line and vertical red line, respectively. We can observe strong and long-lasting variations in magnetic field during the window time of each event.

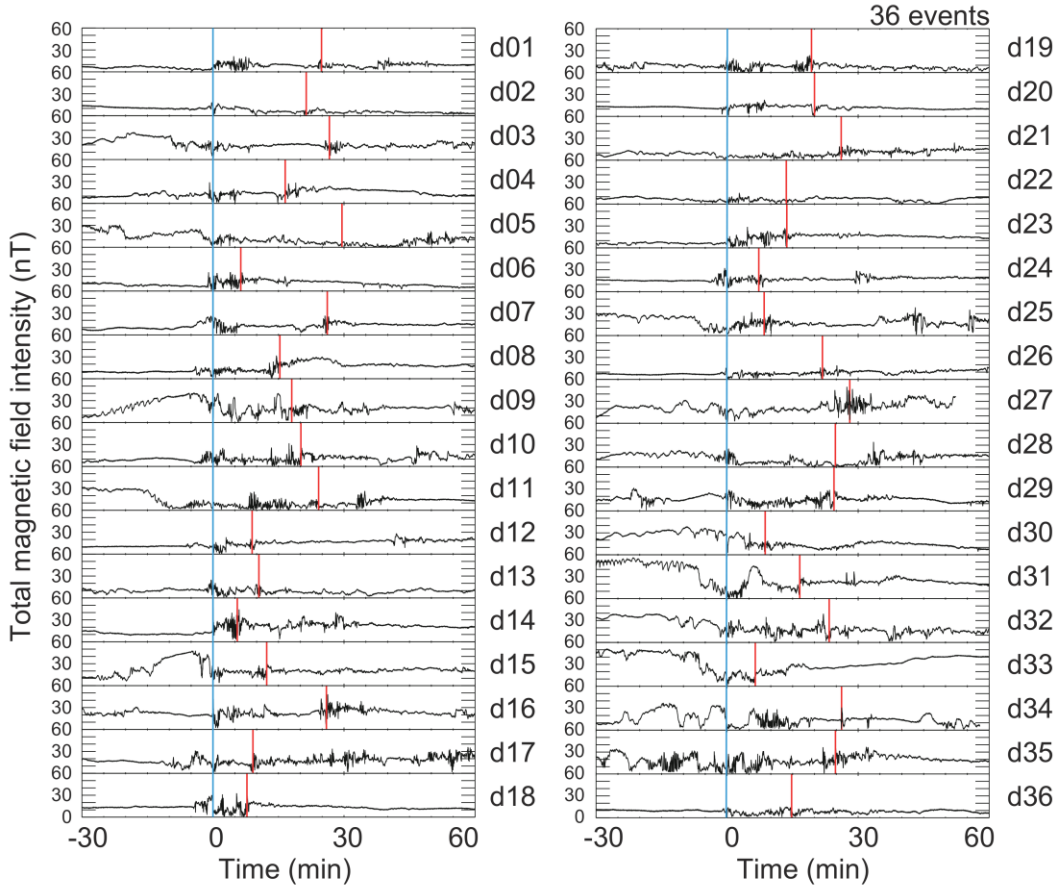

Figure 3.3 Variations of the magnetic field intensity of selected 36 dipolarization events. The data are from -30 to +60 min to the first severe magnetic fluctuation event. The first and last severe magnetic fluctuation events are indicated by the vertical blue line and vertical red line, respectively.

In Figure 3.4, we show variations of elevation angle of magnetic field during the 36 dipolarization events using the similar format in Figure 3.3. We calculated the 10-min averages of elevation angle before and after the vertical blue line. The subtraction between two averages indicates the increase of elevation angle before and after the dipolarization, which is shown in each panel. We can observe a clear increase of elevation angle after the start of window time (vertical blue line), indicating that the magnetic field became more dipole like. The dipolarization feature is a signature of substorm onset.

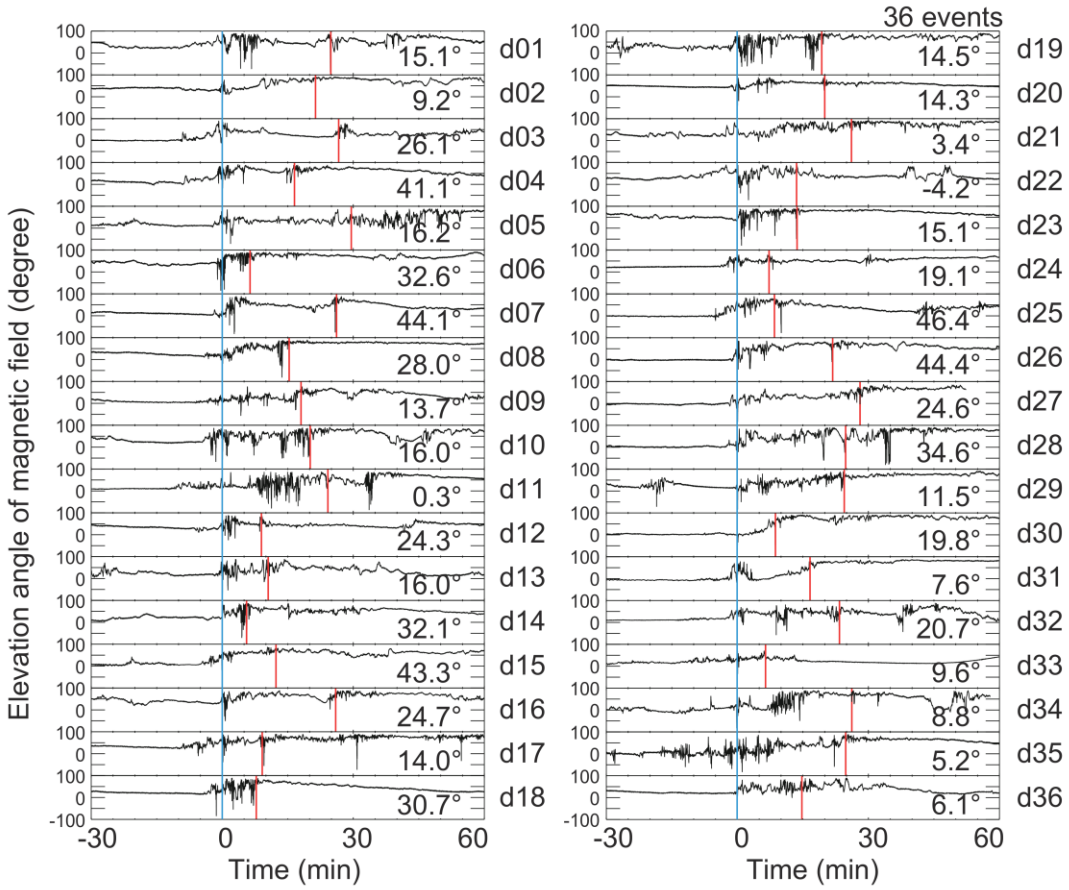

Figure 3.4 Variations of elevation angle of magnetic field during the 36 dipolarization events using the similar format in Figure 3.3. The increase of elevation angle indicates that the magnetic field became more dipole like.

3.2 Spectral Analysis of Magnetic Fluctuations and Discussion

For each dipolarization event, we applied FFT to the magnetic field intensity data and calculated their PSDs. The time window for the FFT analysis was chosen as 512 seconds from the first severe magnetic fluctuation event, instead of the window

time. We averaged the PSD in every eight data point in the frequency domain, providing an equivalent degree of freedom of 8. We show the PSD curve in log-log plot.

Then, we divided the 36 dipolarization events into three groups sorted by (a) the distance to the neutral sheet and (b) ambient magnetic field intensity. In each group, we calculated the average and standard deviation of PSD values at each frequency point using all PSD curves, because we would like to calculate a slope of the PSD in log-log plot which corresponds to the gradient of power law. Figure 3.5 shows the PSDs of magnetic fluctuations for all 36 dipolarization events. We can see that the steepness of the spectral slope increases with increasing frequency for almost all the events.

Finally, we calculated the gyrofrequency of proton in each event using the average ambient magnetic field intensity during the 512 seconds in the FFT analysis. For each group in (a) and (b), we calculated the average of the proton gyrofrequency f_g for all events. Then we applied a linear least-square fitting at frequency ranges of 0.05 Hz–f_g and f_g–1 Hz in average PSD curve to obtain power law parameters. Previous studies showed that the power law of the PSD has a kink point at around 0.05–1 Hz [e.g., Shiokawa et al., 2005a].

Figure 3.6 shows the average PSDs of magnetic fluctuations during dipolarization events, where the events are divided by the distance to the T01-based neutral sheet ΔZ_{NS}. The ΔZ_{NS} in each dipolarization event is the averaged value during window time. The red and blue lines indicate the linear regression lines at 0.05 Hz–f_g and f_g–1 Hz, respectively. The error bar is the standard deviation of PSD values at each frequency point using all PSD curves. We show the error bars every 8 data points. In the group with $\Delta Z_{NS} < 0.1\ R_E$, we cannot observe clear change of slope in average PSD from these two fitted lines at 0.05–1 Hz, which is different from the results of Shiokawa et al. [2005a] by the GEOTAIL satellite at $|X| = 8$–$11\ R_E$. In the group with $\Delta Z_{NS} > 0.45\ R_E$, the slope of PSD becomes deeper at higher frequency range within 0.05–0.1 Hz, which is similar to that of Shiokawa et al. [2005a] for events at small ambient magnetic field. For all three groups, the slope of average PSD changes steeper abruptly from below ~$10^{-1.3}$ Hz to above ~$10^{-1.3}$ Hz (0.05 Hz). This may indicate that enhanced power of magnetic fluctuation near ~$10^{-1.3}$ Hz (0.05 Hz), which is slightly lower than f_g.

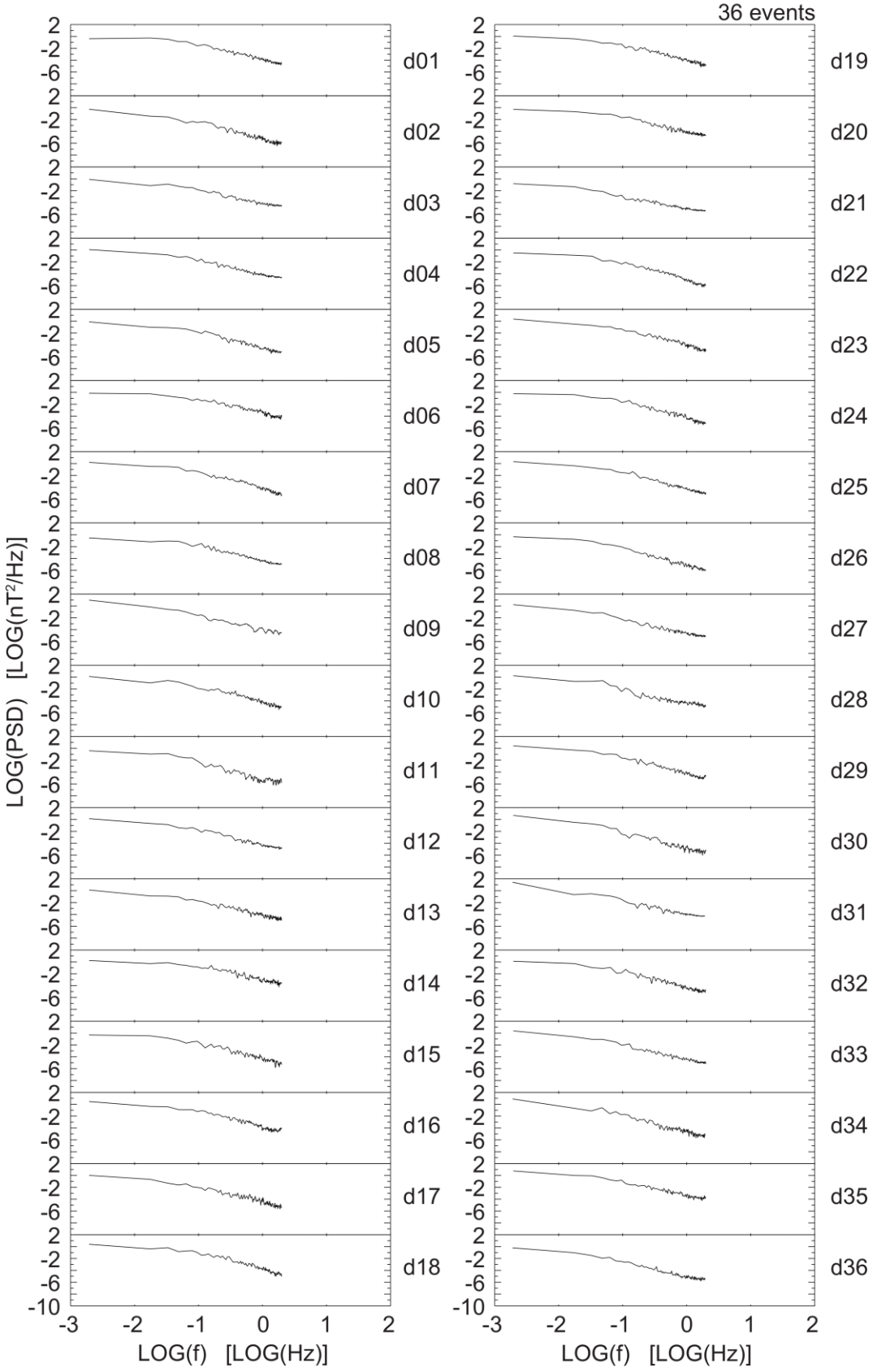

Figure 3.5 The PSDs of magnetic fluctuations for all 36 dipolarization events.

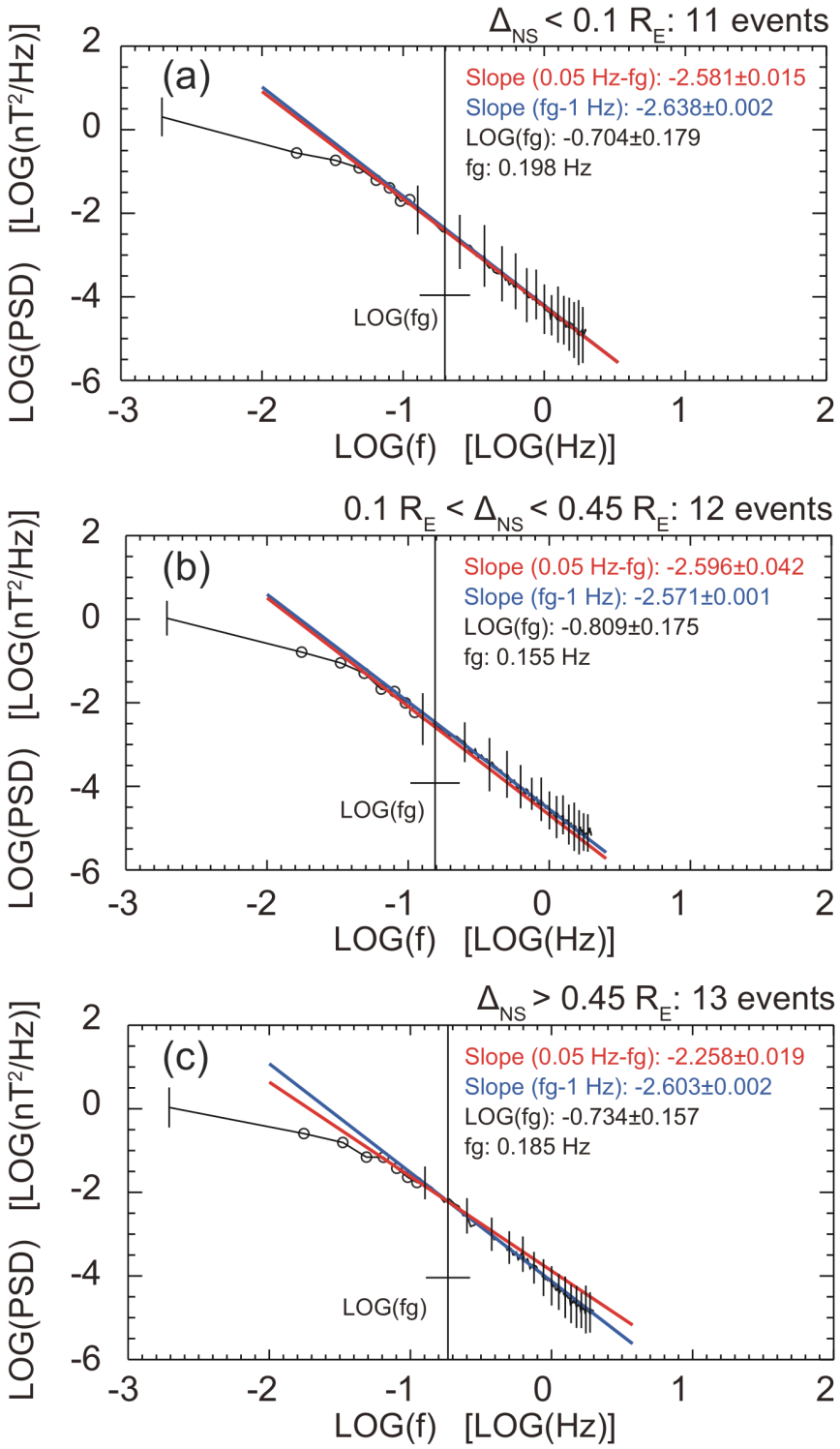

Figure 3.6 Average PSDs of magnetic fluctuations during dipolarization events, where the events are divided by distance to the T01-based neutral sheet ΔZ_{NS}. The red and blue lines indicate the fitting results at 0.05 Hz–f_g and f_g–1 Hz, respectively. We emphasized all the data points using circles between the leftmost two error bars.

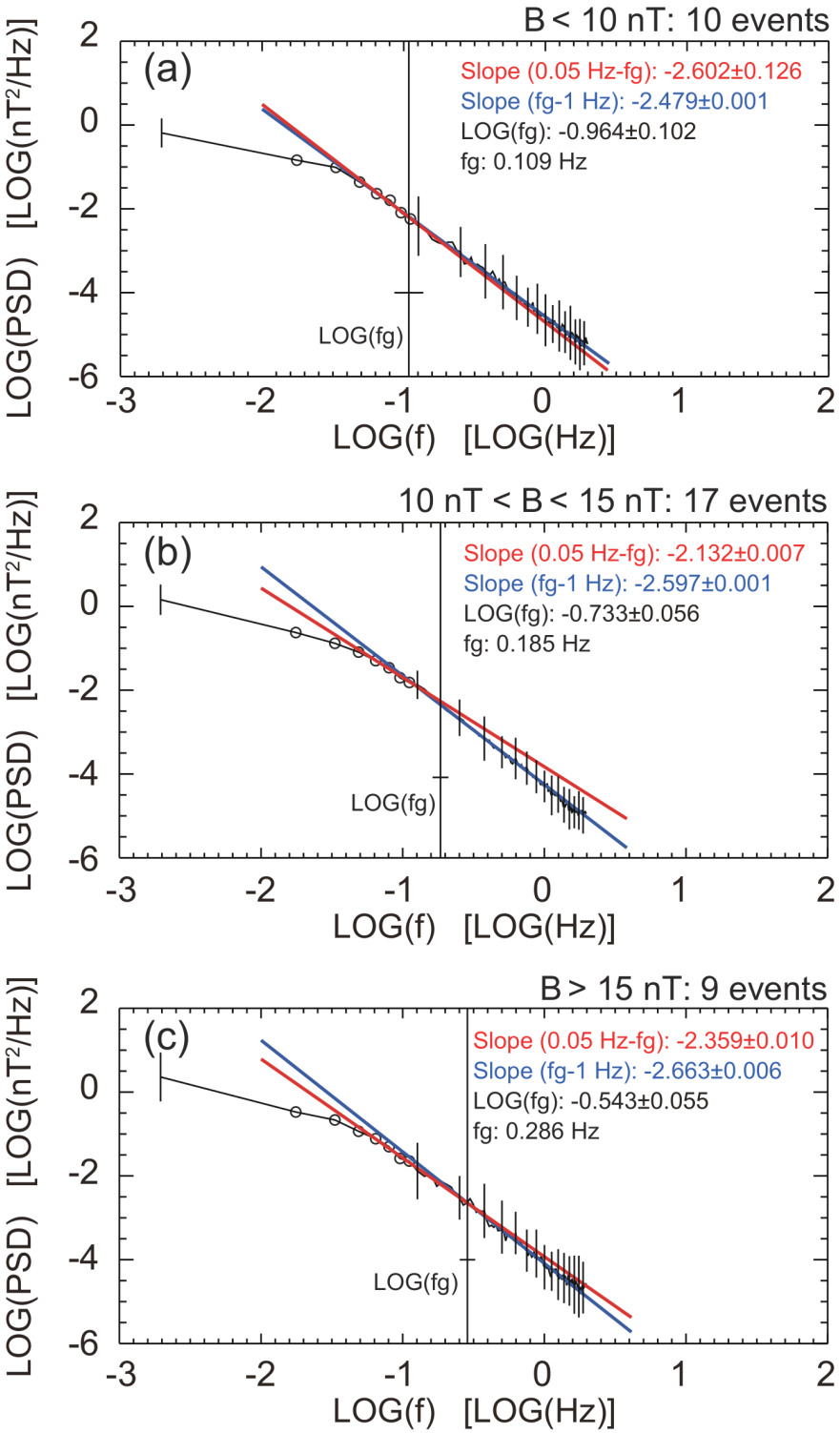

Figure 3.7 Average PSDs of magnetic fluctuations during dipolarization events, where the events are divided by ambient magnetic field intensity. The red and blue lines indicate the fitting results at 0.05 Hz–f_g and f_g–1 Hz, respectively.

Magnetic fluctuation at a frequency near the proton gyrofrequency may severely affect the proton motion and cause the non-MHD effect. The proton gyrofrequency in the magnetotail depends on the ambient magnetic field intensity, which is further related to both radial distance to the Earth and distance to the neutral sheet. Figure 3.7 shows the average PSDs of magnetic fluctuations during dipolarization events, where the events are divided by ambient magnetic field intensity. This plot used similar format to that in Figure 3.6. The ambient magnetic field intensity of each dipolarization event is the averaged value over the 512 seconds of FFT analysis. From panels a to c, we see the increase of f_g with stronger ambient magnetic field intensity. Similar with Figure 3.6, it seems that the slope of average PSD changes steeper abruptly from below ~$10^{-1.3}$ Hz to above ~$10^{-1.3}$ Hz (0.05 Hz). We also see a clear increase of slope at 0.05–0.1 Hz, as can be seen in the difference of the two fitted lines in panels b and c. It seems that the intersection of two fitted lines is related to the f_g in these two panels, which may imply that magnetic fluctuations near f_g have a relatively strong power and contribute to the non-MHD effect in proton motion.

The physical meaning of slopes in PSDs has been summarized and discussed in Shiokawa et al. [2005a]: (a) A three-dimensional (3D) magnetic turbulence should has a Kolmogorov slope of -5/3 [Volwerk et al., 2003], which is comparable to the observed slopes of -2.0 at lower frequency range in PSDs; (b) A slope of -3.0 occurs in a two-dimensional (2D) magnetic turbulence [Frisch, 1995], which is similar to the observed slopes of -2.7 at higher frequency range in PSDs; (c) The abrupt increase and different slopes near fg may indicate the change of turbulence from 3D to 2D.

In this study, we can see similar change of magnetic turbulence from 3D to 2D from below f_g to above f_g in Figures 3.7 b and c. We concluded that the slopes of fitted lines (-2.663 to -2.132) are generally comparable with the values found in previous studies by the GEOTAIL satellite [Shiokawa et al., 2005a]. In the signal analysis, a PSD with a peak at 0.05 Hz can represent intermittent pulses with period of 20 s. We also checked the 512-sec plots of magnetic field intensity in FFT analysis for all the dipolarization events. We found that it is hard to identify such burst signal with period of ~20 s by visual inspection.

It should be noted that we only consider proton (H^+ ions) in previous discussions about the gyrofrequency of ion. Figure 7 of Nosé et al. [2014] summarized the dominant frequency of magnetic fluctuations in the near-Earth magnetotail reported in several previous studies. It seems to be a common phenomenon that the magnetic

fluctuations have a dominant frequency less than f_g but close to the f_{go+} (gyrofrequency of O^+). Nosé et al. [2014] concluded that the magnetic fluctuations during dipolarization can accelerate O^+ ions efficiently, while no clear acceleration is seen in H^+ ions. The peak in PSDs at ~$10^{-1.3}$ Hz (0.05 Hz) found in this study is located between f_{go+} and f_g, which is consistent with these previous studies.

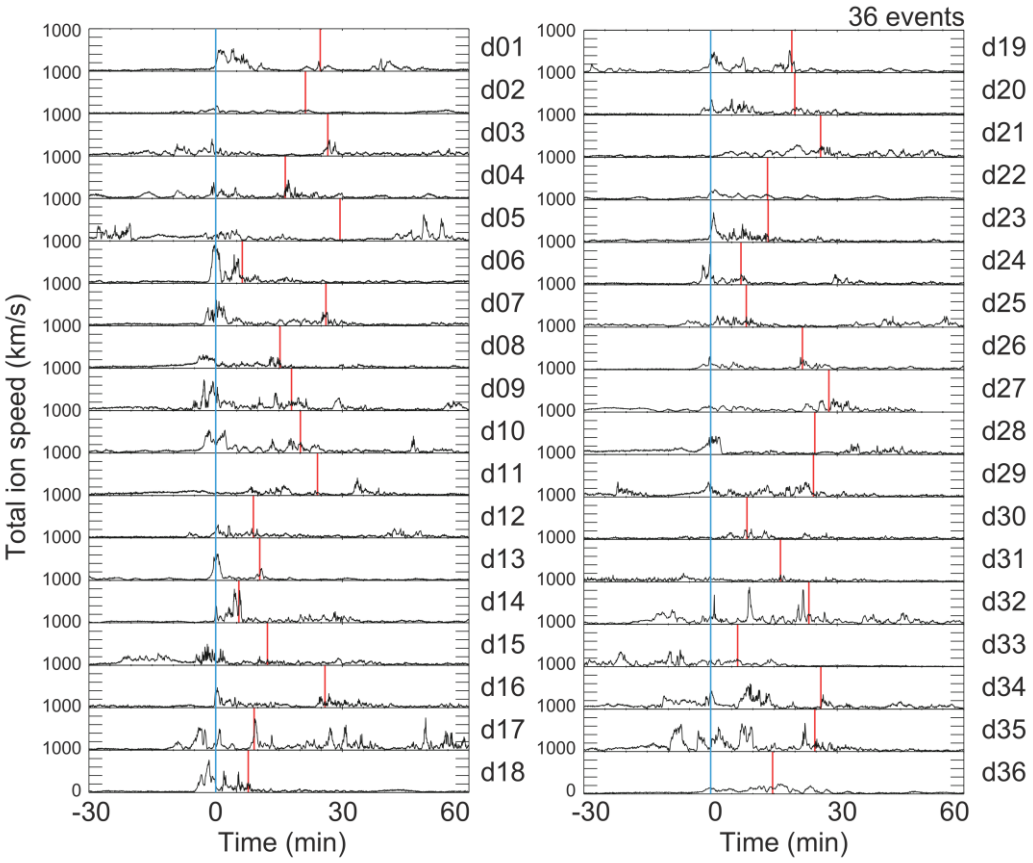

Figure 3.8 Total ion speed accompanied with severe magnetic fluctuations during dipolarization events, using the similar format in Figure 3.3.

3.3 Accompanied Plasma Flows

Figures 3.8 and 3.9 indicate the total ion speed and ion speed in X_{GSM} direction accompanied with severe magnetic fluctuations during dipolarization events, using the similar format in Figure 3.3. We can observe a clear increase of total ion speed during or near the window time of the dipolarization events for most cases. Twenty one of dipolarization events out of 36 are accompanied by earthward high-speed ion flow with V_{Total} > 200 km/s. For thirty of dipolarization events, the total ion speed already started to increase before the dipolarization. These results are consistent with our statistical

analysis in Chapter 2, indicating that for most cases the earthward plasma flows cause magnetic fluctuations in the near-Earth magnetotail.

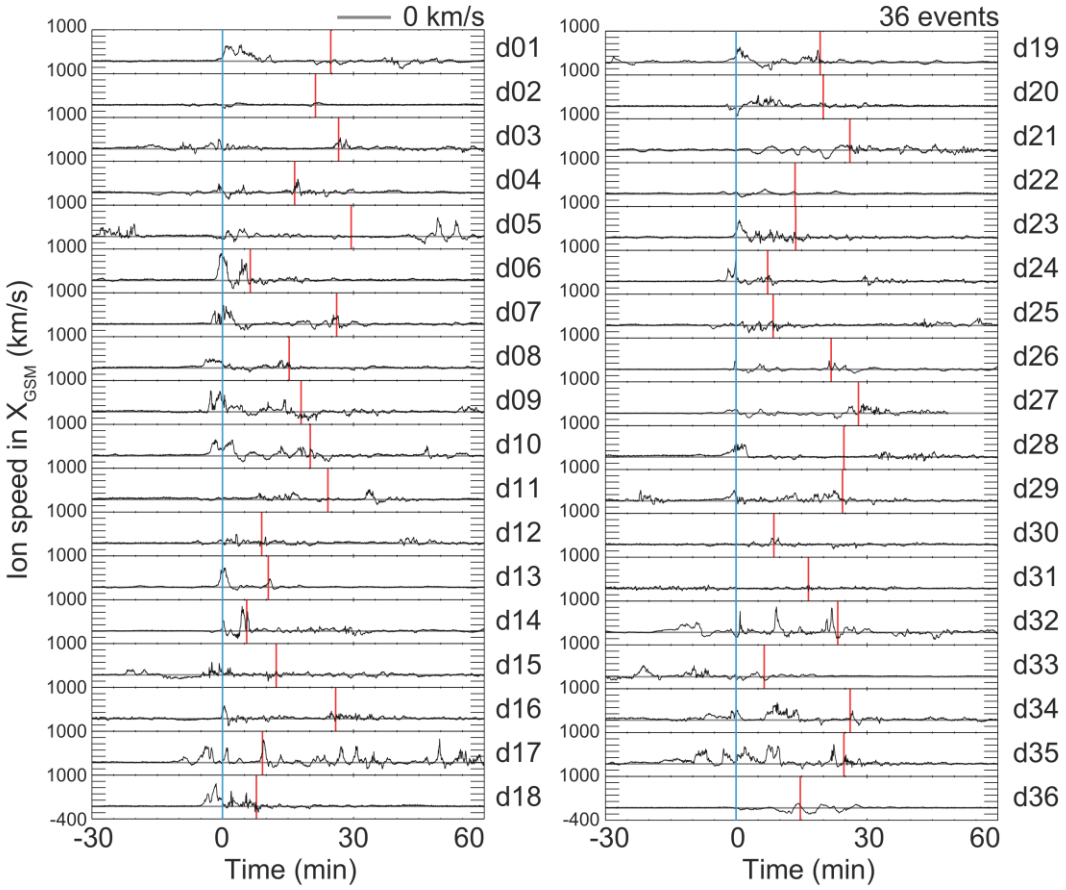

Figure 3.9 Ion speed in X_{GSM} direction accompanied with severe magnetic fluctuations during dipolarization events, using the similar format in Figure 3.3.

3.4 Conclusions

We focused on the spectral analysis of severe magnetic fluctuations in the near-Earth magnetotail. We analyzed the observation data of both THEMIS-D and E probes at 2008–2018 at $|X|$ = 8–12 R_E in the magnetotail, and found 10848 severe magnetic fluctuation events using the same criterion in the statistical analysis in Chapter 2. We then extracted 36 dipolarization events based on the elevation angle of magnetic field, and investigated the spectral property of magnetic fluctuations. Our main results can be summarized as follows.

1. We cannot see clear relationship between the occurrence rates of severe magnetic fluctuations and the solar activity in a complete solar cycle.

2. Most dipolarization events are located close to neutral sheet within 1 R_E, which is consistent with the basic assumption of inside-out substorm model as well as our previous statistical study in Chapter 2.

3. We calculated the PSD of magnetic fluctuations during dipolarization events, and found that the steepness of the spectral slope increases with increasing frequency for almost all the events. We also showed the average PSDs of magnetic fluctuations during dipolarization events sorted by (a) the distance to neutral sheet and (b) ambient magnetic field intensity. In all groups, the slope of average PSD changes steeper abruptly from below ~$10^{-1.3}$ Hz to above ~$10^{-1.3}$ Hz (0.05 Hz). This peak in PSD at ~$10^{-1.3}$ Hz (0.05 Hz) is located between the gyrofrequency of H^+ and O^+ ions, which is consistent with previous results. The slopes (-2.663 to -2.132) of fitted lines in PSDs at 0.05–0.1 Hz are generally comparable with the values found in previous studies as well.

4. We see a clear increase of slope in average PSD at 0.05–0.1 Hz in two groups with larger ambient magnetic field intensity. The intersection of two fitted lines is related to the gyrofrequency of proton f_g, which may imply that magnetic fluctuations near f_g have a relatively strong power and contribute to the non-MHD effect in proton motion.

5. Twenty one of dipolarization events were accompanied by earthward high-speed ion flow with V_{Total} > 200 km/s. For thirty of dipolarization events, the total ion speed already started to increase before the dipolarization. These results are consistent with our statistical analysis in Chapter 2, suggesting that for most cases the earthward plasma flows cause magnetic fluctuations in the near-Earth magnetotail.

6. Compared with previous researches, this study found several dipolarization events and showed their spectra of magnetic fluctuations with a wider radial distance coverage at 8–12 R_E. Lui et al. [1992] and Ohtani et al. [1998] showed the spectra in separate magnetic component, while this study demonstrated the spectra of total magnetic field intensity similar to that of Shiokawa et al. [2005].

Chapter 4
High-latitude Thermospheric Wind Variations at Local Substorm Onsets

This chapter focuses on the substorm onset mechanisms in the ionosphere. For the first time, we showed the characteristics of thermospheric wind variations at local substorm onsets at high latitudes. The wind data were collected by an FPI at Tromsø, Norway. We discussed how the observed thermospheric wind variations could provide a feedback to the development of substorm expansion phase in the near-Earth magnetotail. We also discussed possible causes of the observed wind variations. The contents described in this chapter have been published by Xu et al. [2019a].

4.1 Instrumentation

The FPI used in this study is located in Tromsø, Norway (69.66 °N, 18.94 °E in geographic coordinates). The local time (LT) is 1 h ahead of UT at Tromsø, while magnetic local time (MLT) at Tromsø is ~2.5 h ahead of UT. In one set of measurement, this FPI scans the sky in the five directions of north, west, south, east, and zenith. In each direction, the 630.0 nm and 557.7 nm emissions are observed in sequence. The elevation angle of the sky scan is 45 °. As shown in Figure 4.1, we plot the field-of-view (FOV) of the FPI sky scan over an example all-sky auroral image. The FOV in each direction is 5 °in full angle as indicated by the white circles [Shiokawa et al., 2012].

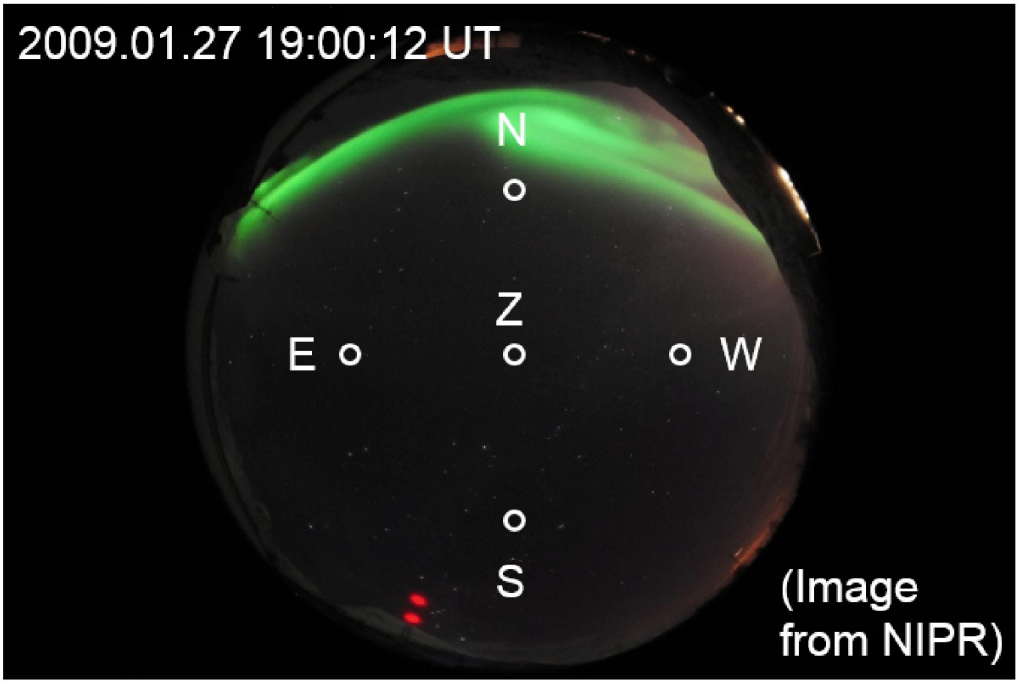

Figure 4.1 The FOV of FPI measurement. The FPI scans the sky in the five directions of north, west, south, east, and zenith. The elevation angle is 45 °. The FOV of the five directions are plotted over the all-sky auroral image, as indicated by the white circles. The FOV in each direction is 5 °.

As described by Shiokawa et al. [2012], this FPI takes images of more than ten interference fringes per exposure. From the Doppler shift of the peak locations of the inner ten fringes from the center, ten individual wind speeds can be determined per exposure. Therefore, there are ten values in the result of each wind measurement. In this study, we used the arithmetic mean v_i of the ten values as the measurement result, and the standard deviation σ_i of the ten values as the random error of the measurement due to count statistics. Because of a lower count rate, the random error increases when the intensity of the emission is weak. We abandoned wind measurements with unreasonable values of $v_i > 500$ m/s.

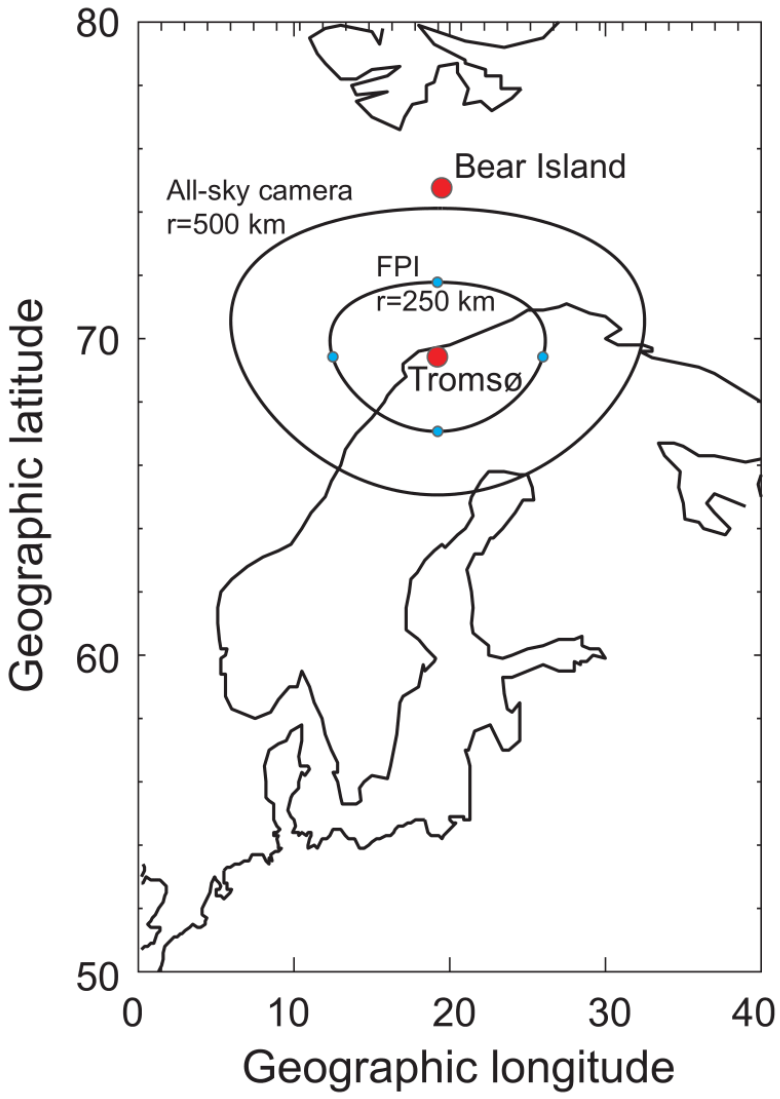

Figure 4.2 A map of Tromsø and Bear Island stations. Two large circles indicate a typical FOV of all-sky camera (radius: 500 km) and FPI scanning region (radius: 250 km) at Tromsø, respectively. Small blue circles indicate the FOV of FPI in four azimuthal directions.

The FPI-derived zonal (meridional) wind is calculated from the difference between the Doppler-shift speeds of the east (north) and west (south) directional winds. The positive direction in zonal and meridional wind points to the geographical east and north, respectively. The directional wind is the wind speed which is projected on the horizontal plane from the line-of-sight wind speed. Such calculation assumes a uniform horizontal wind field in the FOV of the FPI. This means that the zonal (meridional) wind is assumed to be same between the FPI scans in the east (north) and west (south) directions. In the initial selection of wind data, the intervals of the FPI

operation under the clear-sky conditions (status “s” and “p”) were used. The sky conditions every one hour were identified by a collocated all-sky airglow imager of Optical Mesosphere Thermosphere Imagers (OMTIs) [Shiokawa et al., 2009].

The auroral images were obtained by a collocated all-sky camera, which is provided by the National Institute of Polar Research (NIPR), Japan. This camera has a FOV of 180 °with a fish-eye lens. The magnetometer data were provided by the International Monitor for Auroral Geomagnetic Effects (IMAGE) magnetometer network. We used the magnetometer data obtained at the Tromsø and Bear Island stations. The two stations are located at the similar geographic longitude of ~19 °E. The Bear Island site is located at 74.50 °N and 19.20 °E in geographic coordinates. Figure 4.2 shows the locations of two stations. Two large circles indicate a typical FOV of all-sky camera (radius: 500 km) and FPI scanning region (radius: 250 km) at Tromsø, respectively. Small blue circles indicate the FOV of FPI in four azimuthal directions.

4.2 Substorm Onset Time

We used the X-component (positive toward the geographic north) of magnetometer data at Tromsø and Bear Island to identify the onset times of local substorms at Tromsø. By visual inspection, we identified one local substorm event as an obvious decrease (> 50 nT) from the quiet-time baseline in the X-component of the magnetic field data, which was followed by recovery on a timescale of > 1 h. We defined the timing of local substorm onset as the time when the X-component starts to decrease rapidly at the Tromsø and/or Bear Island stations. In such identification, we first used the data at Tromsø where the FPI wind measurement was made. Sometimes the amplitude of decrease in X-component was small and/or the onset timing was ambiguous, although we could identify an obvious decrease at Tromsø. In such a case, we checked the data at Bear Island instead. Besides, we also ensured that there was no other substorm events with magnitude > 50 nT within 1 h before the onset times we defined, and confirmed that the identified local substorm events are isolated cases. We only chose those events with wind measurements available both before and after the local substorm onsets. These criteria limited the number of events significantly. In total, we obtained four events of R1–R4, which were obtained at different LTs.

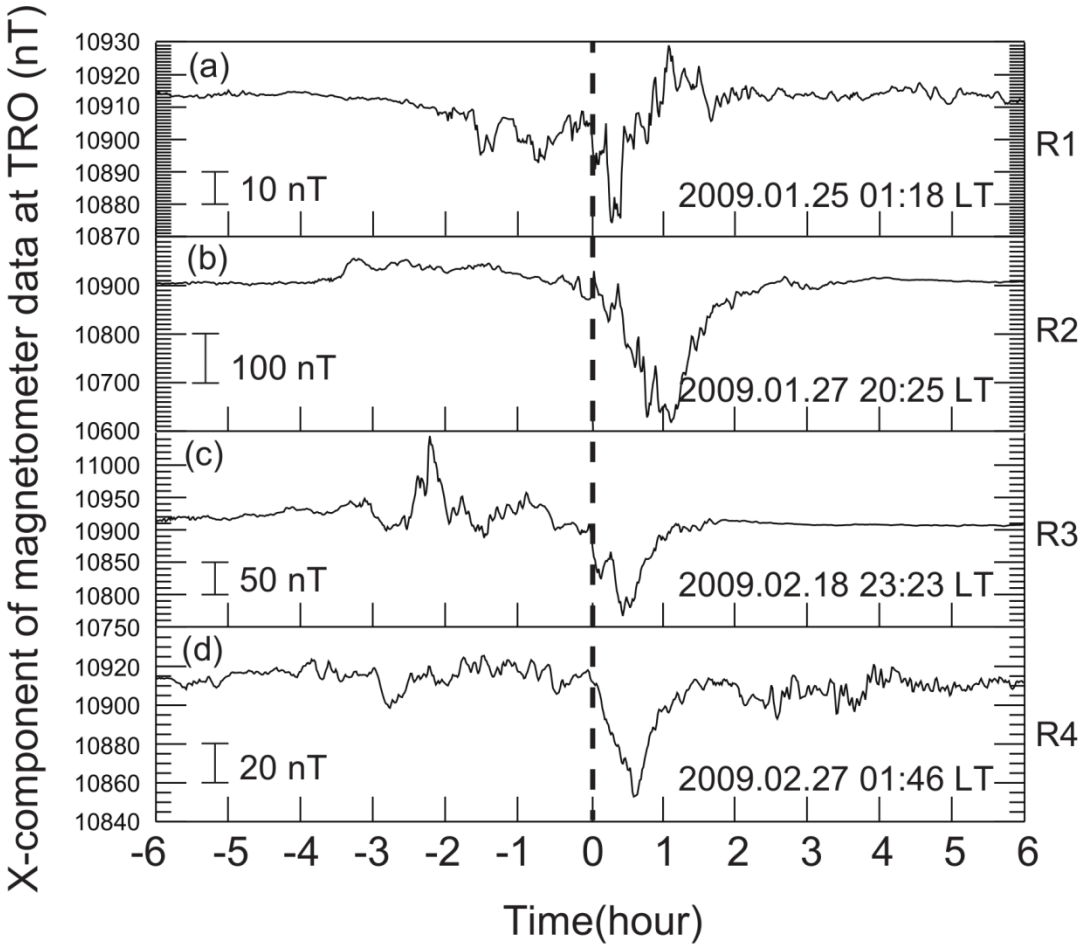

Figure 4.3 X-component of 12-h ground-based magnetometer data at Tromsø for four events. Panels a–d indicate the measurements for events R1–R4, respectively. In each panel, the central dashed line indicates the local substorm onset time near Tromsø. The event time (local substorm onset time near Tromsø) shown by the text is shown in LT at Tromsø (LT = UT + 1 h).

Figures 4.3 and 4.4 show the X-components of magnetic field variations for four events, which were obtained at the Tromsø and Bear Island, respectively. In each panel, the central dashed line represents the identified local substorm onset time near Tromsø. The onset times are written by the text at the bottom right. The local substorm onset signatures at Tromsø can be identified in Figures 4.3a, c, d, while those at Bear Island can be identified in Figure 4.4b. The slightly differing onset times at the two stations can be caused by the differences in the relative locations to the peak-current latitudes.

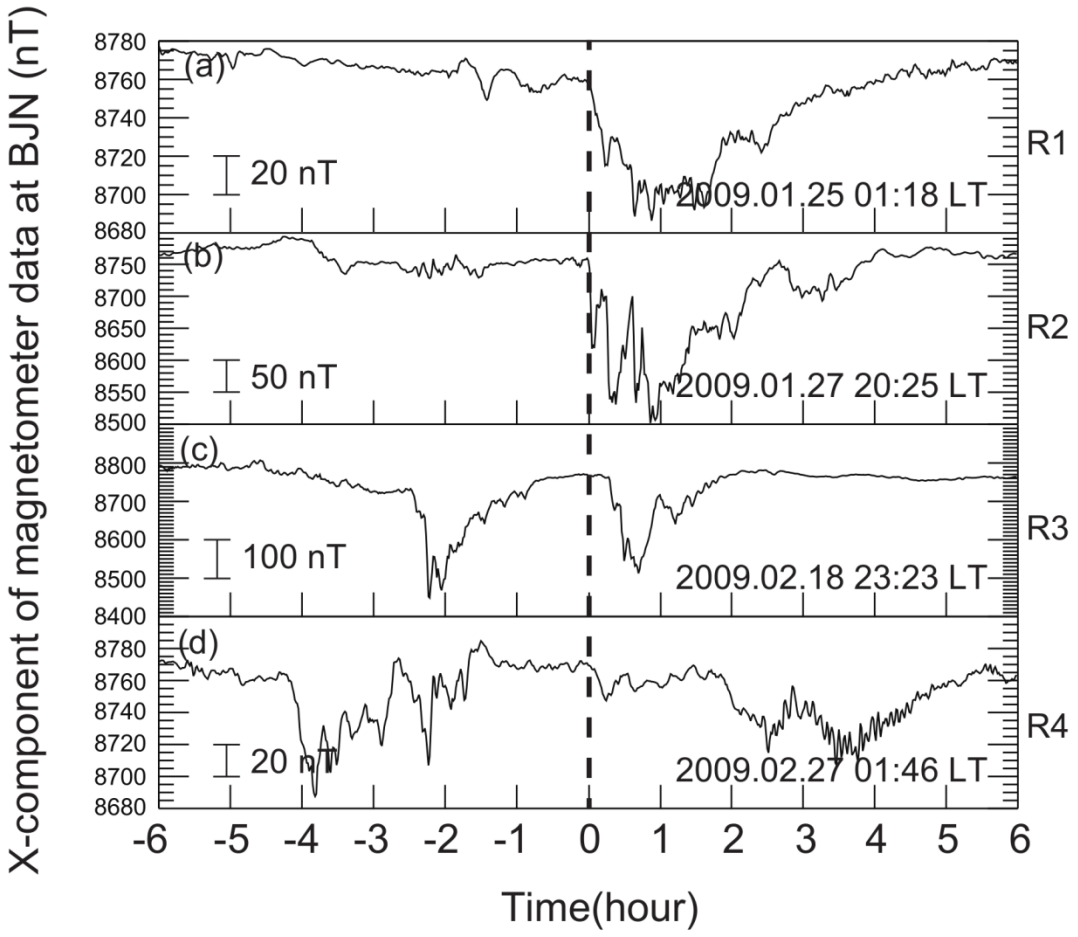

Figure 4.4 X-component of 12-h ground-based magnetometer data at Bear Island for four events, using the similar format in Figure 4.3. Panels a–d indicate the measurements for events R1–R4, respectively.

We also checked the latitude of the peak of westward electrojet current. We analyzed the Z-component magnetic field variation data in the latitudinally distributed stations in the IMAGE magnetometer network (not shown here). We found that the peak-current latitudes were located poleward of Tromsø and equatorward of Bear Island for all four events, which is consistent with the result obtained from the all-sky auroral images. The images show that Tromsø was located equatorward of the onset arcs for all events at the local substorm onset times. However, there is no magnetic field observatory between Tromsø and Bear Island stations. It is difficult to estimate the precise location of the peak-current latitudes.

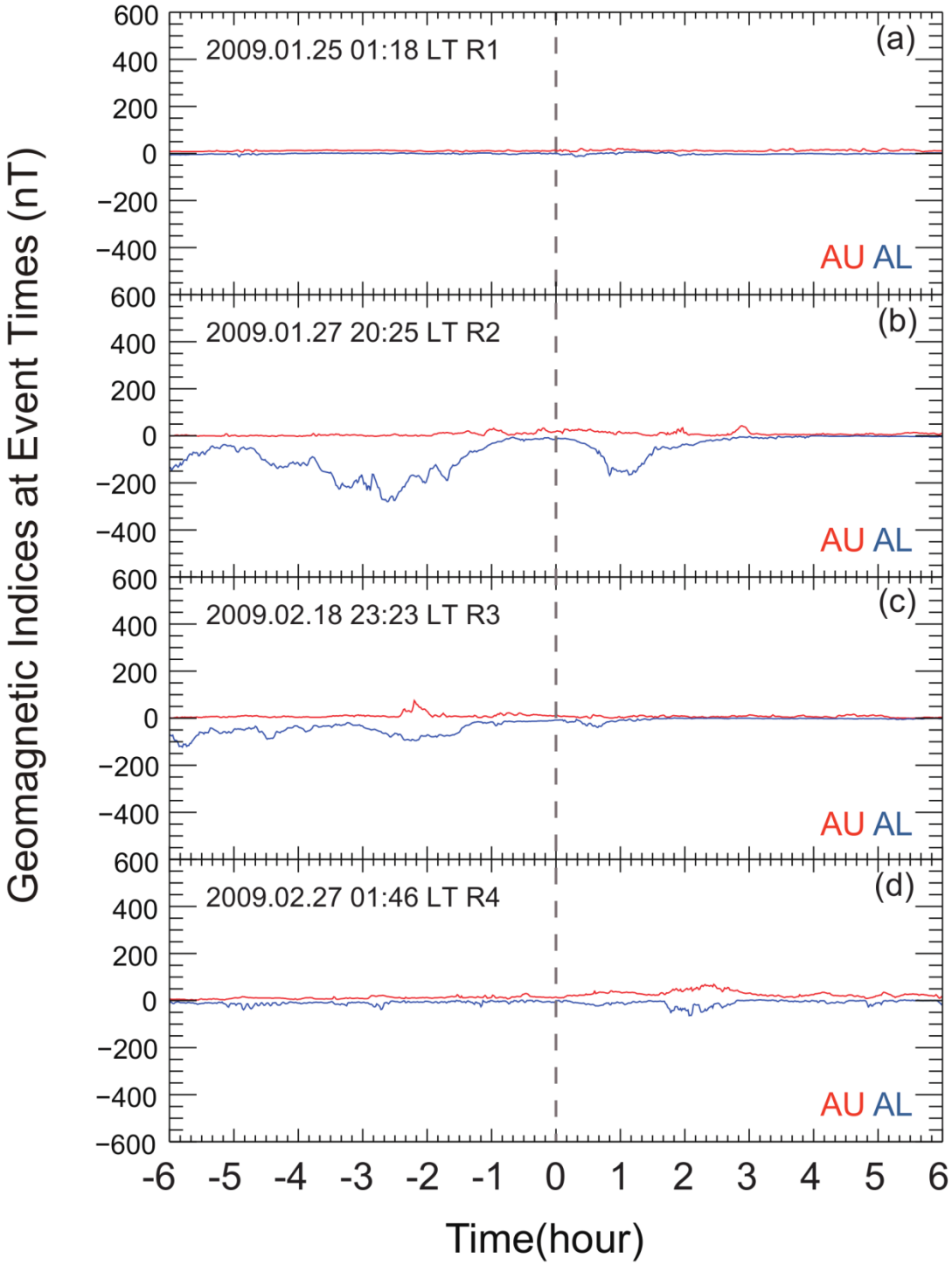

Figure 4.5 AU and AL indices for four events, using similar format in Figure 4.3.

Using the similar format in Figure 4.3, Figure 4.5 shows the amplitude upper (AU) and AL indices for all four events. Substorm activity on a global scale after the identified local substorm onsets can be seen in Figures 4.5b and d, whereas there were no obvious global enhancements of auroral electrojet currents in other events. We

consider that these four identified substorm events in this study could be small localized cases at the longitude of Tromsø and did not expand on a global scale. Besides, there were no substorm activities elsewhere at least 1 h before the identified local substorm onsets at Tromsø. The values of Ap index corresponding to the 12 h of four events shown in Figure 4.5 were between 0 and 27.

4.3 Wind Variations at Local Substorm Onsets

Figures 4.6 and 4.7 show the zonal and meridional winds of all four events plotted over the 4-h east-west cross sections (ewograms) and north-south cross sections (keograms) of the auroral images, respectively. In each panel, the cross sections are in RGB color. The vertical axis in cross sections, which is proportional to the zenith angle of the sky, represents the sequential pixel number in original auroral images. The ewograms and keograms can help to identify the movement of auroral activities in the zonal and meridional directions, respectively. There were no all-sky camera data for ~10 min around 02:16 LT on 27 Feb 2009 at Tromsø (event R4). The purple dashed lines show quiet-time winds at Tromsø, which were estimated from the Horizontal Wind Model 14 (HWM14) [Drob et al., 2015]. HWM14 winds at an altitude of 250 km are overlaid as each reference. The simultaneous Ap index was used as an input to the HWM14. We plotted the model values every 0.5 h. The local substorm onset time near Tromsø is shown by text. The error bars of wind measurements reflect the standard deviation σ_i introduced in Subsection 4.1. The two horizontal yellow lines indicate the east and west (north and south) points of the FPI sky scan at an elevation angle of 45˚ in the zonal (meridional) direction. The vertical red line indicates the local substorm onset time.

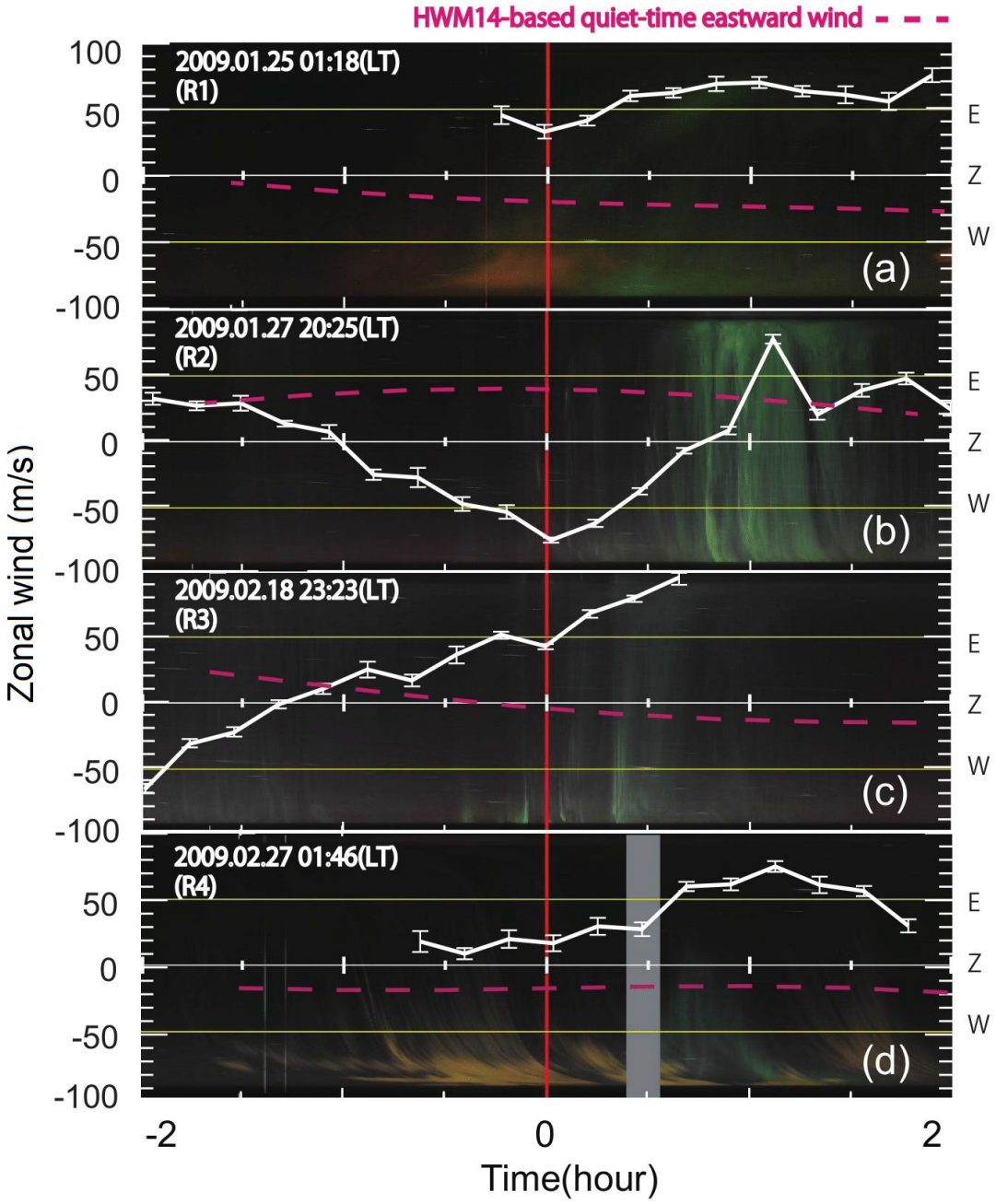

Figure 4.6 Zonal wind plotted over east-west cross sections of auroral images. Panels a–d indicate the measurements for events R1–R4, respectively. In each panel, the horizontal yellow lines indicate the east and west edges of the FPI scan with an elevation angle of 45 °. The vertical red line indicates the local substorm onset time, which is also shown by the text in the top left side. For all four events, Tromsø was located to the south of the onset arc at local substorm onsets. There were no all-sky camera data for ~10 min around 02:16 LT on 27 Feb 2009 at Tromsø (event R4).

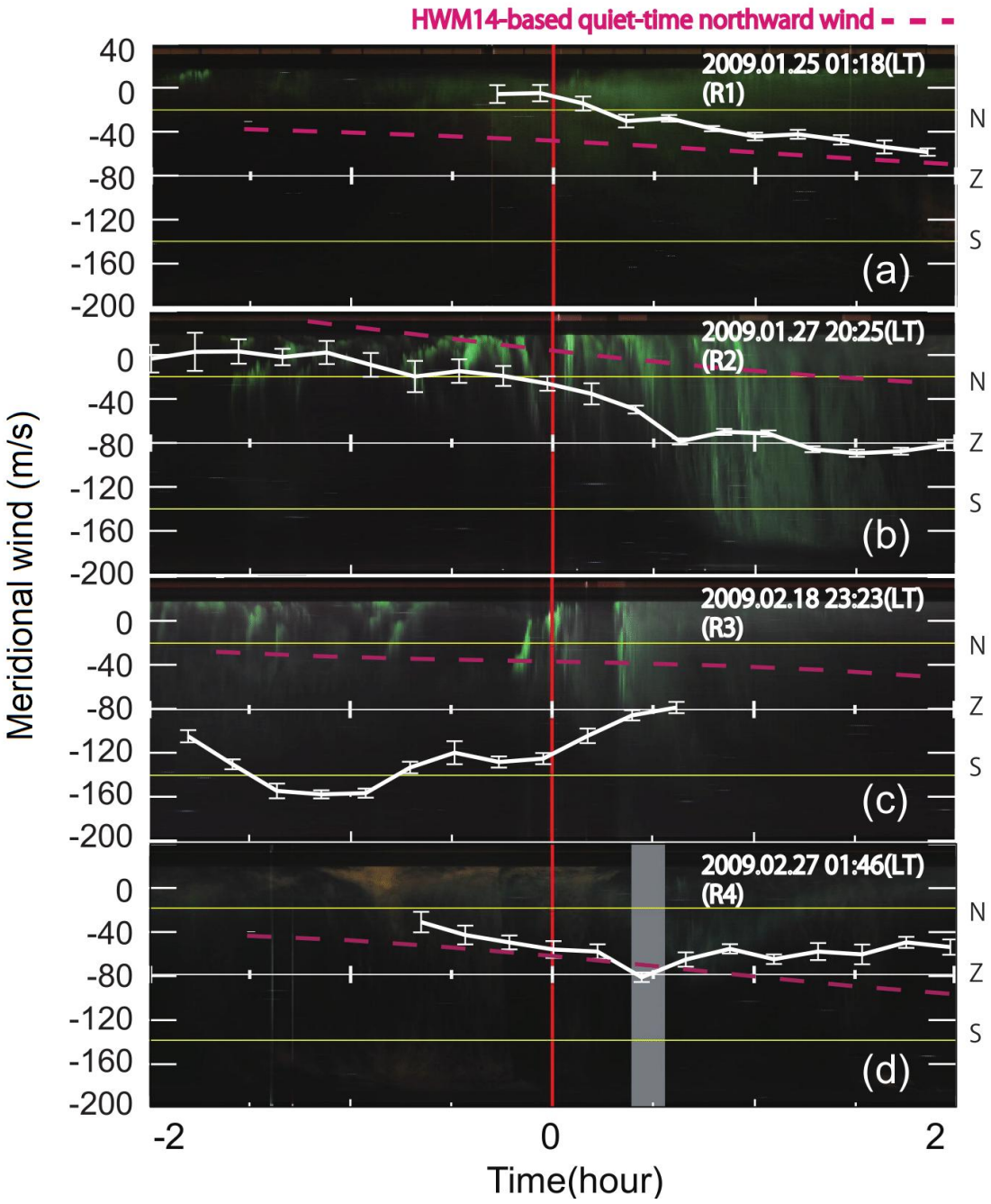

Figure 4.7 Meridional winds plotted over north-south cross sections of auroral images, using the similar format in Figure 4.6.

After the local substorm onsets, eastward increases of the zonal winds can be observed in all four events. The R1 and R2 events also had minimum values of the zonal winds at the onset times. Before the local substorm onsets, the wind of the R2 event was westward while that of the R1 event was still eastward. This may suggest that the zonal wind of the R2 event was accelerated westward before the onset time, although it is unclear for the R1 event due to insufficient amount of measurements.

After the local substorm onsets, the zonal winds of R1, R2 and R4 events increased eastward for ~1 h.

At the local substorm onsets, northward increase of the meridional wind can be seen in Figure 4.7c (R3), while decreases can be identified in Figures 4.7a (R1), b (R2) and d (R4). Before the local substorm onsets, the winds of all four events remained southward, although it is unclear for the R1 event due to insufficient amount of measurements. After the local substorm onsets, northward acceleration occurred in the R3 event for ~0.5 h. The meridional winds of R1 and R2 events decreased for > 1 h, while the R4 event showed decrease for ~0.5 h.

We have to note that obvious changes in the trend of wind measurements at local substorm onsets were observed in the zonal winds of R1 and R2 events, and meridional wind of R3 event. The estimated variations due to the tidal wind (see later Figure 4.9) at these onset times should be a decrease of magnitude pointing to the east for these two zonal winds and an increase of magnitude pointing to the south for this meridional wind. Therefore, it seems that these abrupt changes cannot be caused by the tidal wind. The local substorm onsets probably play a more important role for these cases. Detailed discussion will be given in the Subsection 4.5.

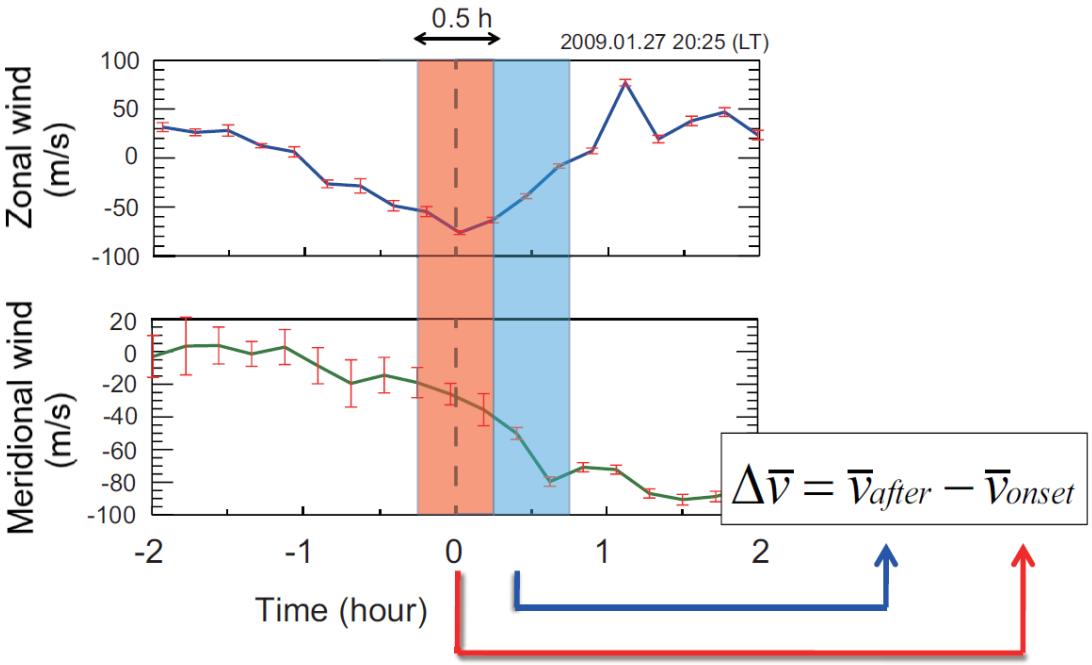

Figure 4.8 Schematic view of calculating the wind variations at local substorm onsets.

In order to quantitatively evaluate the wind variations at substorm onsets, we calculated the differences in average wind speeds at ±15 min to the onset time and at ±15 min to 30 min after the onset time. The standard deviation σ_i indicates the statistical error in each wind measurement. Therefore, we calculated the weighted average of wind speed $\bar{v}_{onset}$ around the local substorm onsets by

$$\bar{v}_{onset} = \frac{\sum_{i=1}^{n}(v_i/\sigma_i^2)}{\sum_{i=1}^{n}(1/\sigma_i^2)} \quad (4.1)$$

where *n* is the number of data points during the 30 min. We also calculated the weighted average of wind speed $\bar{v}_{after}$ at 30 min after the local substorm onsets using the same method. Then the difference $\Delta\bar{v}$ between $\bar{v}_{onset}$ and $\bar{v}_{after}$ can be written as

$$\Delta\bar{v} = \bar{v}_{after} - \bar{v}_{onset}\,. \quad (4.2)$$

Figure 4.8 is a schematic view of calculating the wind variations at local substorm onsets. This difference $\Delta\bar{v}$ indicates the wind variation before and after local substorm onsets. For the zonal (meridional) wind, $\Delta\bar{v} > 0$ indicates an increase, which means that the wind blows more to the east (north). On the other hand, $\Delta\bar{v} < 0$ indicates a decrease, which means that the wind blows more to the west (south).

Table 4.1 Observation results and discussions of four events.

Event (component)	Local time	Wind variation (m/s)	Diurnal tide	Plasma convection	Arc-associated electric field	Directional winds	Joule heating
R1 (Z)	01:18	+17.5	N	Y	U	Y	Y
R1 (M)	01:18	-18.4	Y	N	U	N	Y
R2 (Z)	20:25	+48.9	Y	N	N	U	Y
R2 (M)	20:25	-41.8	Y	Y	U	U	Y
R3 (Z)	23:23	+32.3	N	Y	N	Y	Y
R3 (M)	23:23	+35.5	N	N	U	Y	Y
R4 (Z)	01:46	+24.5	Y	Y	U	Y	Y
R4 (M)	01:46	-23.0	Y	N	U	Y	Y

Y - Wind variation is consistent with that effect (for directional winds: two winds are consistent; for Joule heating: auroral activities penetrated into the FPI scanning region)

N - Wind variation is inconsistent with that effect (for directional winds: two winds are inconsistent)

U - Uncertain or not discussed

Z - Zonal wind

M - Meridional wind

The values of wind variations $\Delta\bar{v}$ calculated using Equations 4.1 and 4.2 are summarized in Table 4.1. The absolute values of observed wind variations at local substorm onsets were less than 49 m/s and more than 17 m/s. The standard deviations (error bars) of the wind measurements used to calculate the weighted averages are 1.9–9.7 m/s (average: 4.8 m/s). Therefore, the observed wind variations are significant compared with the standard deviations. The values of prehistory Kp index at 3–6 h before the local substorm onsets were 0^{+}, 2^{-}, 1 and 1 for R1–R4 events, respectively. It seems that there was no strong prehistory plasma convection that can contribute to the observed wind variations at local substorm onsets.

Figure 4.9 shows a polar plot of the wind variations $\Delta\bar{v}$ at local substorm onsets for all four events. Zonal and meridional winds are indicated by the blue and green arrows, respectively. The length of each arrow corresponds to the absolute value of $\Delta\bar{v}$. Note that these arrows indicate the wind change before and after the local substorm onsets. We can observe eastward increases of the zonal winds from the pre-midnight to post-midnight sector and southward increases of the meridional winds except for the midnight sector.

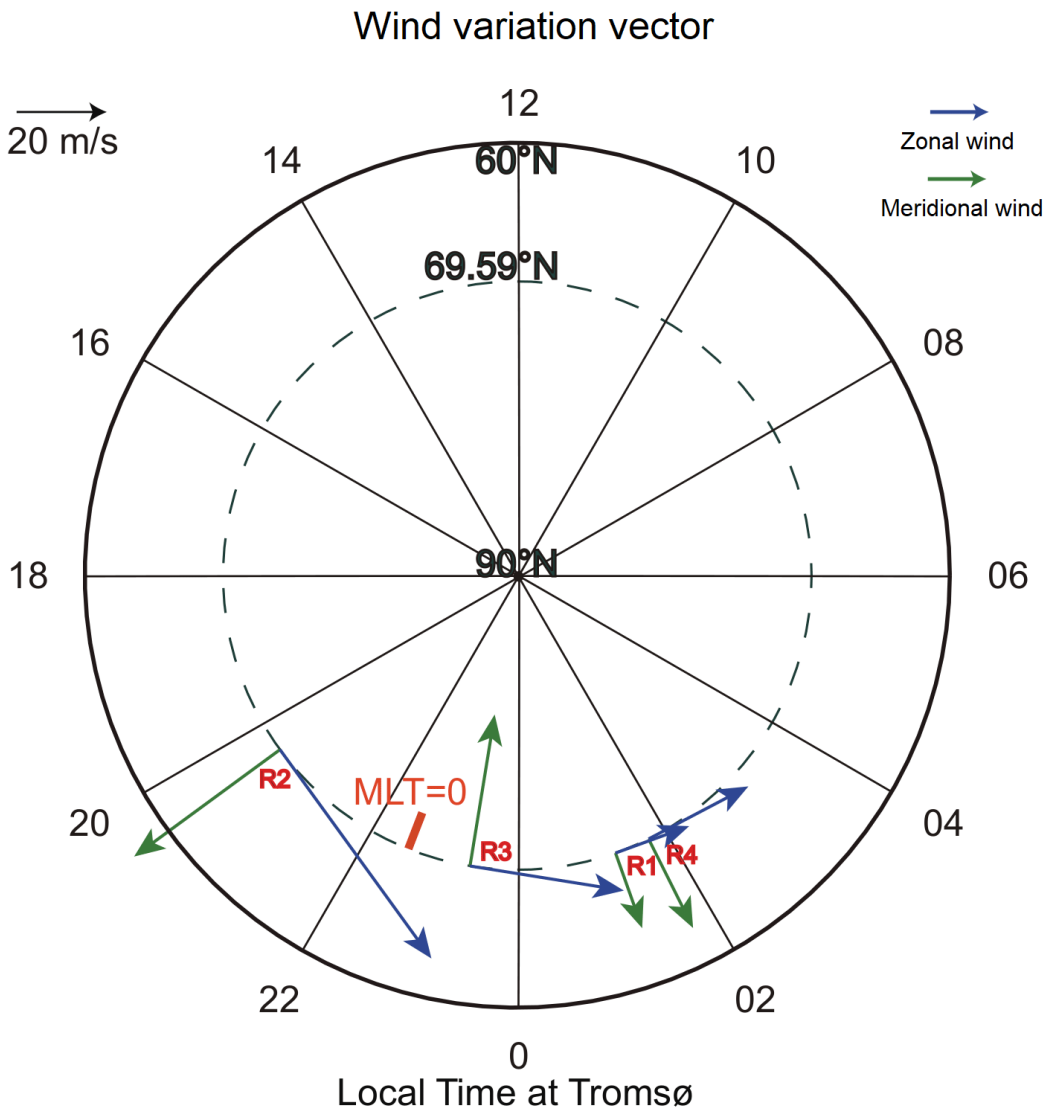

Figure 4.9 Polar plot of wind variations at local substorm onsets for all four events. Zonal and meridional wins are indicated by the blue and green arrows, respectively. The largest observed wind variation was 48.9 m/s (zonal wind of R2 event).

4.4 Discussion on Relevance to Substorm Development

In the Subsection 4.3, we have shown that the variations of thermospheric winds at local substorm onsets were less than 49 m/s for the observed four events. Using CHAMP data at an altitude of ~400 km, Ritter et al. [2010] found that an eastward wind disturbance of the order of 20 m/s in the pre-midnight and midnight sectors and a westward wind disturbance of the order of 50 m/s in the post-midnight sector occur associated with substorms. Wind variations of < 50 m/s at the F-region height at local substorm onsets seem to be a common phenomenon.

As we mentioned in Subsection 1.3, the high-latitude neutral wind can contribute

to a notable Hall current system for several hours, which is called the "flywheel" effect [Lyons et al., 1985; Deng et al., 1991]. At E and F regions, the electrons are hardly moved by neutral motion because of large ratio of cyclotron frequency to electron-neutral collision frequency. The neutral wind can move ions mainly in the directions of u_n (E region, Hall current) and $u_n \times B$ (F region, Pederson current), where u_n is horizontal neutral wind velocity, and B is the geomagnetic field [Rishbeth, 1997]. Thus the wind-induced ionospheric current is mainly due to ion motion changes. At local substorm onsets, the wind-induced ionospheric current can be connected to the field-aligned current (FAC), and cause an inhomogeneity of magnetic tension force. This inhomogeneity may propagate along the magnetic field line and finally affect the plasma dynamics in the near-Earth magnetosphere during the substorm expansion phase. Here, the wind variations play as a feedback to the energy inputs from the magnetosphere.

From the simplified transport equation of Schunk and Nagy [2009], we can obtain the expression of ion velocity u_i which is perpendicular to B as:

$$u_i = \left(\frac{\nu_i \omega_{ci}}{\nu_i^2+\omega_{ci}^2}\frac{u_n \times B}{|B|} + \frac{\nu_i^2}{\nu_i^2+\omega_{ci}^2}u_n\right) + \left(\frac{\nu_i \omega_{ci}}{\nu_i^2+\omega_{ci}^2}\frac{E}{|B|} + \frac{\omega_{ci}^2}{\nu_i^2+\omega_{ci}^2}\frac{E \times B}{|B|^2}\right), \quad (4.3)$$

where ν_i is the ion-neutral collision frequency, ω_{ci} is the ion gyrofrequency, E is the electric field. It is in a stationary frame of reference. In this equation, the left and right brackets in the right side represent the ion velocities caused by neutral wind and electric field, respectively. This equation can indicate the ion current if we multiply it by $n_i e_i$, where n_i and e_i are the density and electric charge of individual ion, respectively.

As an ionospheric current generator, $u_n \times B$ acts as a similar function with E [Rishbeth, 1997; Schunk and Nagy, 2009]. The ionospheric plasma convection is generally caused by the $E \times B$ drift. The drift velocity v_{drift} can be expressed as $E \times B/|B|^2$. Thus E can be written as $-v_{drift} \times B$. Mathematically, both $u_n \times B$ and $-v_{drift} \times B$ (E) can be seen as a current generator. Therefore, the comparison between u_n (or wind variations calculated in this study) and v_{drift} can reflect their relative contributions to the ionospheric current. In this study, the observed wind variations (< 49 m/s in the F region) are much smaller than the typical plasma convection speed (hundreds of meters per second) in the auroral zone [e.g., Provan et al., 2004; Bristow and Jensen, 2007]. This result may suggest that the wind-induced ionospheric current at local substorm onsets does not provide strong feedback to the development of substorm expansion phase in the magnetotail.

4.5 Discussion of Wind Variations at Local Substorm Onsets

In this subsection, we discuss the possible causes of observed wind variations shown in Figures 4.6, 4.7 and 4.9 by considering diurnal tides, plasma convection, and arc-associated electric field. We also discuss the possible spatial inhomogeneity in the FPI sky scan due to auroral Joule heating. These discussions are based on the observed directions of wind variations at local substorm onsets. The results are summarized in Table 4.1. However, we have to note that the tidal wind can cause wind changes with a timescale of several hours, while other factors associated with substorm are more related to wind variations with a shorter timescale. Such short timescale can be comparable with the focused 1 h in this study.

4.5.1 Diurnal Tide

The two important factors that affect high-latitude thermosphere are tides and plasma convection. As shown in Figure 4.10, the day-to-night pressure gradient causes the general structure of tides. Derived from the theory-based model of Kohl and King [1967], Figure 4.11 shows a schematic view of both zonal and meridional winds caused by the diurnal tide at an altitude of 300 km in the nightside high latitudes. The LT when the zonal wind changes direction and the time of minimum meridional wind can shift 2–3 h (we assumed 2 h in Figure 4.11) from the midnight to the post-midnight LTs. Based on this result, we mainly checked the direction of diurnal tide variation at the timing of local substorm onsets, and compared its consistency with the observed wind variations.

The consistency between the directions of diurnal tide variation and observed wind variations can be seen in the R1 (meridional wind only), R2, and R4 events as indicated by “Y” in Table 4.1. The zonal wind of the R2 event showed a continuous westward increase before the local substorm onsets, which is consistent with the tendency of diurnal tide variation. At ~1 h after the onset times, the zonal winds of the R2 and R4 events started to increase westward, which can also be explained by the diurnal tide variation.

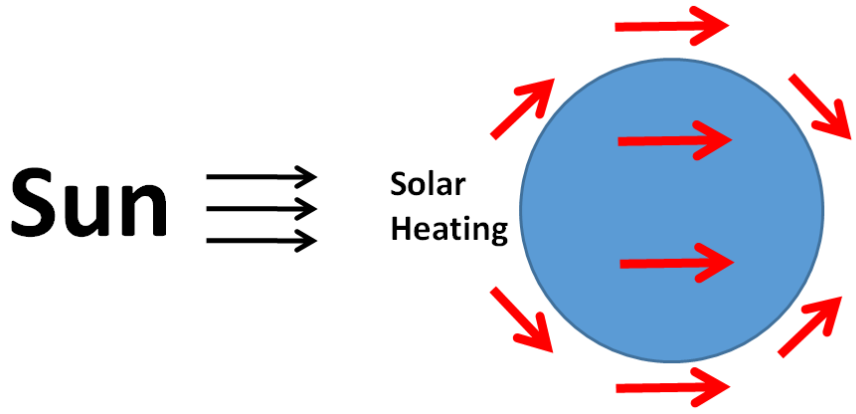

Figure 4.10 A schematic view indicates that the tides are driven by solar heating. The thermospheric wind generally flows from dayside to nightside on Earth.

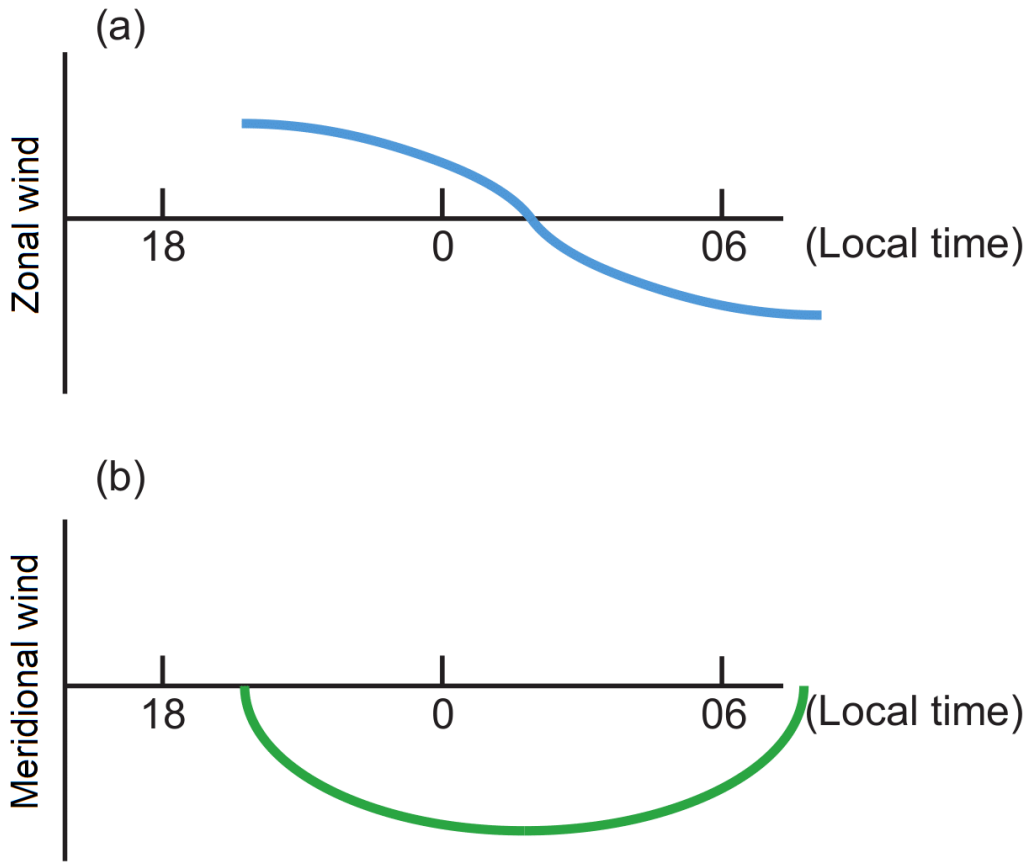

Figure 4.11 A schematic view of diurnal tide based on the model of Kohl and King [1967].

For the meridional wind, the R1 and R2 events showed continuous decreases during the whole measurement, which is consistent with the variation tendency before the meridional-wind minimum in the diurnal tide variation. The R4 event had a

U-shape variation with a minimum at ~30 min after the onset time, which is quite similar to the tendency of diurnal-tide variation around the meridional-wind minimum. As a result, five of the eight observed wind variations at local substorm onsets are qualitatively consistent with the diurnal tide variation. We should mention that the diurnal tide effects can be seen as a result of the Earth's rotation.

4.5.2 Plasma Convection

We estimated the direction of plasma convection at local substorm onsets using the high-latitude plasma convection model of Weimer [1995]. This plasma convection model is based on the electric field measurements obtained from the DE-2 satellite, which has a polar orbit with altitudes of 300–1000 km. In this study, Tromsø was located at the lower latitude side of the model convection pattern (see Figures 2–8 in Weimer [1995]). Basically, the plasma convection is expected to be westward and eastward in the pre-midnight and post-midnight sectors, respectively. We also assumed that the convection speed increased after local substorm onsets. As summarized in Table 4.1, half of the cases show consistency between the observed wind variations and the model plasma convection at local substorm onsets. Note that three of the four zonal winds have such consistency.

However, we should mention that it may take time in the momentum transfer from plasma to neutral particles when considering the ion drag effect in the high-latitude thermospheric F region. The time constant of this ion drag process can be 0.5–6.5 h [Baron and Wand, 1983; Kosch et al., 2001]. In this study, the 30-min timescale we used to calculate the wind variations is shorter than this typical time constant. Therefore, the wind variations due to plasma convection may not have reached a steady state in the observed results.

We also checked the actual plasma convection data obtained by the Super Dual Auroral Radar Network (SuperDARN) and EISCAT radars, as well as the global plasma convection pattern from the SuperDARN radar and the data assimilation model [Ruohoniemi and Baker, 1998], but did not find any useful information. There were no sufficient echoes in the Pykkvibaer and Hankasalmi SuperDARN radars for any of the event times. For the EISCAT radar, we found only a weak signal before the local substorm onset at ~01:18 LT on January 25, 2009, for event R1. However, we cannot further discuss this result because it only provided information before the onset time. In addition, EISCAT was not operational at other event times.

4.5.3 Arc-associated Electric Field

Regarding the ion drag effect on neutral particles, besides the background ionospheric plasma convection, there is also an additional factor about the auroral arc-associated ionospheric electric field. In the formation of the FAC during substorms, an intense perpendicular ionospheric electric field pointing to the auroral arc is generated locally on the equatorward (poleward) side of the auroral arc in the dusk (dawn) sector as a response to the increased upward current [e.g., Aikio et al., 1993; Burke et al., 1982; Carlson et al., 1988; Doe et al., 1995; Valladares and Carlson, 1991]. Figure 4.12 shows a schematic view of the location of arc-associated electric field in the Northern Hemisphere.

At the local substorm onset times, Tromsø was located at the equatorward side of the onset arcs for all four events. Thus, we only considered those events located at the dusk side when discussing the arc-associated electric field. The R2 and R3 events were located in the dusk (pre-midnight) sector according to their LTs. Because the geomagnetic field is downward in the Northern Hemisphere, the direction of ion drag caused by the $E \times B$ drift from this arc-associated electric field points to the west in the dusk sector. The observed eastward increases in the zonal winds of R2 and R3 events are inconsistent with this westward drive due to the arc-associated electric field, as shown by “N” in Table 4.1. These results may suggest that the arc-associated electric field does not work for the observed four events.

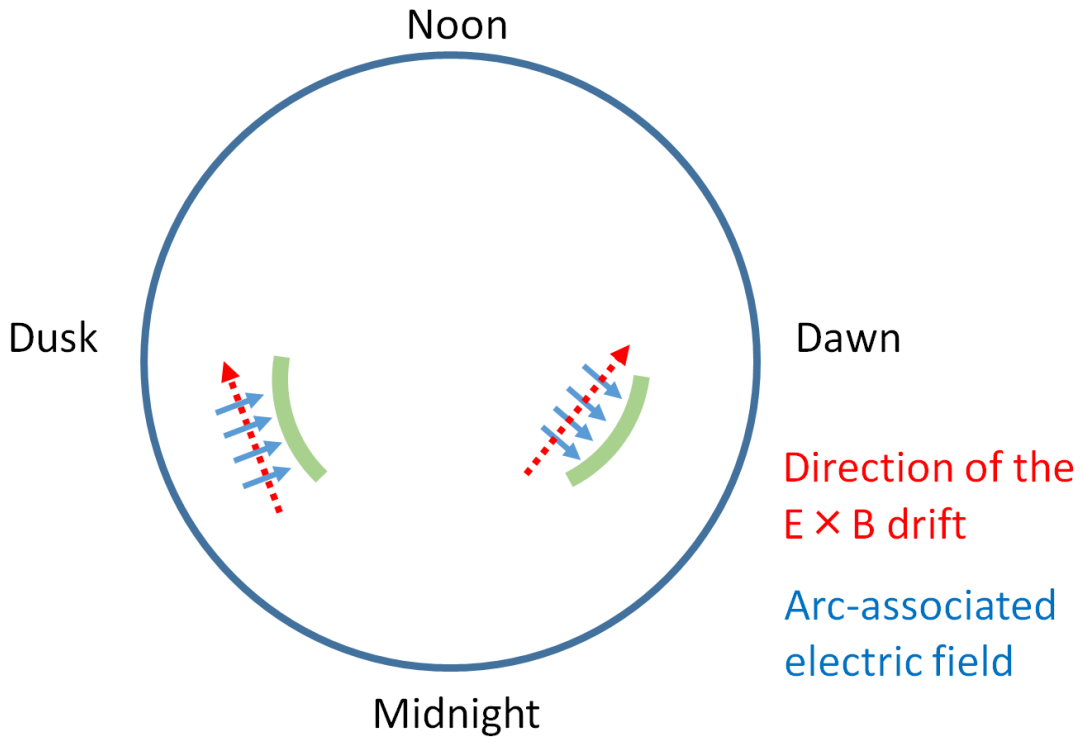

Figure 4.12 A schematic view of the location of arc-associated electric field in the Northern Hemisphere. The blue arrows indicate the arc-associated electric field, while the red arrow shows ion drag effect on thermosphere. The green belt indicates the auroral arc.

Besides, this arc-associated electric field can cause the frictional heating at F-region height through ion-neutral collision [Opgenoorth et al., 1990; St.-Maurice and Hanson, 1982]. This would expand the neutral atmosphere and may cause subsequent southward wind at Tromsø, because Tromsø is always at equatorward side of the auroral arcs. This expansion effect belongs to the discussion in Subsection 4.5.4.

4.5.4 Spatial Homogeneity and Directional Winds

In the FPI measurement, we checked the directional winds to investigate the spatial homogeneity of the wind field in the FOV of the FPI sky scan. We compared the 4-h directional winds in the four directions of east, west, north and south. For a pair of east-west or north-south directional winds, we defined them as “consistent” if anti-phase variations (similar amplitudes but with opposite signs) are visually

identified. This term “consistent” indicates homogeneity of the wind field in the FPI sky-scan area. As shown in Table 4.1, “Y” and “N” indicate that the two directional winds are consistent and inconsistent, respectively. We only see an inconsistency between north and south directional winds in the R1 event.

We assumed that Joule heating is strong enough to change the background wind field existing near the auroral arc. Once the auroral activity penetrates into the FPI scanning region in the zonal (meridional) direction, the Joule heating will cause expansion of the neutral air and affect the east (north) and west (south) directional winds in opposite directions. In such a case, inconsistent directional winds are expected to be observed.

From Figures 4.6 and 4.7, we can see the penetration of auroral activities in all four events. The last column in Table 4.1 corresponds to the Joule heating of auroral activities, where “Y” indicates that auroral activity have penetrated into the FPI scanning region in the zonal (meridional) direction for the zonal (meridional) wind. Based on these results and assumption, we suggest that the Joule heating effect of auroral activities only influenced meridional wind of the R1 event and caused the corresponding inconsistency in directional winds.

It should be noted that auroral activities inside the FPI scanning region may not always affect the FPI wind measurement, because the center location of the Joule heating can be different from the optical aurora region. Besides, the Joule heating rate per mass of the neutral peaks at F-region height, although the Joule heating rate has a peak at E-region height [Deng et al., 2011]. The modification to the pressure gradient due to the Joule heating process should be more obvious in the F-region thermosphere.

4.5.5 Summary and Discussion

Based on the directions of observed wind variations at local substorm onsets, we found that the variations in three of the four zonal and one of the four merdional winds are consistent with the wind change expected from plasma convection enhancement associated with substorms, and the variations in two of the four zonal and three of the four merdional winds are consistent with the winds expected from diurnal tide. None of these wind variations can be explained by the ion drag effect based on the arc-associated electric field. We suggest that the inconsistency between

directional winds in one meridional wind is caused by the Joule heating effect of the moving auroral activity, if we assume that strong Joule heating can exist near the auroral arc. These results suggest that for our observed F-region wind variations at local substorm onsets, they were caused mainly by plasma convection and diurnal tide, while arc-associated electric field did not contribute much.

Cai et al. [2019] used the same FPI (630.0 nm) at Tromsø in a study of thermospheric wind variations during different substorm phases. The four substorm events found in their report are different with this study and have stronger X-component magnetic field variations. We found that the plasma convection is one important factor to affect the observed wind variations at local substorm onsets, which is consistent with their results. If we assume that the observed wind variations occurred within 30 min, then the amplitudes of acceleration rates of zonal winds were 0.0097–0.0272 m/s^2 (+17.5 m/s of R1, +48.9 m/s of R2). These acceleration rates of zonal winds are comparable with the ones (0.0189–0.1 m/s^2) during/near the expansion phase reported by Cai et al. [2019].

In the end, we have to note that various discussed factors may affect the wind variations simultaneously for the observed four events. A possible solution to separate individual factors might be using a 3D circulation model driven by the observations of various parameters, such as electric field and ion density. Liuzzo et al. [2015] tested the reliability of the Global Ionosphere-Thermosphere Model (GITM) in simulating the mesoscale wind during a substorm event at high latitudes. They concluded that model wind at high latitudes can be reliable only if an accurate representation of the actual drivers prevailing at the time can be identified. In order to apply the model unambiguously and reproduce the high-latitude thermospheric response to local substorm onsets, we need to obtain more observation parameters.

4.6 Conclusions

This was the first time that the high-latitude thermospheric wind variations at local substorm onsets are investigated using an FPI at Tromsø in Norway. We used wind data in 2009 which were measured from the Doppler shift of red-line emission (630.0 nm, F region). In total, we obtained four events, which occrred at different LTs. We discussed possible causes of the wind variations by considering diurnal tide, plasma convection and arc-associated electric field. We also considered spatial homogeneity in the FPI sky scan. The results in this chapter can be summarized as

follows.

1. We assumed that the abrupt substorm energy input can create a sudden change of the thermospheric wind that may be distinguishable from the background slower effects, although the timescale of ion drag effect can be several hours. We observed some sudden changes of the wind direction at local substorm onsets.

2. The observed wind variations at local substorm onsets were less than 49 m/s. These values are much smaller than the typical plasma convection speed in the auroral zone. We speculate that the wind-induced ionospheric current at local substorm onsets does not provide strong feedback to the development of substorm expansion phase in the magnetotail.

3. The observed events showed eastward increases of zonal winds from the pre-midnight to post-midnight sector and southward increases of meridonal winds except for the midnight. We suggest that the observed wind variations at local substorm onsets were affected mainly by plasma convection and diurnal tide, while arc-associated electric field did not contribute much.

Finally, we have to note that the conclusions in this chapter are based on a limited number of events. The response of high-latitude thermosphere and the role of various factors may be different for different substorm cases. More measurements about thermospheric winds should be studied in order to understand the complicated thermospheric responses at substorm onsets.

Chapter 5
Average Thermospheric Winds at High Latitudes during Geomagnetically Quiet Times

This chapter presents the first study of quiet-time average thermospheric winds using an FPI at Tromsø, Norway. This is an expanded study of the results shown in Chapter 4. We defined geomagnetically quiet conditions both locally and globally, and obtained the quiet-time average winds. We then subtracted the influence of quiet-time average winds from the resutls of previous event study, and confirmed that the main conclusions in Chapter 4 are preserved. This indicates that the observed high-latitude thermospheric wind variations at local substorm onsets are mainly caused by substorm-associated phenomena with short time period, such as the intensification of ionospheric plasma convection. Most contents described in this chapter have been published by Xu et al. [2019b].

5.1 Definition of Quiet-time Measurement

In order to obatin the quiet-time average winds at Tromsø, we checked the wind data collected during 2009–2015 from the red-line emission (wavelength: 630.0 nm) of FPI measurments. The emission altitude of the 630 nm airglow is 200–300 km in the thermosphere, and therefore the FPI-derived winds are weighted values through the 630 nm emission profile. The details about this FPI and other instruments can be found in Subsection 4.1.

We applied strict criteria to define geomagnetically quiet times at Tromsø. For step 1, we used Kp $\leqslant$ 1^{+} to ensure globally quiet conditions both at the time of the wind measurement and 3–6 h before the wind measurement because neutral gas can take that long to recover after being influenced by geomagnetic activity at high latitudes [Aruliah et al., 1999].

For step 2, we ensured locally quiet conditions at Tromsø. We defined baseline X-component values at Tromsø at each time sector for each year, as shown in Table 5.1. Each baseline value was chosen from the first clear quiet day of that year as determined by visual inspection, presented as 1-h averages. If no value was available

for a given year, we used the corresponding value from the previous year. We defined a non-quiet interval when the absolute difference between the X-component value and the baseline exceeded 50 nT. An isolated substorm event was defined as a continuous series of non-quiet intervals that lasted for more than 1 h, and the first (last) non-quiet interval was defined as the start (end) of the isolated substorm event. As shown in Figure 5.1, we excluded any wind measurements obtained either during or up to 3 h after these isolated substorm events.

Table 5.1 The baseline X-component values at Tromsø at each time sector for each year.

Year	Dusk (14–20 UT)	Midnight (20–2 UT)	Dawn (2–8 UT)	Date of the chosen value
2009	10910.4	10901.2	10886.4	26 Jan, 2009
2010	10903.2	10902.6	10903.0	8 Feb, 2010
2011	10893.9	10888.7	10890.9	27 Jan, 2011
2012	10893.9*	10888.7*	10890.9*	--
2013	10847.3	10846.4	10850.1	4 Oct, 2013
2014	10852.4	10849.9	10850.1*	13 Feb, 2014
2015	10852.4*	10849.9*	10850.1*	--

Unit: nT

* We used the same corresponding value in previous year.

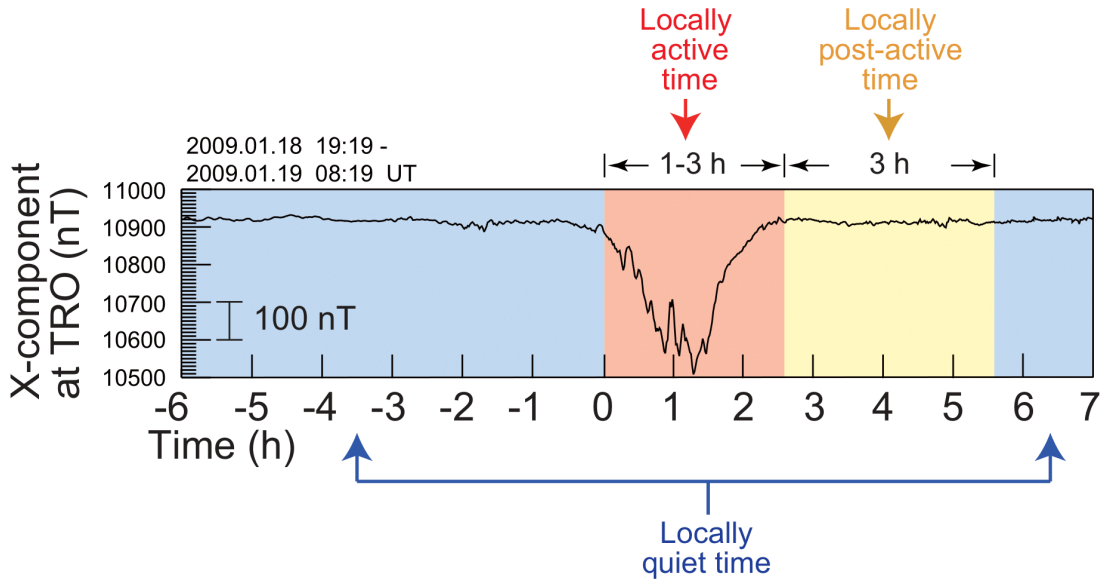

Figure 5.1 Definition of locally quiet at Tromsø.

For step 3, we checked the all-sky images at Tromsø and excluded any measurements made when auroral activities were penetrating the FPI scanning region. In this study, quiet-time periods were defined as those that satisfied the criteria in above steps 1–3. We further excluded some wind measurements with suspicious cloud influences as identified by the all-sky auroral camera, although the weather conditions were already checked at the beginning of wind data selection. The left data were qualifying wind measurements.

Finally, for step 4, we used these qualifying wind measurements to calculate the 30-min initial average winds (the thick gray curves in Figures 5.2b and 5.3b). Despite being selected as wind measurements during geomagnetically quiet times, some exceptional wind measurements exhibited large deviations from the initial average winds, as marked by the red asterisks in Figures 5.2b and 5.3b. The deviations were more than 100 m/s from the initial average winds, which may have been caused by geomagnetic activities not identified in above steps 1–3. We therefore removed these exceptional wind measurements with large deviations from the initial average winds in the qualifying wind measurements. The remaining data were used to re-calculate the final quiet-time average winds as shown by the blue and green curves in Figures 5.2a and 5.3a, respectively. The same blue and green curves are present in Figures 5.2b and 5.3b, respectively, but they mostly overlap with the initial average winds shown as the gray curves. We will discuss the possible causes of the aforementioned exceptional wind measurements in the Subsection 5.4.

The selected wind measurements that satisfied the above steps 1–4 were only in the winter at Tromsø. The Table 5.2 shows the dates of all these wind measurments. For most dates, both zonal and meridional wind measurements were available.

Table 5.2 The selected wind measuremnts during geomagnetically quiet time.

Year	Month and Dates with measurements
2009	1.23–1.25, 1.28, 1.29, 2.17, 2.18, 11.10, 11.11, 11.13, 11.14, 11.17–11.20, 11.24, 11.27, 12.6–12.8, 12.25
2010	2.18, 3.2
2011	2.23, 2.24, 11.19
2012	9.28, 11.23, 12.23
2013	--
2014	1.19, 11.13
2015	--

5.2 Quiet-time Average Winds

Figures 5.2 and 5.3 show the quiet-time average winds at Tromsø in the zonal and meridional directions, respectively. The half-length of an error bar corresponds to the standard deviation of all the wind measurments used to calculate the average in that bin. As shown in Figures 5.2b and 5.3b, there were 5–20 wind measurements in each 30-min bin to calculate the average winds. In Figures 5.2a and 5.3a, we also plotted in yellow the quiet-time average winds at Kiruna in Sweden (67.87°N, 20.43°E in geographic coordinates) from Aruliah et al. [1999] and in red the average winds at Tromsø as obtained from the HWM [Drob et al., 2015].

Considering the diurnal tide, the zonal wind in Figure 5.2a should be eastward before 2–3 UT and westward after 2–3 UT [e.g., Kohl and King, 1967]. However, the observed zonal wind exhibits a westward increase before the midnight, with a minimum of ~0 m/s at 21–22 UT. After 22 UT, the zonal wind recovers eastward and then decreases again after midnight. The zero crossing of the zonal wind after midnight occurs at ~3 UT. The maximum speed of zonal wind is ~100 m/s at both the dusk and dawn sides. On the other hand, the meridional wind in Figure 5.3a shows an equatorward wind with a minimum value of -130 m/s around the midnight, which is a typical signature of a diurnal tide in the thermosphere.

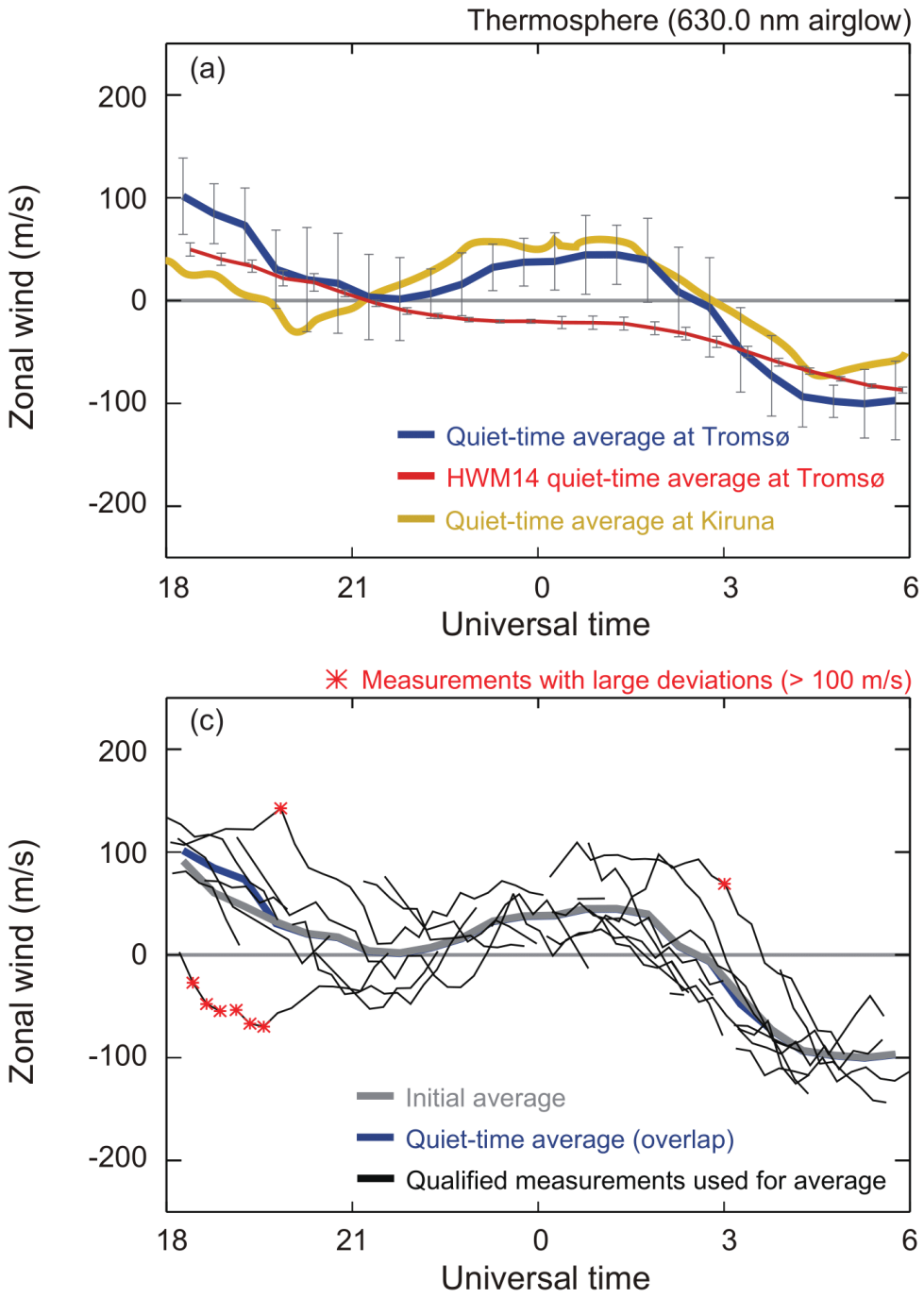

Figure 5.2 Nightside quiet-time average zonal wind in thermosphere (200–300 km) at Tromsø. The data were averaged in 0.5 h bins. (a) Quiet-time average zonal wind. In quiet times, the HWM14-derived average wind at Tromsø and average wind at Kiruna of Aruliah et al. [1999] are also shown. (b) Qualifying wind measurements satisfying both globally and locally quiet conditions, from which initial average wind is calculated. Red asterisks indicate those wind measurements with large deviations (> 100 m/s) from the initial average wind. We artificially shifted the HWM wind to a few minutes later to avoid overlapping of error bars.

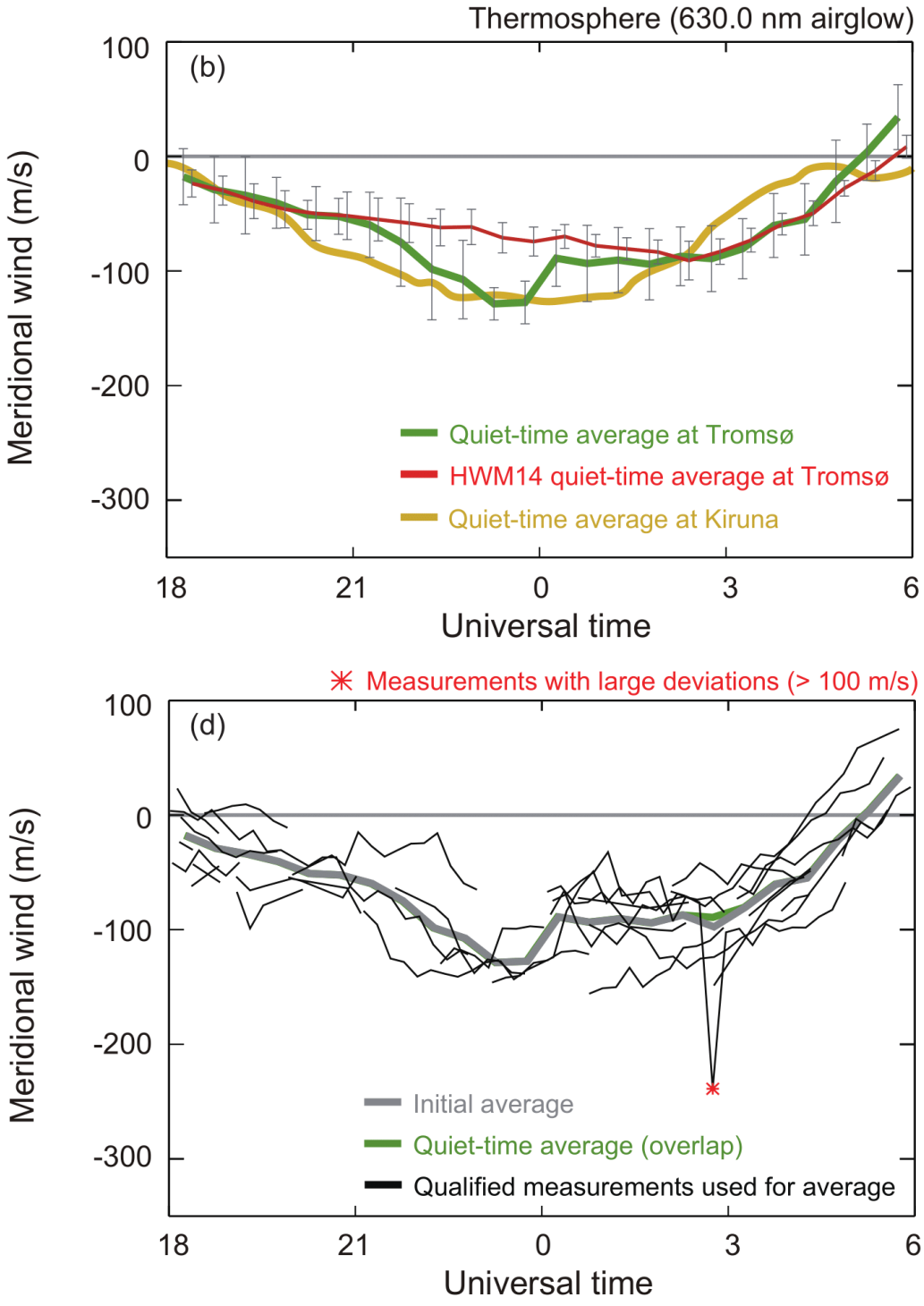

Figure 5.3 Nightside quiet-time average meridional wind in thermosphere at Tromsø, using similar format in Figure 5.2.

5.3 Discussion of Quiet-time Average Winds

5.3.1 Comparison with Model and Satellite Winds

For the HWM14-derived average winds in Figures 5.2 and 5.3, we first calculated the model-based local winds corresponding to all the time segments used in quiet-time average winds. We chose the simultaneous Ap index as the input of the HWM14 model. The height was chosen to be 250 km.We then calculated the averages in the same way as we did for the actual observations. Again, the half-length of an error bar corresponds to the standard deviation of all the winds used to calculate the average in that bin. Note that the HWM-derived average winds have been shifted artificially to a few minutes later in Figures 5.2 and 5.3 to avoid overlapping of error bars, although they were calculated using the same time bins as those used for the quiet-time average winds.

In Figure 5.3a, the diurnal-tide structure of the HWM14-derived meridional wind is consistent with actual observations, although the model predicts lower speeds near midnight. In Figure 5.2a, HWM14 fails to predict the observed westward increase of zonal wind before midnight. These results suggest that further improvements are required for the HWM to demonstrate the quiet-time winds at high latitudes.

The GOCE satellite provides direct wind measurements at both dawn and dusk sectors at an altitude of ~250 km. As shown in Figure 8 of Dhadly et al. [2017], the quiet-time average cross-track wind in December Solstice at 65–70 °N geomagnetic latitudes has a MLT coverage at ~6:30–9:00 and ~16:00–18:30, which correspond to ~4:00–6:30 UT and ~13:30–16:00 UT at Tromsø, respectively. The average cross-track wind of GOCE at ~6:30 MLT is westward in geomagnetic coordinates with an amplitude of ~100 m/s, which is comparable to the observed zonal wind at 4:00 UT in this study in geographic coordinates.

5.3.2 Comparison with F-region Wind at Kiruna

In Figures 5.2a and 5.3a, we showed the quiet-time average winds with Kp $\leqslant 2^-$ obtained from a 630 nm FPI at Kiruna, Sweden. Figure 1.8 in Chapter 1 showed this result of Aruliah et al. [1999]. They averaged 42 ±15 wind measurements in each 15-min bin. For the zonal wind, both Tromsø and Kiruna exhibit an obvious westward increase of zonal wind before midnight, something that Aruliah et al. [1999]

suggested could be caused by westward plasma convection. At F-region height, the effect from tidal components other than the diurnal tide is minor, and the ion drag effect is more effective than at E-region height [e.g., Mayr and Harris, 1978; Richmond et al,. 2003]. Therefore, we speculate that the observed westward increase of zonal wind at Tromsø is most likely related to the westward plasma convection at the dusk side, which is expected from the usual two-cell plasma convection pattern [e.g., Heppner and Maynard, 1987; Thomas and Shepherd, 2018].

Note that the westward increase of zonal wind at dusk side is slightly larger and earlier (before 20 UT) at Kiruna. This westward increase ceases and starts to increase eastward at ~20 UT at Kiruna and at ~22 UT at Tromsø. We therefore explore the possible reasons for this 2 h time difference. Aruliah et al. [1999] used north and west FPI scans at an elevation angle of 30 °. If we assume that the thermospheric wind measurements in this study were obtained right above Tromsø at an altitude of 250 km, then the spatial differences in wind measurements between this study and Aruliah et al. [1999] are ~400 km and ~250 km for the zonal and meridional directions, respectively. At the zonal-wind measurement point at Kiruna, the MLT is ~2.3 h ahead of UT and the geomagnetic latitude is ~65.20 °N, both of which are close to the corresponding values at Tromsø (2.5 h, 66.64 °N). Consequently, the 2 h time difference in zonal wind variations between Kiruna and Tromsø is unlikely to have been caused by the location difference.

Before midnight, the direction of ionospheric plasma convection changes abruptly from westward into eastward near the Harang discontinuity at the equatorward side of the auroral zone [e.g., Heppner and Maynard, 1987; Erickson et al., 1991; Koskinen and Pulkkinen, 1995]. The Harang discontinuity may be the cause of the westward decrease and subsequent eastward increase of zonal wind in Figure 5.2a. Aruliah et al. [1999] showed that the eastward turning of convection direction at the Harang discontinuity occurs at earlier MLT with increasing geomagnetic activities. In Figure 5.2a, the zonal wind of Aruliah et al. [1999] was obtained with Kp $\leqslant$ 2^-, whereas this study at Tromsø was obtained with Kp $\leqslant$ 1^+. The different geomagnetic activity level may be the cause of the 2-h time difference in zonal wind variations between Kiruna and Tromsø. At dawn side, the different threshold of Kp index may also contribute to the different zonal winds between two stations.

5.4 Events with Large Deviations from Averages and Discussion

We found wind measurements in five nights during which there were large deviations (> 100 m/s) from quiet-time averages. These large deviations are shown in Figures 5.2b and 5.3b. For two of them (events with large deviations in zonal winds before 20 UT), we show the entire measurement over the corresponding night in Figures 5.4 and 5.5 (events E1 and E2). In Figures 5.4a, 5.4b, 5.5a, and 5.5b, the blue rectangle at the top of the panel indicates the quiet-time period as defined in Subsection 5.1. The red rectangle indicates the interval in which there was large deviation from the quiet-time average winds. The light blue curve indicates the quiet-time average winds shown in Figures 5.2a and 5.3a. Figures 5.4c–5.4e and 5.5c–5.5e show the X-component of the magnetometer data, the AE and AL indices, and the B_y and Bz components of the IMF in GSM coordinates. For events E1 and E2, the large deviations in zonal winds lasted for 0.5–1 h, while the meridional winds showed well consistency with the averages. Note the presence of substorm activity right after the event time in Figures 5.4a and 5.4b. The aurora identified by the all-sky images expanded southward into the FPI scanning region at the same time. It was cloudy before 19 UT and after 22 UT as shown by the gray rectangles in Figures 5.5a and 5.5b, and measurements made during these time periods were excluded when calculating the quiet-time average winds.

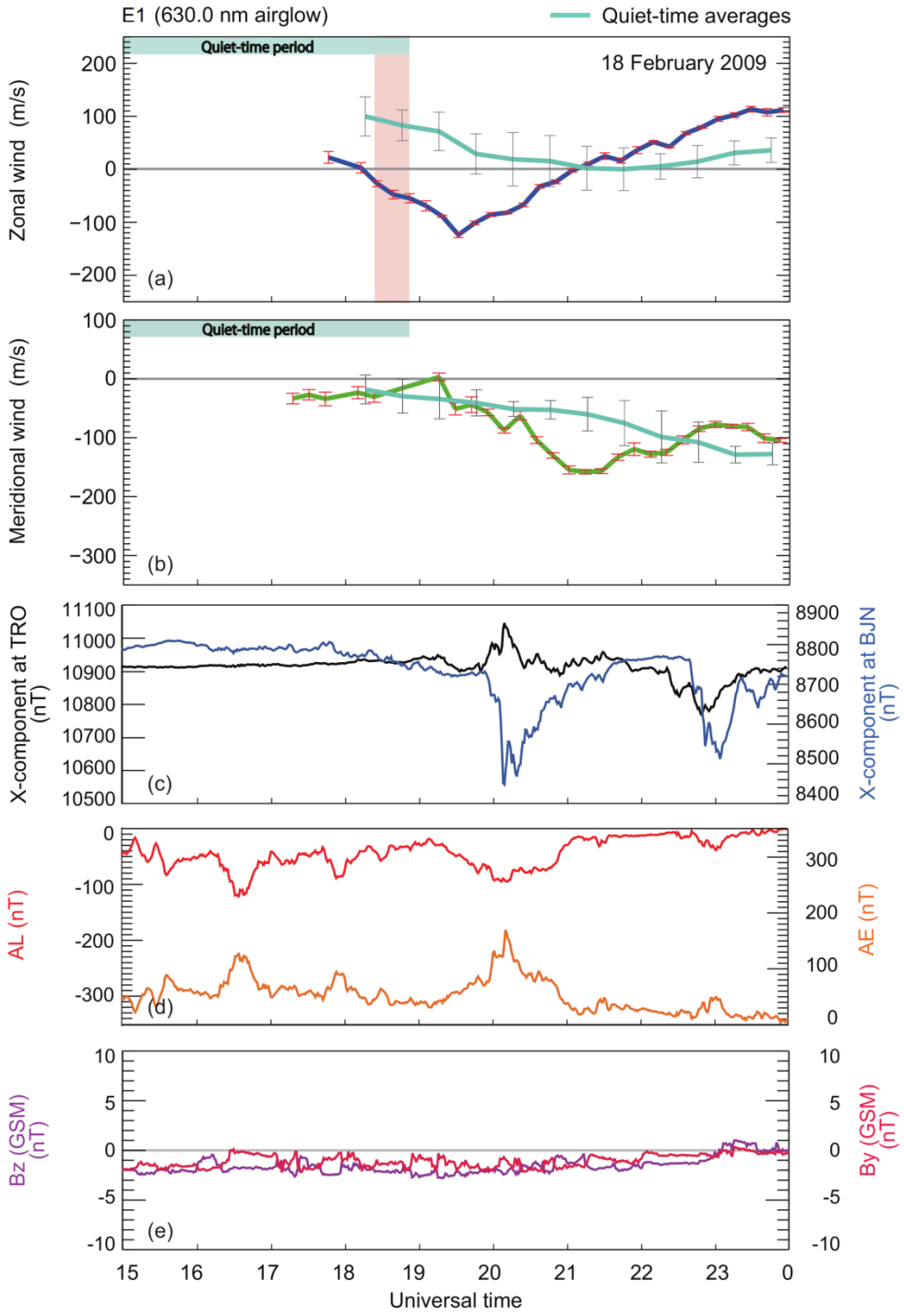

Figure 5.4 One thermospheric wind measurement (event E1) during geomagnetically quiet times, whose zonal wind showed large deviation (> 100 m/s) from quiet-time average wind. (a) Zonal wind. (b) Meridional wind. (c) X-component of magnetometer data at Tromsø and Bear Island. (d) AE and AL indices. (e) IMF B_y and B_z in GSM coordinates. The blue rectangle indicates the quiet-time period. The red rectangle indicates the interval of the deviated wind measurements. The light blue curve indicates the quiet-time average wind.

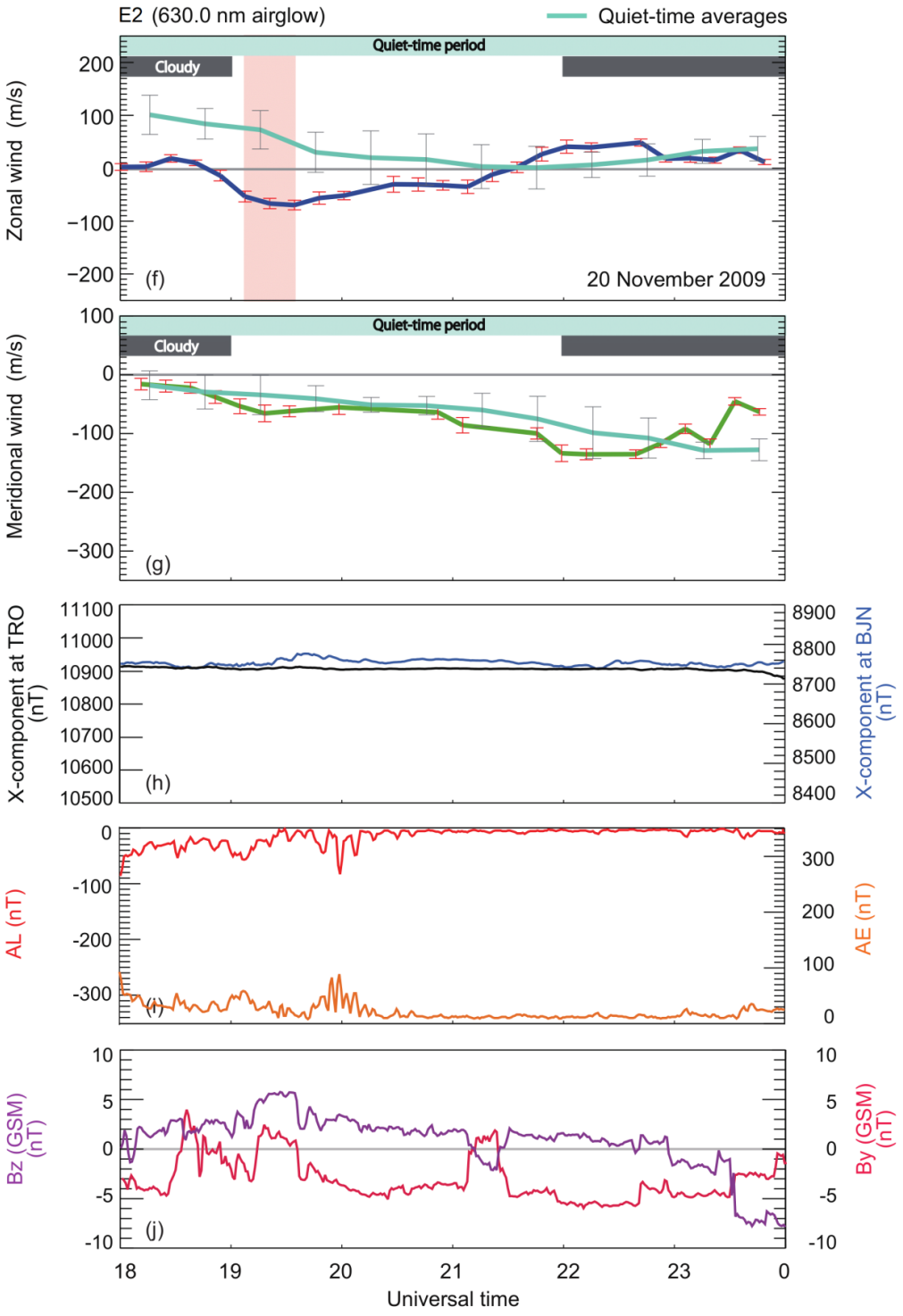

Figure 5.5 Another thermospheric wind measurement (event E2) during geomagnetically quiet times, whose zonal wind showed large deviation (> 100 m/s) from quiet-time average wind. This plot uses similar format in Figure 5.4. The dark gray rectangle indicates times of cloud.

Before and during events E1 and E2, weak auroral activities were identified at the northern edge of the all-sky images at Tromsø. However, no substorm could be identified at Bear Island from the magnetometer data. Because the measurements and the average in the meridional direction are consistent, it is unlikely that these large zonal wind deviations were caused by the Joule heating occurring to the north of Tromsø. The AE and AL indices show some substorm activities with amplitudes of less than ~100 nT on a global scale, although we ensured Kp $\leqslant$ 1^+ for both events. These substorms probably occurred elsewhere at different LTs from that at Tromsø.

At high latitudes, the ion drag in the F region is more effective than that in the E region [e.g., Mayr and Harris, 1978; Richmond et al., 2003]. Considering the two-cell plasma convection pattern [e.g., Weimer, 1995], westward convection is expected above Tromsø associated with these AE and AL activities before and during events E1 and E2. Therefore, we suggest that the plasma convection associated with substorms that occurred at different LTs might cause a westward drive to the thermosphere above Tromsø in these two events, although the ion motion may have been dominated by neutral wind at high latitudes under the condition of weak electric field [e.g., Fujii et al., 1998]. Thus, even if small substorm activity with AE < 100 nT occurs at different LTs, the zonal wind at Tromsø may be deviated by more than 100 m/s. Previous studies also reported that strong plasma convection can occur at high latitudes during quiet times [e.g., Nishitani et al., 2003].

We also checked the plasma data from the SuperDARN and EISCAT radar, as well as the global convection map from the SuperDARN radar and a data assimilation model [Ruohoniemi and Baker, 1998]. However, we found no useful convection data for events E1 and E2. For these two events, the plasma convection pattern provided by the SuperDARN convection model showed a very small convection area at high latitudes (> 70 °N in geomagnetic latitude), and Tromsø was outside that area. However, we speculated that some weak westward plasma convection at Tromsø may not been seen in the SuperDARN convection model.

5.5 Subtraction of Average Winds in the Event Study

The results of quiet-time average winds at Tromsø are shown in Figures 5.2 and 5.3. In Chapter 4, we reported the event study of thermospheric wind variations at local substorm onsets. In order to remove the influence from phenomena with longer time periods (e.g., tidal variation), we then subtracted the deviation due to quiet-time

average winds from the wind measurements in previous event study. For each of events R1–R4 shown in Figures 4.6 and 4.7, we calculated the variation of quiet-time average winds at local substorm onsets using the same method in Equations 4.1 and 4.2. Because the bin size of 0.5 h in average wind plots is same with the time interval applied in Equation 4.2, the result using Equation 4.1 equals to the individual value itself in average wind plots. Finally, we subtracted these values from the observed thermospheric wind variations at local substorm onsets shown in Table 4.1. The results of thermospheric wind variations at local substorm onsets of events R1–R4 after the subtraction are shown in Table 5.3.

Table 5.3 Thermospheric wind variations at local substorm onsets after the subtraction of quiet-time average winds.

Event (component)	Local time	Wind variation (m/s)	Deviation due to quiet-time average winds (m/s)	Wind variation after the subtraction (m/s)
R1 (zonal)	01:18	+17.5	+6.4	+11.1
R1 (meridional)	01:18	-18.4	-4.6	-13.8
R2 (zonal)	20:25	+48.9	-42.7	+91.6
R2 (meridional)	20:25	-41.8	-6.6	-35.2
R3 (zonal)	23:23	+32.3	+9.1	+23.2
R3 (meridional)	23:23	+35.5	-9.0	+44.5
R4 (zonal)	01:46	+24.5	+0.1	+24.4
R4 (meridional)	01:46	-23.0	+2.9	-25.9

In Table 5.3, we can see that all the zonal winds of events R1–R4 increased eastward at local substorm onsets, even after we subtracted the deviations due to quiet-time average winds. This is the same conclusion with that we obtained without the subtraction of quiet-time winds. For the meridional winds, the amplitudes of wind variations become smaller (larger) for events R1 and R2 (R3 and R4). In general, all the directions of wind variations in both zonal and meridional winds are not changed after the subtraction. The amplitudes of wind variations in most events do not change much after the subtraction, except for the zonal wind of event R2. As a result, both the directions and amplitudes of wind variations show good consistency before and after the subtraction of quiet-time average winds.

These results indicate that the observed thermospheric wind variations at local substorm onsets are much smaller compared with typical plasma convection speed in the auroral zone even after we subtracted the deviations due to quiet-time average

winds. Thus, all the main conclusions in Chapter 4 are preserved. Compared with tidal variations with longer time periods, these results also suggest that the substorm-associated phenomena with short time periods (e.g., intensification of plasma convection) are the main contributors to the observed thermospheric wind variations at local substorm onsets.

5.6 Conclusions

Using an FPI at Tromsø in Norway, we focused on the high-latitude nightside average thermospheric winds during geomagnetically quiet times. The wind data were collected from red-line emission (630.0 nm, altitude: 200–300 km) during 2009–2015. This was the first time that direct wind measurements from an FPI have been used to obtain the quiet-time average thermospheric winds at Tromsø. We applied these results to previous event study at local substorm onsets. The main results of this chapter are summarized as follows.

1. The average zonal wind at Tromsø exhibits a westward increase from the typical diurnal tide variation before midnight, with a minimum value of ~0 m/s centered at 21–22 UT. This can be caused by the westward plasma convection at the dusk side. After 22 UT, the zonal wind recovers eastward and then turns westward after midnight. The maximum speed of the zonal wind is ~100 m/s at both the dusk and dawn sides. The average meridional wind is an equatorward wind with a minimum value of -130 m/s around midnight, which is a typical signature of a diurnal tide in the thermosphere. The wind pattern observed at Tromsø is similar to that at Kiruna by Aruliah et al. [1999], although the decrease of zonal wind at Tromsø before the midnight occurs 2 h later than that at Kiruna.

2. At Tromsø, HWM14 predicts a meridional wind with smaller amplitude and fails to predict the decrease in zonal wind before midnight. This suggests that some improvements are necessary for the HWM to demonstrate the quiet-time thermospheric winds at high latitudes.

3. We reported two events during geomagnetically quiet time that exhibited large deviations (> 100 m/s) from the quiet-time average winds. We speculate that the westward increases of zonal wind (> 100 m/s) before the midnight are caused by the plasma convections associated with weak substorm activities that occur at LTs different from that at Tromsø. This fact implies that even if small substorm activity with AE < ~100 nT occurs at different LTs, the zonal wind at Tromsø may be deviated

by more than 100 m/s.

4. We subtracted the deviations due to quiet-time average winds from the observed thermospheric wind variations at local substorm onsets in Chapter 4. Both the amplitudes and directions of wind variations show well consistency before and after the subtraction. All the main conclusions in Chapter 4 are preserved. These results suggest that compared with tidal variations with longer time periods, the substorm-associated phenomena with short time periods (e.g., intensification of plasma convection) are the main contributors to the observed thermospheric wind variations at local substorm onsets.

Chapter 6
General Conclusions

6.1 Concluding Remarks

Substorms are fundamental geomagnetic and auroral disturbances with time scales of two to three hours. Among various substorm models, one intense debate is about the onset mechanisms of substorms. Besides, it is also important to study how substorm influences the Earth's upper atmosphere at substorm onsets. In this thesis, we have studied the onset mechanisms of substorms both in the magnetosphere and the ionosphere, and showed how the high-latitude ionosphere and thermosphere can be affected by local substorm onsets. We analyzed various data obtained from both satellite and ground-based instruments, and applied several empirical models. We can summarize the conclusions of this thesis as follows.

For the first topic in Chapter 2, we focused on the magnetospheric processes of substorm onsets. For the first time, we statistically studied severe magnetic fluctuations in the near-Earth magnetotail at 6–12 R_E. These fluctuations may cause non-MHD effect in the magnetotail, which are necessary for current disruption in the inside-out substorm model. We used magnetic field data in 2013–2014 obtained by the THEMIS-E satellite (sampling rate: 4 Hz). We identified 3322 severe magnetic fluctuation events that satisfied the criteria $\sigma_B/\bar{B} > 0.5$, where σ_B and $\bar{B}$ are the standard deviation and the average value of magnetic field intensity during the time interval of the local proton gyroperiod, respectively. We found that the occurrence rates of severe magnetic fluctuation events are 0.00312 %, 0.0312 %, and 0.0675 % at 6–8, 8–10, and 10–12 R_E, respectively. Most events lasted for no more than 20 s. Based on these occurrence rates, we assumed that four substorms with 5 min intervals of current disruption occur every day, and estimated the possible scale sizes of current disruption by severe magnetic fluctuations as 11.47 R_E^3. The fluctuation events occurred most frequently at the Z_{GSM} (Z distance in the GSM coordinates) close to the model neutral sheet position within 0.2 R_E. Most events occurred in association with sudden decreases in the AL index and magnetic field dipolarization, indicating that they are near substorm onsets or substorm expansion phase. Forty-seven percent of

fluctuation events were accompanied by ion flow with total speed $V > 100$ km/s, indicating that for half of cases the violation of ion gyromotion tends to occur during high-speed flow in the near-Earth magnetotail. The superposed epoch analysis also indicated that the speed of plasma flow increases before the severe magnetic fluctuations. We discuss how both the inside-out and outside-in substorm models can explain such phenomenon.

For the second topic in Chapter 3, we investigated the spectral property of the severe magnetic fluctuations in the near-Earth magnetotail. We selected multiple-fluctuation events with long lasting timescales using the measurements of THEMIS-D and E for 2008–2018. We further extracted 36 dipolarization events with severe magnetic fluctuations. For thirty of dipolarization events, the total ion speed already started to increase before the dipolarization, suggesting that for most cases the earthward plasma flows cause magnetic fluctuations. Using FFT, we calculated the PSDs of magnetic fluctuations during dipolarization events. We showed the average PSDs of magnetic fluctuations sorted by (a) the distance to the neutral sheet and (b) ambient magnetic field intensity. In all groups, the slope of average PSD changes steeper abruptly from below ~$10^{-1.3}$ Hz to above ~$10^{-1.3}$ Hz (0.05 Hz). This peak at ~$10^{-1.3}$ Hz (0.05 Hz) is consistent with previous studies. We also see a clear increase of slope in average PSDs at 0.05–0.1 Hz in two groups with larger ambient magnetic field intensity, implying that the magnetic fluctuations have a relatively strong power near the proton gyrofrequency and may contribute to the non-MHD effect in proton motion.

For the third topic in Chapter 4, we focused on the ionospheric and thermospheric processes at substorm onsets. Energy input from the magnetosphere during substorms can strongly affect the high-latitude thermosphere. On the other hand, the wind-induced ionospheric current at substorm onsets may provide a feedback to the substorm development in the magnetosphere. For the first time, we studied the high-latitude thermospheric wind variations at local substorm onsets at Tromsø, Norway, and the possibility of such feedback mechanism. We used an FPI located at Tromsø, whose wind measurements are estimated from the Doppler shift of red-line emission (630.0 nm, altitudes: 200–300 km) of aurora and airglow. The wind data have been collected since 2009 with a time resolution of ~13 min. We carefully identified the onset times of isolated local substorms at Tromsø and obtained four events with wind measurements. All events showed eastward increases of zonal winds

at local substorm onsets. For meridional winds, these events showed southward increases except for those at midnight. The observed wind variations at local substorm onsets were less than 49 m/s, which were much smaller than the typical plasma convection speed in the auroral zone. Therefore, we speculated that the wind-induced ionospheric current at local substorm onsets does not provide strong feedback to the development of substorm expansion phase in the magnetotail. We also discussed the possible causes of observed wind variations in the context of plasma convection, diurnal tides, and arc-associated electric field.

For the fourth topic in Chapter 5, we investigated the average winds in the thermosphere during geomagnetically quiet times. The quiet-time average winds provide a baseline wind in the upper atmosphere, but they remain insufficiently understood at Tromsø. We used wind data for 2009–2015 obtained from the same FPI at Tromsø. On average, the zonal wind shows a westward increase compared with diurnal tidal wind before midnight. A maximum speed of 100 m/s occurs at both the dusk and dawn sides. The meridional wind has a diurnal-tide structure with a minimum value of -130 m/s near midnight. We also reported occasionally large wind deviations (> 100 m/s) from the averages, even during geomagnetically quiet times. We discussed the mechanisms that may affect quiet-time average winds. Finally, we subtracted the deviations due to quiet-time average winds from the observed thermospheric wind variations at local substorm onsets in the previous event study. The results suggested that the substorm-associated winds with shorter time period are the main contributors to the observed wind variations at local substorm onsets.

Based on Chapters 2−5, we can make the following general conclusions of this thesis: (1) Substorm onset is unlikely to be caused by severe magnetic fluctuations in the near-Earth magnetotail or by thermospheric wind variations at high latitudes, although we did not completely deny the scenarios of substorm onset in inside-out and MIC substorm models. (2) At local substorm onsets, high-latitude thermospheric wind can be affected by plasma convection and diurnal tide, and is dominated by substorm-associated energy input from the magnetosphere, such as plasma convection.

6.2 Future Perspectives

In this thesis, we conducted various analyses focusing on substorm onsets. We suggest some future researches as follows.

1. In Chapter 2, we focused on the severe magnetic fluctuations in the near-Earth magnetotail. The time sequence between the occurrence of magnetic fluctuations and earthward plasma flows is crucial, because the outside-in and inside-out substorm models suggest opposite explanations about their relationship. The statistical analysis in this thesis indicated that the plasma flows occur at first and cause magnetic fluctuations, suggesting the outside-in model. However, it is possible that the observed plasma flow is caused by another magnetic fluctuation that occurs at the earthward side of the satellite location, which supports the scenario of rarefaction wave in the inside-out model (as we discussed in Subsection 2.2.4). Because THEMIS mission has radially distributed probes in the magnetotail, a simultaneous measurement from multiple probes is constructive in future research when discussing the relationship between magnetic fluctuations and plasma flows in the magnetotail.

2. In Chapter 4, the event study of thermospheric wind variations at local substorm onset was based on a limited number of events. It is valuable to conduct a statistical approach including sufficient number of events. In that case, we can also discuss the dependence of wind variations at local substorm onsets on various parameters, such as IMF and $F_{10.7}$ index. Ritter et al. [2010] conducted a statistical analysis of thermospheric wind variations at substorm onsets using the measurements of CHAMP satellite. However, the wind measurements of satellite and FPI are obtained at different altitudes. It is worth to include more FPI measurements in related research.

3. In Chapters 4 and 5, we did not obtain any real-time plasma convection data from SuperDARN and EISCAT radars for the observed wind events. The coupling between thermosphere and ionosphere occurs predominantly at high latitudes. Therefore, the simultaneous measurements of thermospheric wind and plasma convection are important. Such comparison has been reported when discussing the thermospheric winds at high latitudes during substorm recovery phase by Oyama et al. [2016]. The direct measurement of plasma convection can also contribute to the investigation of substorm onset mechanisms, as described in Subsection 4.4. The mid-latitude SuperDARN radar with a newly developed fitting algorithm can significantly increase the amount of convection measurement at high latitudes for the

substorm study [Nishitani et al., 2019]. We suggest that simultaneous measurements of thermospheric wind and plasma convection should be made in future researches focusing on substorm onsets.

Abbreviations

AE: auroral electrojet;
AL: amplitude lower;
AMPTE/CCE: Active Magnetospheric Particle Tracer Explorers/Charge Composition Explorer;
AU: amplitude upper;
BBF: bursty bulk flow;
CECL: cowling electrojet current loop;
CHAMP: Challenging Minisatellite Payload;
DE: Dynamics Explorer;
EISCAT: European Incoherent Scatter;
ESA: electrostatic analyzer;
FAC: field-aligned current;
FFT: Fast Fourier Transform;
FGM: fluxgate magnetometer;
FOV: field-of-view;
FPI: Fabry-Perot interferometer;
GOCE: Gravity Field and Steady-State Ocean Circulation Explorer;
GSM: geocentric solar magnetospheric;
HWM: Horizontal Wind Model;
IMAGE: International Monitor for Auroral Geomagnetic Effects;
IMF: interplanetary magnetic field;
LT: local time;
MHD: magnetohydrodynamics;
MIC: magnetosphere-ionosphere coupling;
MLT: magnetic local time;
NENL: near-Earth neutral line;
PSD: power spectral density;
SuperDARN: Super Dual Auroral Radar Network;
THEMIS: Time History of Events and Macroscale Interactions during Substorms;
UT: universal time.

References

Aikio, A. T., H. J. Opgenoorth, M. A. L. Persson, and K. U. Kaila (1993), Ground-based measurements of an arc-associated electric field, J. Atmos. Terr. Phys., 55, 797–808, doi:10.1016/0021-9169(93)90021-P.

Akasofu, S.-I. (1964), The development of the auroral substorm, Planet. Space Sci., 12, 273–282, doi:10.1016/0032-0633(64)90151-5.

Angelopoulos, V., C. F. Kennel, F. V. Coroniti, R. Pellat, M. G. Kivelson, R. J. Walker, C. T. Russell, W. Baumjohann, W. C. Feldman, and J. T. Gosling (1994), Statistical characteristics of bursty bulk flow events, J. Geophys. Res., 99, 21257–21280, doi:10.1029/94JA01263.

Angelopoulos, V. (2008), The THEMIS Mission, Space Sci. Rev., 141, 5–34, doi:10.1007/s11214-008-9336-1.

Aruliah, A. L., D. Rees, T. J. Fuller-Rowell (1991), The combined effect of solar and geomagnetic activity on high latitude thermospheric neutral winds. Part I. Observations, J. Atmos. Terr. Phys., 53(6–7), 467–483, doi:10.1016/0021-9169(91)90075-i.

Aruliah, A. L., I. C. F. Müller-Wodarg, and J. Schoendorf (1999), Consequences of geomagnetic history on the high-latitude thermosphere and ionosphere: averages, J. Geophys. Res., 104(A12), 28073–28088, doi:10.1029/1999JA900334.

Auster, H. U., K. H. Glassmeier, W. Magnes, O. Aydogar, W. Baumjohann, D. Constantinescu, D. Fischer, K. H. Fornacon, E. Georgescu, P. Harvey, O. Hillenmaier, R. Kroth, M. Ludlam, Y. Narita, R. Nakamura, K. Okrafka, F. Plaschke, I. Richter, H. Schwarzl, B. Stoll, A. Valavanoglou, and M. Wiedemann (2008), The THEMIS Fluxgate Magnetometer, Space Sci. Rev., 141, 235–264, doi:10.1007/978-0-387-89820-9_11.

Baker, D. N., T. I. Pulkkinen, V. Angelopoulos, W. Baumjohann, and R. L. McPherron (1996), Neutral line model of substorms: Past results and present view, J. Geophys. Res., 101, 12975–13010, doi:10.1029/95JA03753.

Baron, M. J., and R. H. Wand (1983), F-region ion temperature enhancements resulting from Joule heating, J. Geophys. Res., 88, 4114–4118, doi:10.1029/JA088iA05p04114.

Batten, S., and D. Rees (1990), Thermospheric winds in the auroral oval: observations of small scale structures and rapid fluctuations by a Doppler Imaging System, Planet. Space Sci., 38(5), 675–694, doi:10.1016/0032-0633(90)90074-Z.

Bauer, T. M., W. Baumjohann, R. A. Treumann, N. Sckopke, and H. Lühr (1995), Low-frequency waves in the near-Earth plasma sheet, J. Geophys. Res., 100, 9605–9617, doi:10.1029/95JA00136.

Baumjohann, W., G. Paschmann, and H. Lühr (1990), Characteristics of high-speed ion flows in the plasma sheet, J. Geophys. Res., 95, 3801–3809, doi:10.1029/JA095iA04p03801.

Baumjohann, W., M. Hesse, S. Kokubun, T. Mukai, T. Nagai, and A. A. Petrukovich (1999), Substorm dipolarization and recovery, J. Geophys. Res., 104, 24995–25000, doi:10.1029/1999JA900282.

Birn, J., and M. Hesse (1996), Details of current disruption and diversion in simulations of magnetotail dynamics, J. Geophys. Res., 101(A7), 15345–15358, doi:10.1029/96JA00887.

Borovsky, J. E., R. J. Nemzek, and R. D. Belian (1993), The occurrence rate of magnetospheric-substorm onsets: Random and periodic substorms, J. Geophys. Res., 98, 3807–3813, doi:10.1029/92JA02556.

Borovsky, J. E., and K. Yakymenko (2017), Substorm occurrence rates, substorm recurrence times, and solar wind structure, J. Geophys. Res., 122, 2973–2998, doi:10.1002/ 2016JA023625.

Brekke, A. (1997), Physics of the upper polar atmosphere, Wiley, Hoboken, p 192, doi:10.1007/978-3-642-27401-5.

Bristow, W. A., and P. Jensen (2007), A superposed epoch study of SuperDARN convection observations during substorms, J. Geophys. Res., 112, A06232, doi:10.1029/2006JA012049.

Burke, W. J., M. S. Gussenhoven, M. C. Kelley, D. A. Hardy, and F. J. Rich (1982), Electric and magnetic field characteristics of discrete arcs in the polar cap, J. Geophys. Res., 87(A4), 2431–2443, doi:10.1029/JA087iA04p02431.

Cai, L., S. Oyama, A. Aikio, H. Vanhamäki, and I. Virtanen (2019), Fabry-Perot interferometer observations of thermospheric horizontal winds during magnetospheric substorms, J. Geophys. Res., 124, 3709–3728, doi:10.1029/2018JA026241.

Carlson, H. C., R. A. Heelis, E. J. Weber, and J. R. Sharber (1988), Coherent

mesoscale convection patterns during northward interplanetary magnetic field, J. Geophys. Res., 93(A12), 14501–14514, doi:10.1029/JA093iA12p14501.

Chen, F. F. (1983), Introduction to Plasma Physics and Controlled Fusion, Plasma Physics, 2nd Edn., Plenum Press, 1, 20, ISBN:0-306-41332-9.

Chu, X., R. L. McPherron, T.-S. Hsu, and V. Angelopoulos (2015), Solar cycle dependence of substorm occurrence and duration: Implications for onset, J. Geophys. Res., 120, 2808–2818, doi:10.1002/2015JA021104.

Conde, M., and R. W. Smith (1998), Spatial structure in the thermospheric horizontal wind above Poker Flat, Alaska, during solar minimum, J. Geophys. Res., 103(A5), 9449–9471, doi:10.1029/97JA03331.

Conde, M., J. D. Craven, T. Immel, E. Hoch, H. Stenbaek-Nielsen, T. Hallinan, R. W. Smith, J. Olson, and Wei Sun (2001), Assimilated observations of thermospheric winds, the aurora, and ionospheric currents over Alaska, J. Geophys. Res., 106(A6), 10493–10508, doi:10.1029/2000JA000135.

Consolini, G., M. Kretzschmar, A. T. Y. Lui, G. Zimbardo, and W. M. Macek (2005), On the magnetic field fluctuations during magnetospheric tail current disruption: A statistical approach, J. Geophys. Res., 110, A07202, doi:10.1029/2004JA010947.

David, M., J. J. Sojka, and R. W. Schunk (2016), How uncertainty in the neutral wind limits the accuracy of ionospheric modeling and forecasting, J. Geophys. Res., 121, 519–528, doi:10.1002/2015JA021544.

Davis, T. N., and M. Sugiura (1966), Auroral electrojet activity index AE and its universal time variations, J. Geophys. Res., 71, 785–801, doi:10.1029/JZ071i003p00785.

Deng, W., T. L. Killeen, A. G. Burns, and R. G. Roble (1991), The flywheel effect: ionospheric currents after a geomagnetic storm, Geophys. Res. Lett., 18, 1845–1848, doi:10.1029/91GL02081.

Deng, Y., T. J. Fuller-Rowell, R. A. Akmaev, and A. J. Ridley (2011), Impact of the altitudinal Joule heating distribution on the thermosphere, J. Geophys. Res., 116, A05313, doi:10.1029/2010JA016019.

Dhadly, M., J. Emmert, D. Drob, M. Conde, E. Doornbos, G. Shepherd, J. Makela, Q. Wu, R. Niciejewski, and A. Ridley (2017), Seasonal dependence of northern high-latitude upper thermospheric winds: A quiet time climatological study based on ground-based and space-based measurements, J. Geophys. Res., 122,

2619–2644, doi:10.1002/2016JA023688.

Doe, R. A., J. F. Vickrey, and M. Mendillo (1995), Electrodynamic model for the formation of auroral ionospheric cavities, J. Geophys. Res., 100(A6), 9683–9696, doi:10.1029/95JA00001.

Drob, D. P., J. T. Emmert, J. W. Meriwether, J. J. Makela, E. Doornbos, M. Conde, G. Hernandez, J. Noto, K. A. Zawdie, S. E. McDonald, J. D. Huba, and J. H. Klenzing (2015), An update to the Horizontal Wind Model (HWM): The quiet time thermosphere, Earth and Space Sci., 2, 301–319, doi:10.1002/2014EA000089.

Emmert, J. T., M. L. Faivre, G. Hernandez, M. J. Jarvis, J. W. Meriwether, R. J. Niciejewski, D. P. Sipler, and C. A. Tepley (2006a), Climatologies of nighttime upper thermospheric winds measured by ground-based Fabry-Perot interferometers during geomagnetically quiet conditions: 1. Local time, latitudinal, seasonal, and solar cycle dependence, J. Geophys. Res., 111, A12302, doi:10.1029/2006JA011948.

Emmert, J. T., G. Hernandez, M. J. Jarvis, R. J. Niciejewski, D. P. Sipler, and S. Vennerstrom (2006b), Climatologies of nighttime upper thermospheric winds measured by ground-based Fabry-Perot Interferometers during geomagnetically quiet conditions: 2. High-latitude circulation and IMF dependence, J. Geophys. Res., 111, A12303, doi:10.1029/2006JA011949.

Erickson, G. M., R. W. Spiro, and R. A. Wolf (1991), The physics of the Harang discontinuity, J. Geophys. Res., 96(A2), 1633–1645, doi:10.1029/90JA02344.

Frisch, U. (1995), Turbulence, Cambridge Univ. Press, New York, ISBN:9781139170666.

Frühauff, D., and K. H. Glassmeier (2016), Statistical analysis of magnetotail fast flows and related magnetic disturbances, Ann. Geophys., 34, 399–409, doi:10.5194/angeo-34-399-2016.

Fujii, R., S. Nozawa, S. C. Buchert, N. Matuura, and A. Brekke (1998), The motion of ions in the auroral ionosphere, J. Geophys. Res., 103(A9), 20685–20695, doi:10.1029/98JA01685.

Haerendel, G. (1992), Disruption, ballooning or auroral avalanche-On the cause of substorms, in Proceedings of the International Conference on Substorms (ICS-1), Kiruna, Sweden 23–27 March 1992, Eur. Space Agency Spec. Publ., ESA SP-335, 417–420.

Hashimoto, C., R. TanDokoro, and M. Fujimoto (2005), Effects of guide field in three-dimensional magnetic reconnection, in Frontiers in Magnetospheric Plasma Physics, COSPAR Colloq. Ser., vol. 16, edited by M. Hoshino, Y. Omura, and L. J. Lanzerotti, 130–134, Elsevier, New York.

Henderson, M. G. (2009), Observational evidence for an inside-out substorm onset scenario, Ann. Geophys., 27, 2129–2140, doi:10.5194/angeo-27-2129-2009.

Hendricks, W. A., and K. W. Robey (1936), The sampling distribution of the coefficient of variation, Ann. Math. Stat., 7, 129–132, doi:10.1214/aoms/1177732503.

Heppner, J. P., and N. C. Maynard (1987), Empirical high-latitude electric field models, J. Geophys. Res., 92(A5), 4467–4489, doi:10.1029/JA092iA05p04467.

Hones, E. W. (1973), Plasma flow in the plasma sheet and its relation to substorms, Radio Sci., 8, 979–990, doi:10.1029/RS008i011p00979.

Hwang, K.-J., M. L. Goldstein, T. E. Moore, B. M. Walsh, D. G. Baishev, A. V. Moiseyev, B. M. Shevtsov, and K. Yumoto (2014), A tailward moving current sheet normal magnetic field front followed by an earthward moving dipolarization front, J. Geophys. Res., 119, 5316–5327, doi:10.1002/2013JA019657.

Ishii, M., M. Conde, R. W. Smith, M. Krynicki, E. Sagawa, and S. Watari (2001), Vertical wind observations with two Fabry-Perot interferometers at Poker Flat, Alaska, J. Geophys. Res., 106(A6), 10537–10551, doi:10.1029/2000JA900148.

Ishii, M., M. Kubota, M. Conde, R. W. Smith, and M. Krynicki (2004), Vertical wind distribution in the polar thermosphere during Horizontal E Region Experiment (HEX) campaign, J. Geophys. Res., 109, A12311, doi:10.1029/2004JA010657.

Jacquey, C., J. A. Sauvaud, and J. Dandouras (1991), Location and propagation of the magnetotail current disruption during substorm expansion: Analysis and simulation of an ISEE multi-onset event, Geophys. Res. Lett., 18, 389–392, doi:10.1029/90GL02789.

Kan, J. R. (1993), A global magnetosphere-ionosphere coupling model of substorms, J. Geophys. Res., 98(A10), 17263–17275, doi:10.1029/93JA01168.

Kan, J. R., H. Li, C. Wang, H. U. Frey, M. V. Kubyshkina, A. Runov, C. J. Xiao, L. H. Lyu, and W. Sun (2011), Brightening of onset arc precedes the dipolarization onset: THEMIS observations of two events on 1 March 2008, Ann. Geophys., 29, 2045–2059, doi:10.5194/angeo-29-2045-2011.

Kohl, H., and J. W. King (1967), Atmospheric winds between 100 and 700 km and their effects on the ionosphere, J. Atmos. Terr. Phys., 29, 1045–1062, doi:10.1016/0021-9169(67)90139-0.

Kosch, M. J., K. Cierpka, M. T. Rietveld, T. Hagfors, and K. Schlegel (2001), High-latitude ground-based observations of the thermospheric ion-drag time constant, Geophys. Res. Lett., 28, 1395–1398, doi:10.1029/2000GL012380.

Koskinen, H. E. J., and T. I. Pulkkinen (1995), Midnight velocity shear zone and the concept of Harang discontinuity, J. Geophys. Res., 100(A6), 9539–9547, doi:10.1029/95JA00228.

Kozak, L. V., B. A. Petrenko, A. T. Y. Lui, E. A. Kronberg, E. E. Grigorenko, and A. S. Prokhorenkov (2018), Turbulent processes in the Earth's magnetotail: spectral and statistical research, Ann. Geophys., 36, 1303–1318, doi:10.5194/angeo-36-1303-2018.

Liuzzo, L. R., A. J. Ridley, N. J. Perlongo, E. J. Mitchell, M. Conde, D. L. Hampton, W. A. Bristow, and M. J. Nicolls (2015), High-latitude ionospheric drivers and their effects on wind patterns in the thermosphere, J. Geophys. Res., 120, 715–735, doi:10.1002/2014JA020553.

Lui, A. T. Y., A. Mankofsky, C.-L. Chang, K. Papadopoulos, and C. S. Wu (1990), A current disruption mechanism in the neutral sheet: A possible trigger for substorm expansions, Geophys. Res. Lett., 17, 745–748, doi:10.1029/GL017i006p00745.

Lui, A. T. Y. (1991a), A synthesis of magnetospheric substorm models, J. Geophys. Res., 96, 1849–1856, doi:10.1029/90JA02430.

Lui, A. T. Y. (1991b), Extended consideration of a synthesis model for magnetospheric substorms, in Magnetospheric Substorms, Geophys. Monogr. Ser., vol. 64, edited by J. R. Kan et al., 43–60, AGU, Washington, D.C.

Lui, A. T. Y., C.-L. Chang, A. Mankofsky, H.-K. Wong, and D. Winske (1991c), A cross-field current instability for substorm expansions, J. Geophys. Res., 96, 11389–11401, doi:10.1029/91JA00892.

Lui, A. T. Y., R. E. Lopez, B. J. Anderson, K. Takahashi, L. J. Zanetti, R. W. McEntire, T. A. Potemra, D. M. Klumpar, E. M. Greene, and R. Strangeway (1992), Current disruptions in the near-Earth neutral sheet region, J. Geophys. Res., 97, 1461–1480, doi:10.1029/91JA02401.

Lui, A. T. Y., and A.-H. Najmi (1997), Time-frequency decomposition of signals in a current disruption event, Geophys. Res. Lett., 24, 3157,

doi:10.1029/97GL03229.

Lui, A. T. Y. (2001), A multiscale model for substorms, Space Sci. Rev., 95, 325–345, doi:10.1023/A:1005217304749.

Lyons, L. R., T. L. Killeen, and R. L. Walterscheid (1985), The neutral “flywheel” as a source of quiet-time polar cap currents, Geophys. Res. Lett., 12, 101–104, doi:10.1029/GL012i002p00101.

Mayr, H. G., and I. Harris (1978), Some characteristics of electric field momentum coupling with the neutral atmosphere, J. Geophys. Res., 83(A7), 3327–3336, doi:10.1029/JA083iA07p03327.

McAllister, A. H., M. Dryer, P. McIntosh, H. Singer, and L. Weiss (1996), A large polar crown coronal mass ejection and a “problem” geomagnetic storms: April 14–23, 1994, J. Geophys. Res., 101, 13497–13515, doi:10.1029/96JA00510.

McFadden, J., C. Carlson, D. Larson, J. Bonnell, F. Mozer, V. Angelopoulos, K.-H. Glassmeier, and U. Auster (2009), THEMIS ESA First Science Results and Performance Issues, Space Sci. Rev., 141, 477–508, doi:10.1007/978-0-387-89820-9_20.

McPherron, R. L. (1970), Growth phase of magnetospheric substorms, J. Geophys. Res., 75(28), 5592–5599, doi:10.1029/JA075i028p05592.

Nagai, T. (1991), An empirical model of substorm-related magnetic field variations at synchronous orbit, in Magnetospheric Substorms, Geophys. Monogr. Ser., vol. 64, edited by J. R. Kan et al., 91–95, AGU, Washington, D. C.

Nakamura, R., W. Baumjohann, C. Mouikis, L. M. Kistler, A. Runov, M. Volwerk, Y. Asano, Z. Vörös, T. L. Zhang, B. Klecker, H. Rème, and A. Balogh (2004), Spatial scale of high-speed flows in the plasma sheet observed by Cluster, Geophys. Res. Lett., 31, L09804, doi:10.1029/2004GL019558.

Nevanlinna, H., and T. I. Pulkkinen (1998), Solar cycle correlations of substorm and auroral occurrence frequency, Geophys. Res. Lett., 25, 3087–3090, doi:10.1029/98GL02335.

Nishida, A. (1968), Geomagnetic D_p 2 fluctuations and associated magnetospheric phenomena, J. Geophys. Res., 73, 1795–1803, doi:10.1029/JA073i005p01795.

Nishitani, N., and T. Oguti (1988), Auroral Activity and Corresponding Magnetic Signatures at Synchronous Orbit, J. Geomag. Geoelectr., 40, 423–445, doi:10.5636/jgg.40.423.

Nishitani, N., V. Papitashvili, T. Ogawa, N. Sato, H. Yamagishi, A. S. Yukimatu, and F.

J. Rich (2003), Interhemispheric asymmetry of the high latitude ionospheric convection on May 11–12, 1999, J. Geophys. Res., 108(A5), 1184, doi:10.1029/2002JA009680.

Nishitani, N., J. M. Ruohoniemi, M. Lester, J. B. H. Baker, A. V. Koustov, S. G. Shepherd, G. Chisham, T. Hori, E. G. Thomas, R. A. Makarevich, A. Marchaudon, P. Ponomarenko, J. A. Wild, S. E. Milan, W. A. Bristow, J. Devlin, E. Miller, R. A. Greenwald, T. Ogawa, and T. Kikuchi (2019), Review of the accomplishments of mid-latitude Super Dual Auroral Radar Network (SuperDARN) HF Radars, Prog. Earth Planet. Sci., 6:27, doi:10.1186/s40645-019-0270-5.

Nosé, M., H. Koshiishi, H. Matsumoto, P. C:son Brandt, K. Keika, K. Koga, T. Goka, and T. Obara (2010), Magnetic field dipolarization in the deep inner magnetosphere and its role in development of O^+-rich ring current, J. Geophys. Res., 115, A00J03, doi:10.1029/2010JA015321.

Nosé, M., K. Takahashi, K. Keika, L. M. Kistler, K. Koga, H. Koshiishi, H. Matsumoto, M. Shoji, Y. Miyashita, and R. Nomura (2014), Magnetic fluctuations embedded in dipolarization inside geosynchronous orbit and their associated selective acceleration of O^+ ions, J. Geophys. Res., 119, doi:10.1002/2014JA019806.

Ohtani, S., K. Takahashi, L. J. Zanetti, T. A. Potemra, and R. W. McEntire (1992), Initial signatures of magnetic field and energetic particle fluxes at tail reconfiguration: Explosive growth phase, J. Geophys. Res., 97, 19311–19324, doi:10.1029/92JA01832.

Ohtani, S., T. Higuchi, A. T. Y. Lui, and K. Takahashi (1995), Magnetic fluctuations associated with tail current disruption: Fractal analysis, J. Geophys. Res., 100, 19135–19145, doi:10.1029/95JA00903.

Ohtani, S., K. Takahashi, T. Higuchi, A. T. Y. Lui, H. E. Spence, and J. F. Fennell (1998), AMPTE/CCE-SCATHA simultaneous observations of substorm-associated magnetic fluctuations, J. Geophys. Res., 103, 4671–4682, doi:10.1029/97JA03239.

Ono, Y., M. Nosé, S. P. Christon, and A. T. Y. Lui (2009), The role of magnetic field fluctuations in nonadiabatic acceleration of ions during dipolarization, J. Geophys. Res., 114, A05209, doi:10.1029/2008JA013918.

Opgenoorth, H. J., I. Hägström, P. J. S. Williams, and G. O. L. Jones (1990), Regions

of strongly enhanced perpendicular electric fields adjacent to auroral arcs, J. Atmos. Terr. Phys., 52, 449–458, doi:10.1016/0021-9169(90)90044-N.

Oyama, S., T. T. Tsuda, T. Sakanoi, Y. Obuchi, K. Asamura, M. Hirahara, A. Yamazaki, Y. Kasaba, R. Fujii, S. Nozawa, and B. J. Watkins (2009), Spatial evolution of frictional heating and the predicted thermospheric wind effects in the vicinity of an auroral arc measured with the Sondrestrom incoherent-scatter radar and the Reimei satellite, J. Geophys. Res., 114, A07311, doi:10.1029/2009JA014091.

Oyama, S., K. Shiokawa, Y. Miyoshi, K. Hosokawa, B. J. Watkins, J. Kurihara, T. T. Tsuda, and C. T. Fallen (2016), Lower thermospheric wind variations in auroral patches during the substorm recovery phase, J. Geophys. Res., 121, 3564–3577, doi:10.1002/2015JA022129.

Pan, D.-X., X.-Z. Zhou, Q.-Q. Shi, J. Liu, V. Angelopoulos, A. Runov, Q.-G. Zong, and S.-Y. Fu (2015), On the generation of magnetic dips ahead of advancing dipolarization fronts, Geophys. Res. Lett., 42, 4256–4262, doi:10.1002/2015GL064369.

Provan, G., M. Lester, S. B. Mende, and S. E. Milan (2004), Statistical study of high-latitude plasma flow during magnetospheric substorms, Ann. Geophys., 22, 3607–3624, doi:10.5194/angeo-22-3607-2004.

Rees, D., N. Lloyd, P. J. Charleton, and M. Carlson (1984), Comparison of plasma flow and thermospheric circulation over northern Scandinavia using EISCAT and a Fabry-Perot interferometer, J. Atmos. Terr. Phys., 46, 545–564, doi:10.1016/0021-9169(84)90073-4.

Richmond, A. D., C. Lathuillère, S. Vennerstroem (2003), Winds in the high-latitude lower thermosphere: Dependence on the interplanetary magnetic field, J. Geophys. Res., 108(A2), 1066, doi:10.1029/2002JA009493.

Rishbeth, H. (1997), The ionospheric E-layer and F-layer dynamos-a tutorial review, J. Atmos. Terr. Phys., 59, 1873–1880, doi:10.1016/S1364-6826(97)00005-9.

Ritter, P., H. Lühr, and E. Doornbos (2010), Substorm-related thermospheric density and wind disturbances derived from CHAMP observations, Ann. Geophys., 28, 1207–1220, doi:10.5194/angeo-28-1207-2010.

Runov, A., V. Angelopoulos, X.-Z. Zhou, X.-J. Zhang, S. Li, F. Plaschke, and J. Bonnell (2011), A THEMIS multicase study of dipolarization fronts in the magnetotail plasma sheet, J. Geophys. Res., 116, A05216, doi:10.1029/2010JA016316.

Ruohoniemi, J. M., and K. B. Baker (1998), Large-scale imaging of high-latitude convection with Super Dual Auroral Radar Network HF radar observations, J. Geophys. Res., 103(A9), 20797–20811, doi:10.1029/98JA01288.

Schmid, D., M. Volwerk, R. Nakamura, W. Baumjohann, and M. Heyn (2011), A statistical and event study of magnetotail dipolarization fronts, Ann. Geophys., 29, 1537–1547, doi:10.5194/angeo-29-1537-2011.

Schmid, D., R. Nakamura, M. Volwerk, F. Plaschke, Y. Narita, W. Baumjohann, W. Magnes, D. Fischer, H. U. Eichelberger, R. B. Torbert, C. T. Russell, R. J. Strangeway, H. K. Leinweber, G. Le, K. R. Bromund, B. J. Anderson, J. A. Slavin, and E. L. Kepko (2016), A comparative study of dipolarization fronts at MMS and Cluster, Geophys. Res. Lett., 43, 6012–6019, doi:10.1002/2016GL069520.

Schunk, R., and A. Nagy (2009), Ionospheres: physics, plasma physics, and chemistry, 2nd edn, Cambridge Univ. Press, Cambridge, 139–140, ISBN:9781108462105.

Sergeev, V. A., R. C. Elphic, F. S. Mozer, A. Saint-Marc, and J. A. Sauvaud (1992), A two-satellite study of nightside flux transfer events in the plasma sheet, Planet. Space Sci., 40, 1551–1572, doi:10.1016/0032-0633(92)90052-P.

Shiokawa, K., and K. Yumoto (1993), Global characteristics of particle precipitation and field-aligned electron acceleration during isolated substorms, J. Geophys. Res., 98, 1359–1375, doi:10.1029/92JA01092.

Shiokawa, K., W. Baumjohann, and G. Haerendel (1997), Braking of high-speed flows in the near-Earth tail, Geophys. Res. Lett., 10, 1179–1182, doi:10.1029/97GL01062.

Shiokawa, K., W. Baumjohann, G. Haerendel, G. Paschmann, J. F. Fennell, E. Friis-Christensen, H. Lühr, G. D. Reeves, C. T. Russell, P. R. Sutcliffe, and K. Takahashi (1998), High-speed ion flow, substorm current wedge, and multiple Pi 2 pulsations, J. Geophys. Res., 103, 4491–4507, doi:10.1029/97JA01680.

Shiokawa, K., I. Shinohara, T. Mukai, H. Hayakawa, and C. Z. Cheng (2005a), Magnetic field fluctuations during substorm-associated dipolarizations in the nightside plasma sheet around $X = 10\ R_E$, J. Geophys. Res., 110, A05212, doi:10.1029/2004JA010378.

Shiokawa, K., Y. Miyashita, I. Shinohara, and A. Matsuoka (2005b), Decrease in B_z prior to the dipolarization in the near-Earth plasma sheet, J. Geophys. Res., 110, A09219, doi:10.1029/2005JA011144.

Shiokawa, K., K. Hosokawa, K. Sakaguchi, A. Ieda, Y. Otsuka, T. Ogawa, and M. Connors (2009), The optical mesosphere thermosphere imagers (OMTIs) for network measurements of aurora and airglow, future perspectives of space plasma and particle instrumentation and international collaborations. In: AIP Conference proceedings, edited by Hirahara M, Miyoshi Y, Terada N, Shinohara I, Mukai T. AIP Conference proceedings, 212–215, doi:10.1063/1.3169292.

Shiokawa, K., Y. Otsuka, S. Oyama, S. Nozawa, M. Satoh, Y. Katoh, Y. Hamaguchi, Y. Yamamoto, and J. Meriwether (2012), Development of lowcost sky-scanning Fabry-Perot interferometers for airglow and auroral studies, Earth Planets Space, 64(11),1033–1046, doi:10.5047/eps.2012.05.004.

Slavin, J. A., R. P. Lepping, J. Gjerloev, D. H. Fairfield, M. Hesse, C. J. Owen, M. B. Moldwin, T. Nagai, A. Ieda, and T. Mukai (2003), Geotail observations of magnetic flux ropes in the plasma sheet, J. Geophys. Res., 108(A1), 1015, doi:10.1029/2002JA009557.

St.-Maurice, J. P., and W. B. Hanson (1982), Ion frictional heating at high latitudes and its possible use for an in situ determination of neutral thermospheric winds and temperature, J. Geophys. Res., 87(A9), 7580–7602, doi:10.1029/JA087iA09p07580.

Takahashi, K., L. J. Zanetti, R. E. Lopez, R. W. McEntire, T. A. Potemra, and K. Yumoto (1987), Distribution of the magnetotail current sheet observed by AMPTE/CCE, Geophys. Res. Lett., 14, 1019–1022, doi:10.1029/GL014i010p01019.

Tanskanen, E. I., T. I. Pulkkinen, A. Viljanen, K. Mursula, N. Partamies, and J. A. Slavin (2011), From space weather toward space climate time scales: Substorm analysis from 1993 to 2008, J. Geophys. Res., 116, A00I34, doi:10.1029/2010JA015788.

Thomas, E. G., and S. G. Shepherd (2018), Statistical patterns of ionospheric convection derived from mid-latitude, high-latitude, and polar SuperDARN HF radar observations, J. Geophys. Res., 123, 3196–3216, doi:10.1002/2018JA025280.

Tsyganenko, N. A. (2002a), A model of the near magnetosphere with a dawn-dusk asymmetry: 1. Mathematical structure, J. Geophys. Res., 107(A8), 1179, doi:10.1029/2001JA000219.

Tsyganenko, N. A. (2002b), A model of the near magnetosphere with a dawn-dusk

asymmetry: 2. Parameterization and fitting to observations, J. Geophys. Res., 107(A8), 1176, doi:10.1029/2001JA000220.

Valladares, C. E., and H. C. Carlson Jr. (1991), The electrodynamic, thermal, and energetic character of intense Sun-aligned arcs in the polar cap, J. Geophys. Res., 96(A2), 1379–1400, doi:10.1029/90JA01765.

Volwerk, M., R. Nakamura, W. Baumjohann, R. A. Treumann, A. Runov, Z. Vörös, T. L. Zhang, Y. Asano, B. Klecker, I. Richters, A. Balogh, and H. Réme (2003), A statistical study of compressional waves in the tail current sheet, J. Geophys. Res., 108(A12), 1429, doi:10.1029/2003JA010155.

Vörös, Z., W. Baumjohann, R. Nakamura, M. Volwerk, A. Runov, T. L. Zhang, H. U. Eichelberger, R. Treumann, E. Georgescu, A. Balogh, B. Klecker, and H. Réme (2004), Magnetic turbulence in the plasma sheet, J. Geophys. Res., 109, A11215, doi:10.1029/2004JA010404.

Weimer, D. R. (1995), Models of high-latitude electric potentials derived with a least error fit of spherical harmonic coefficients, J. Geophys. Res., 100, 19595–19607, doi:10.1029/95JA01755.

Wiltberger, M., T. I. Pulkkinen, J. G. Lyon, and C. C. Goodrich (2000), MHD simulation of the magnetotail during the December 10, 1996, substorm, J. Geophys. Res., 105, 27649–27664, doi:10.1029/1999JA000251.

Witasse, O., J. Lilensten, C. Lathuillère, and B. Pibaret (1998), Meridional thermospheric neutral wind at high latitude over a full solar cycle, Ann. Geophys., 16, 1400–1409, doi:10.1007/s00585-998-1400-3.

Xu, H. (2017a), Study of substorm onset mechanisms using the THEMIS satellite and a ground-based Fabry-Perot interferometer, Master Thesis, Nagoya University.

Xu, H., K. Shiokawa, and D. Frühauff (2017b), Statistical analysis of severe magnetic fluctuations in the near-Earth plasma sheet observed by THEMIS-E, Ann. Geophys., 35, 1131–1142, doi:10.5194/angeo-35-1131-2017.

Xu, H., K. Shiokawa, S. Oyama, and Y. Otsuka (2019a), Thermospheric wind variations observed by a Fabry-Perot interferometer at Tromsø, Norway, at substorm onsets, Earth Planets Space, 93(71), doi:10.1186/s40623-019-1072-0.

Xu, H., K. Shiokawa, S. Oyama, and S. Nozawa (2019b), High-latitude thermospheric wind study using a Fabry-Perot interferometer at Tromsø in Norway: averages and variations during quiet times, Earth Planets Space, 110(71), doi:10.1186/s40623-019-1093-8.

Appendix

In this appendix, we demonstrate all the results based on green-line wind measurements (557.7 nm, altitudes: 90–100 km) which are not shown in Chapters 4 and 5. These results possibly contain ambiguity due to the emission height change. These results have not been published in journal paper, although we think they are worth for reporting. We provide necessary information about these results in the captions of following figures, but refrain from making detailed discussion.

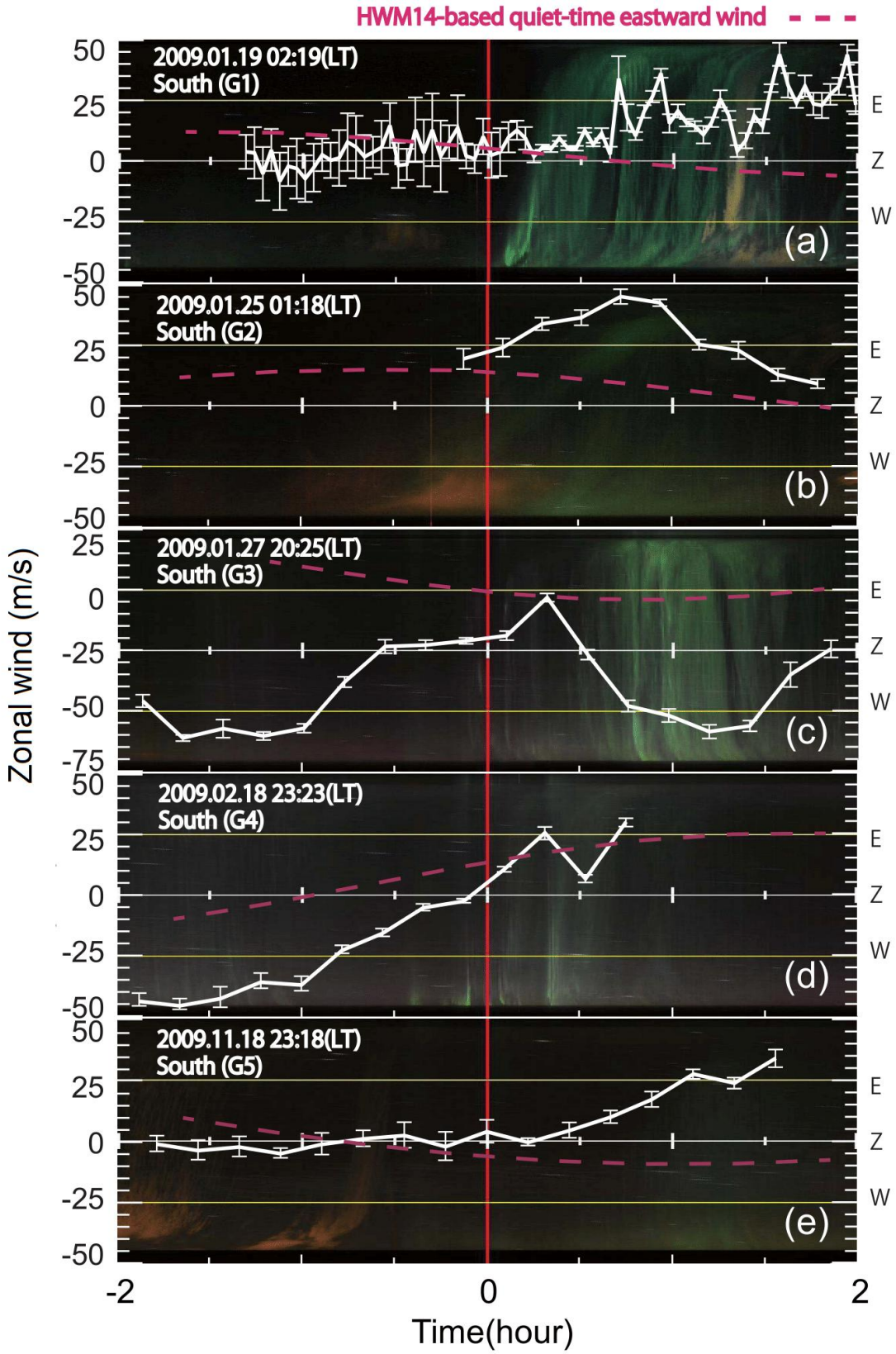

Figure A1 Zonal winds of green-line events at local substorm onsets plotted over east-west cross sections of auroral images, using similar format in Figure 4.6.

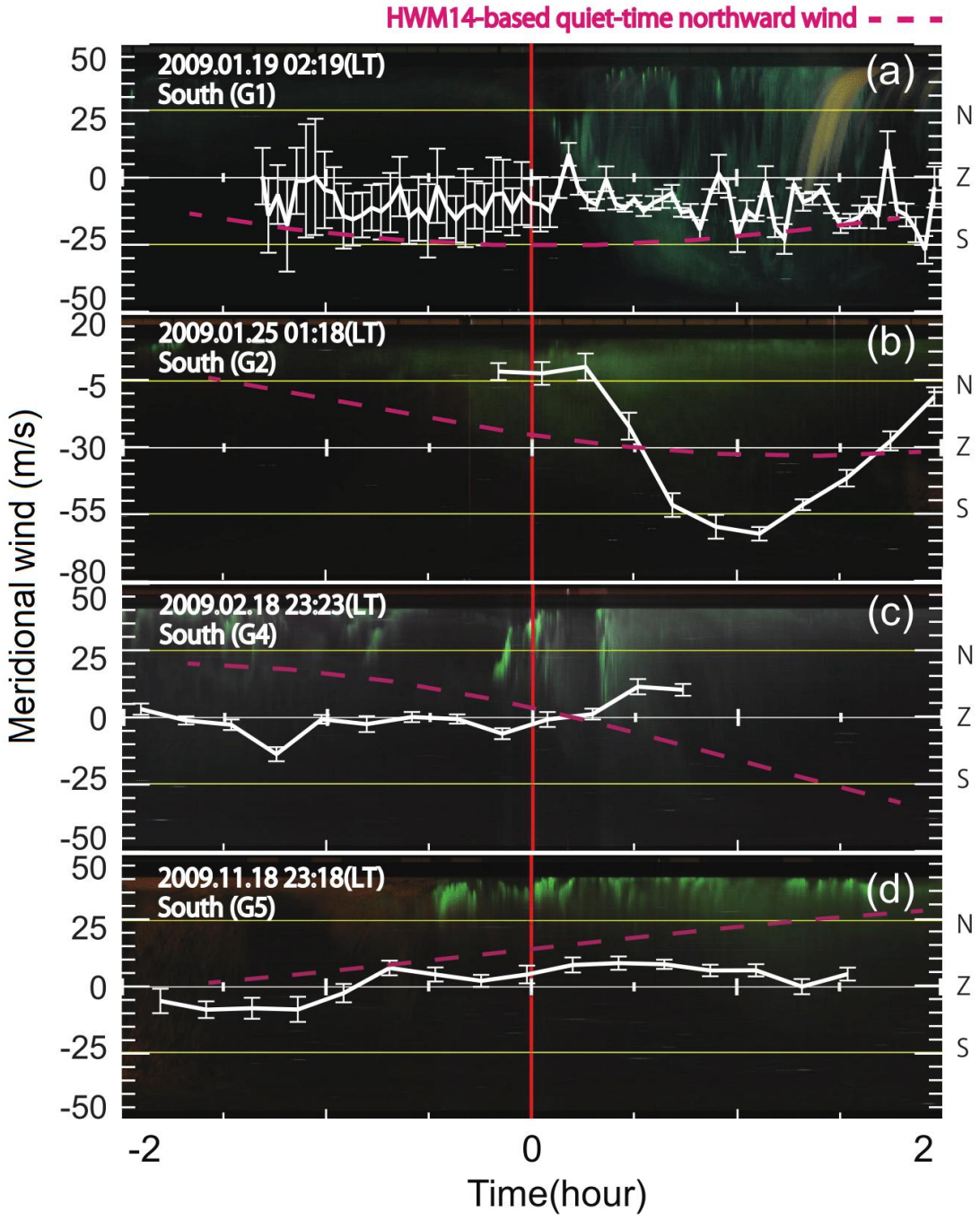

Figure A2 Meridional winds of green-line events at local substorm onsets plotted over north-south cross sections of auroral images, using similar format in Figure 4.7.

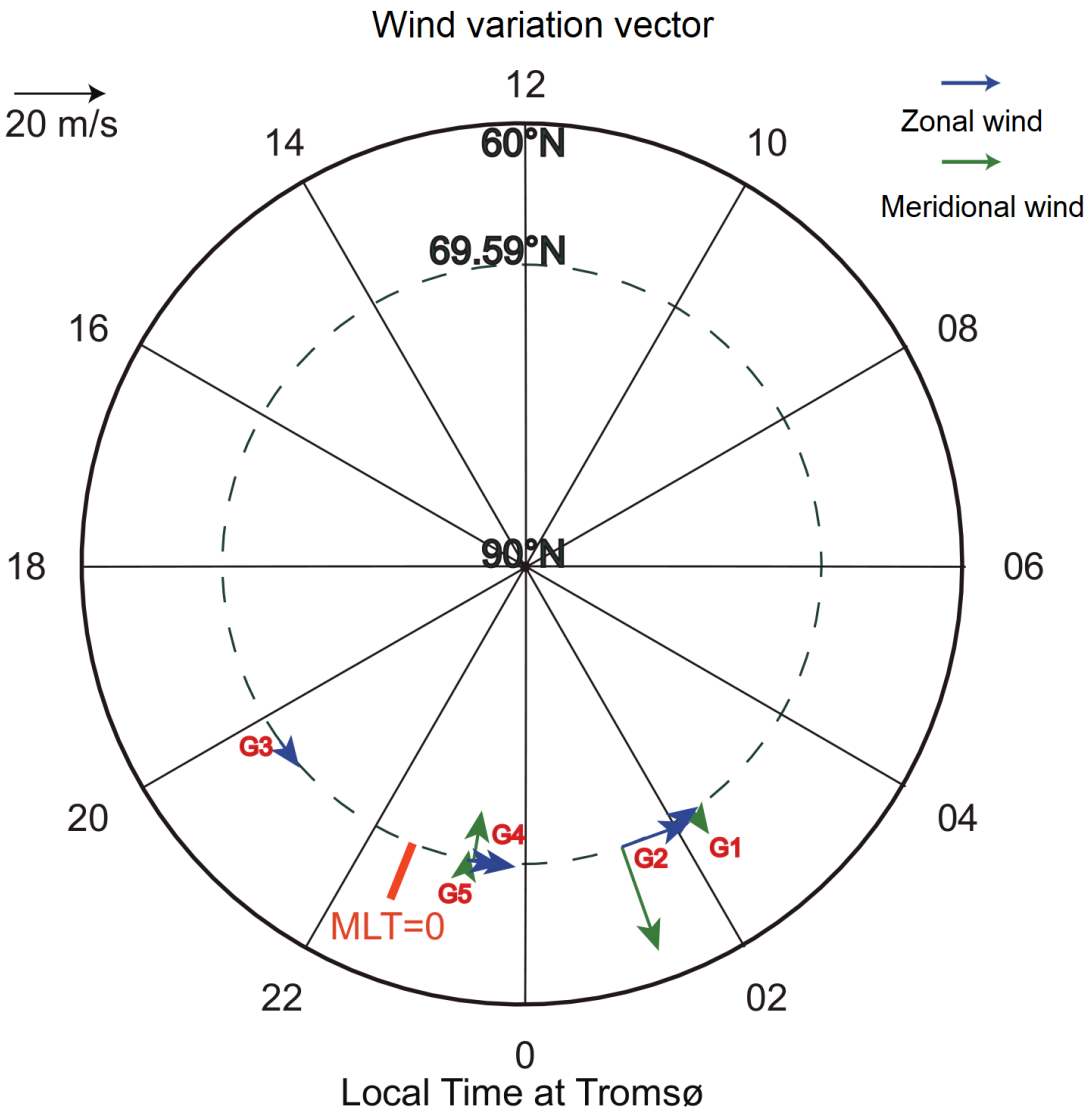

Figure A3 Polar plot of wind variation vectors of green-line events, using similar format in Figure 4.9.

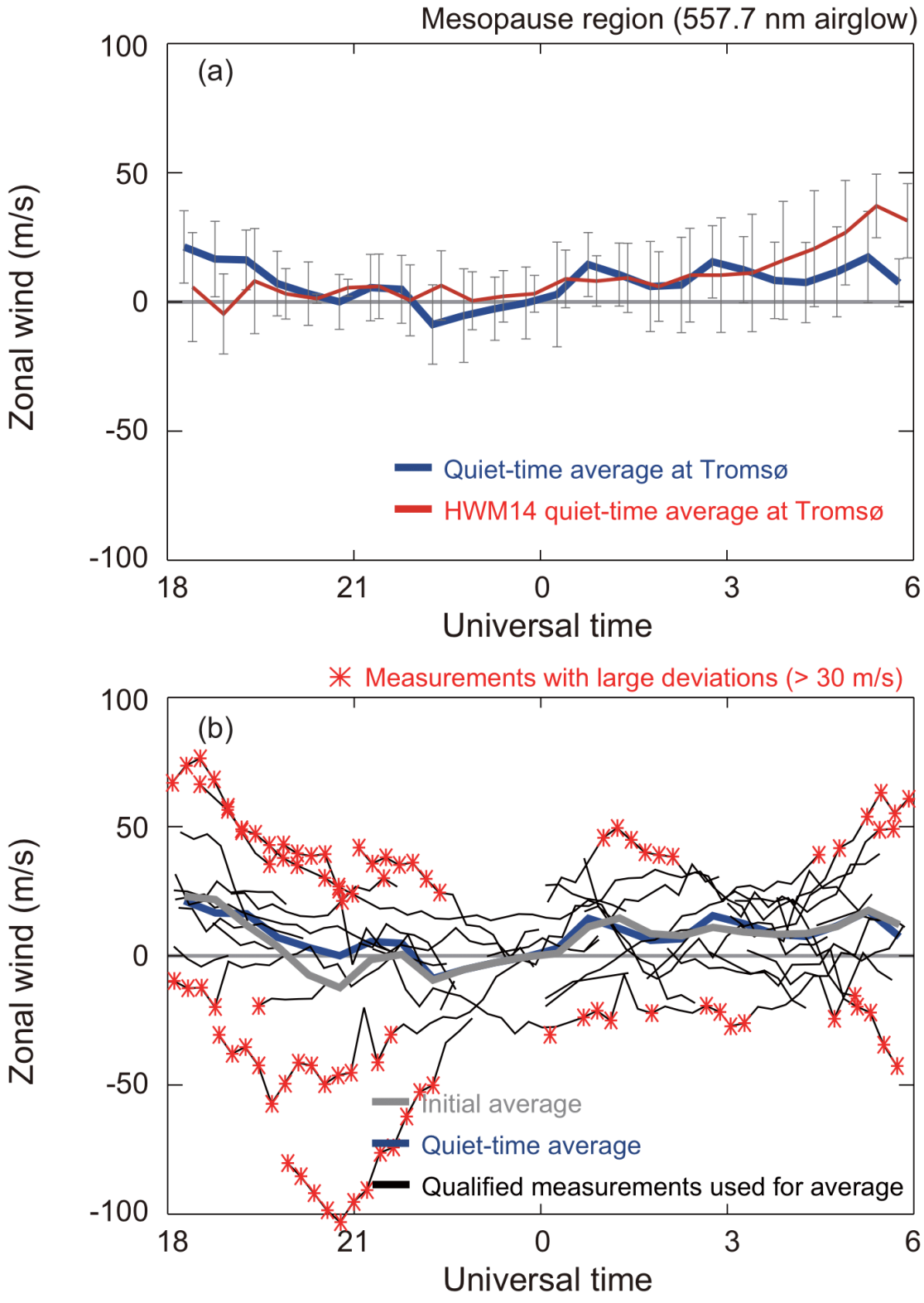

Figure A4 Nightside quiet-time average zonal wind in the mesopause region (90–100 km) at Tromsø, using similar format in Figure 5.2.

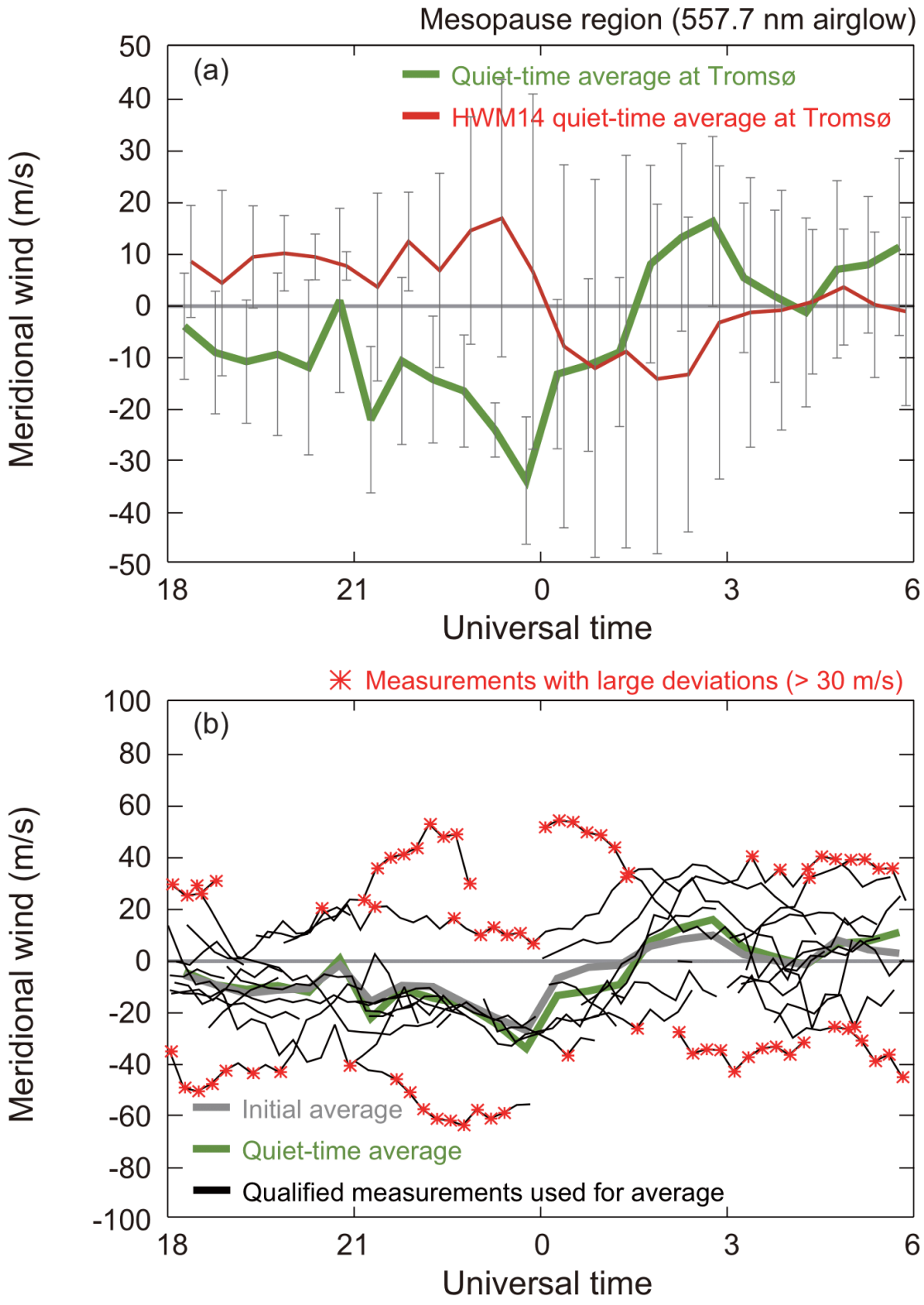

Figure A5 Nightside quiet-time average meridinal wind in the mesopause region (90–100 km) at Tromsø, using similar format in Figure 5.3.

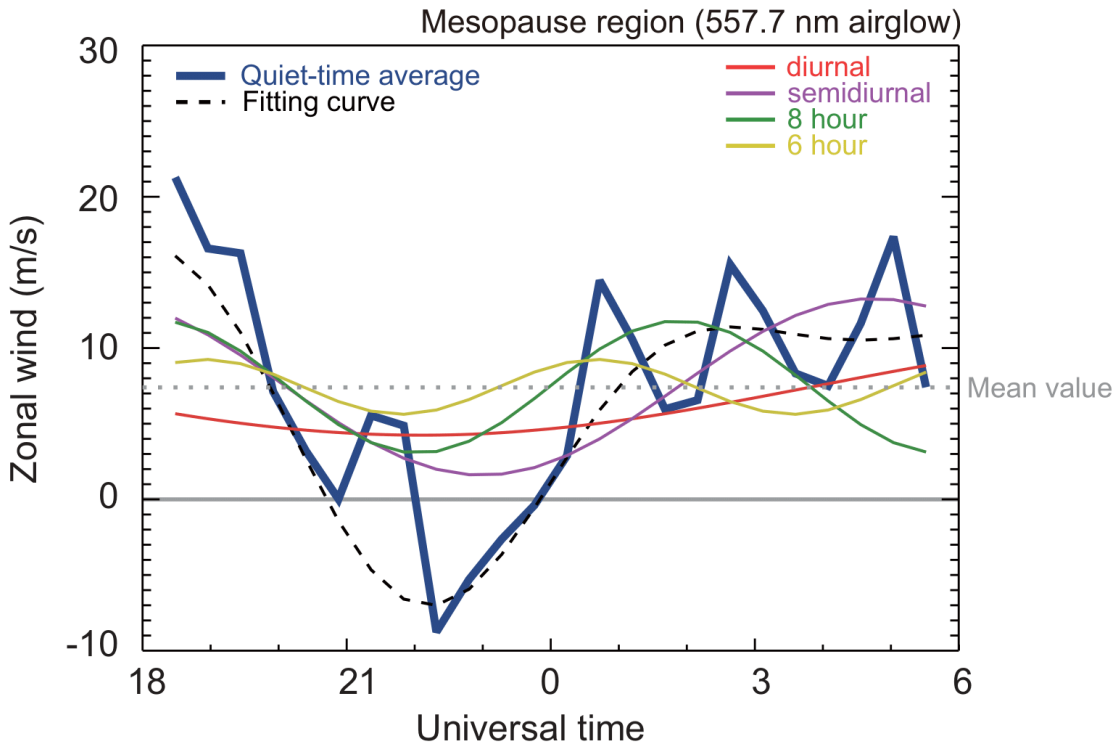

Figure A6 Sinusoidal regression on the nightside quiet-time average zonal wind in the mesopause region at Tromsø. The blue curve shows the observed average zonal wind. The dashed line indicates the sum of all the fitted tidal components.

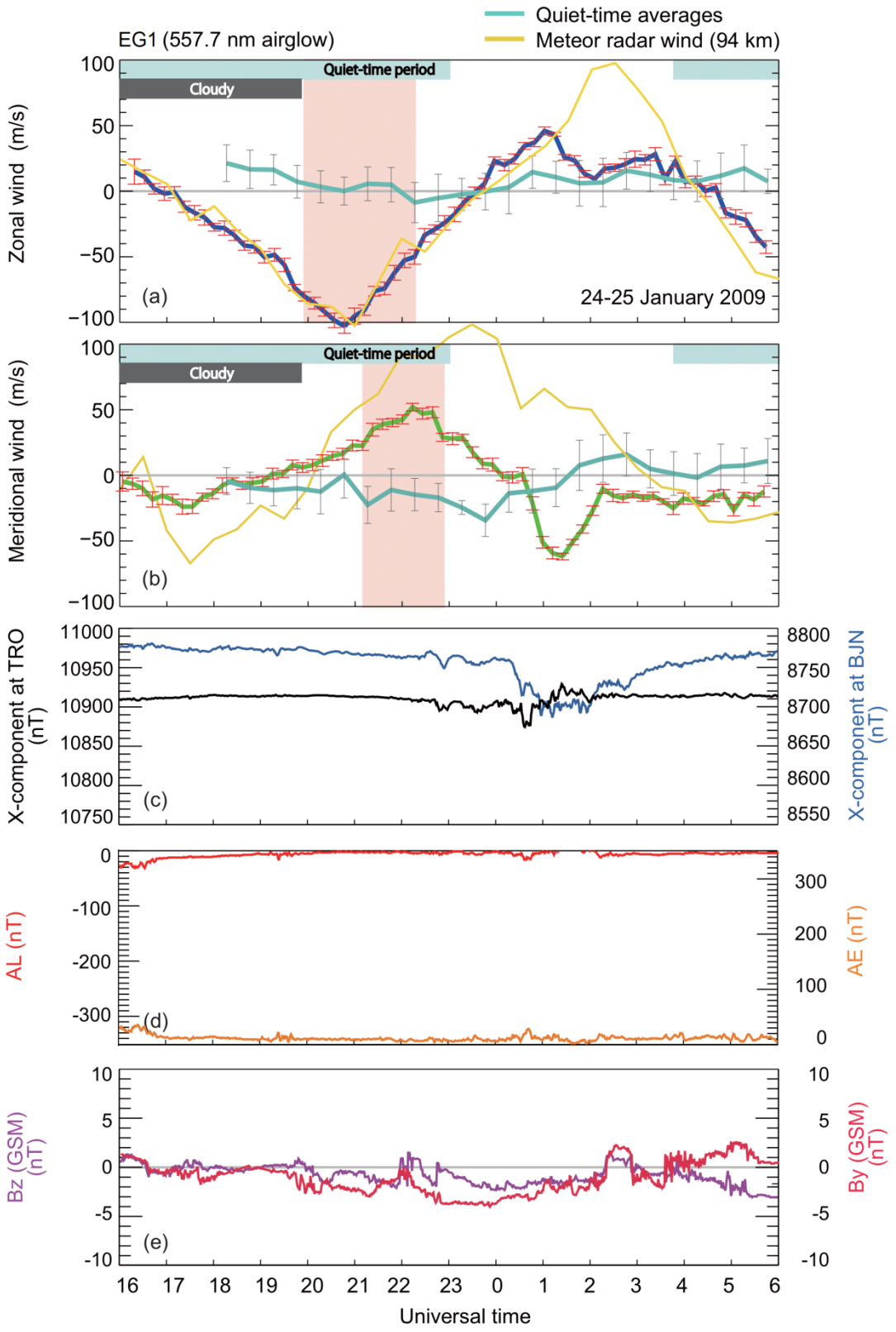

Figure A7 One wind measurement in the mesopause region (event EG1) during geomagnetically quiet times, whose zonal and meridional winds showed large deviations (> 30 m/s) from quiet-time average winds. This plot uses similar format in Figure 5.4.

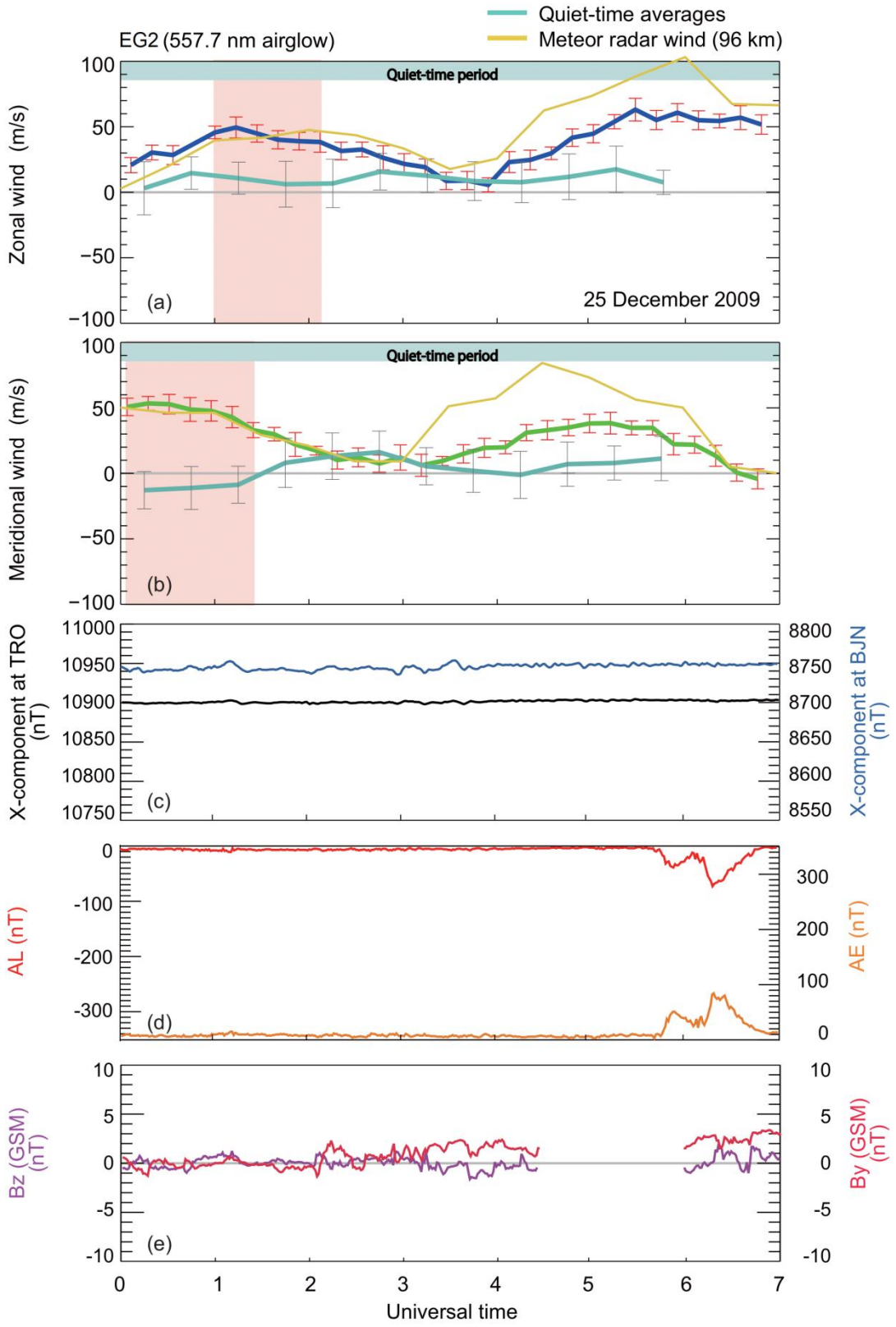

Figure A8 Another wind measurement in the mesopause region (event EG2) during geomagnetically quiet times, whose zonal and meridional winds showed large deviations (> 30 m/s) from quiet-time average winds. This plot uses similar format in Figure 5.4.

Lists of Publications and Presentations

Ⅰ. Publications in Refereed Journals

1. *Xu, H., K. Shiokawa, and D. Früehauff (2017), Statistical analysis of severe magnetic fluctuations in the near-Earth plasma sheet observed by THEMIS-E, Ann. Geophys., 35, 1131–1142, doi:10.5194/angeo-35-1131-2017.
2. *Xu, H., K. Shiokawa, S. Oyama, and Y. Otsuka (2019), Thermospheric wind variations observed by a Fabry-Perot interferometer at Tromsø, Norway, at substorm onsets, Earth Planets Space, 93(71), doi:10.1186/s40623-019-1072-0.
3. *Xu, H., K. Shiokawa, S. Oyama, and S. Nozawa (2019), High-latitude thermospheric wind study using a Fabry-Perot interferometer at Tromsø in Norway: averages and variations during quiet times, Earth Planets Space, 110(71), doi:10.1186/s40623-019-1093-8.

Ⅱ. Presentations

1. Xu, H., and K. Shiokawa, Statistical analysis of magnetic field fluctuations in the near-Earth magnetotail by THEMIS, Japan Geoscience Union Meeting 2015, Chiba, Japan, 24–29 May 2015. (oral presentation)
2. Xu, H., K. Shiokawa, and D. Fruehauff, Statistical analysis of severe magnetic fluctuations in the near-Earth magnetotail observed by THEMIS-E, 2015 American Geophysical Union Fall Meeting, San Francisco, USA, 14–18 December 2015. (poster presentation)
3. Xu, H., K. Shiokawa and D. Fruehauff, Statistical analysis of severe magnetic fluctuations in the near-Earth magnetotail observed by THEMIS-E, Japan Geoscience Union Meeting 2016, Chiba, Japan, 22–26 May 2016. (oral presentation)
4. Xu, H., K. Shiokawa and D. Fruehauff, Severe Magnetic Fluctuations and Their Kinetic Effect on Ion Motion in the near-Earth Magnetotail Observed by THEMIS-E, a Statistical Study, The 140th Society of Geomagnetism and Earth, Planetary and Space Sciences Fall Meeting, Fukuoka, Japan, 19–23 November 2016. (poster presentation)
5. Xu, H., K. Shiokawa, S. Oyama and Y. Otsuka, Thermospheric wind variations

observed by a Fabry-Perot interferometer at Tromsoe, Norway, at substorm onsets, 2016 American Geophysical Union Fall Meeting, San Francisco, USA, 12–16 December 2016. (poster presentation)

6. Xu, H., K. Shiokawa, S. Oyama and Y. Otsuka, Study of thermospheric wind variations at substorm onsets using a Fabry-Perot interferometer at Tromsoe, Norway, Japan Geoscience Union Meeting 2017, Chiba, Japan, 20–25 May 2017. (oral presentation)
7. Xu, H., K. Shiokawa, S. Oyama and Y. Otsuka, Thermospheric wind variations at substorm onset: Multi-event study using a Fabry-Perot interferometer at Tromsoe, Norway, 2017 Coupling, Energetics and Dynamics of Atmospheric Regions Workshop, Keystone, USA, 18–23 June 2017. (poster presentation)
8. Xu, H., K. Shiokawa, S. Oyama and Y. Otsuka, Multi-event study of thermospheric wind variations at substorm onset using an FPI at Tromsoe, Norway, The 142nd Society of Geomagnetism and Earth, Planetary and Space Sciences Fall Meeting, Kyoto, Japan, 15–19 October 2017. (oral presentation)
9. Xu, H., K. Shiokawa, S. Oyama and Y. Otsuka, Multi-event study of high-latitude thermospheric wind variations at substorm onset with a Fabry-Perot interferometer at Tromsoe, Norway, 2017 AGU Fall Meeting, New Orleans, USA, 11–15 December 2017. (poster presentation)
10. Xu, H., K. Shiokawa, and S. Oyama, Study of average thermospheric wind at high latitudes using a Fabry-Perot interferometer at Tromsoe, Norway, Japan Geoscience Union Meeting 2018, Chiba, Japan, 20–24 May 2018. (oral presentation)
11. Xu, H., K. Shiokawa, and S. Oyama, Study of high-latitude quiet-time mean thermospheric winds with a Fabry-Perot interferometer in Tromsoe, Norway, The 144th Society of Geomagnetism and Earth, Planetary and Space Sciences Fall Meeting, Nagoya, Japan, 23–27 November 2018. (oral presentation)
12. Xu, H., K. Shiokawa, and S. Oyama, Study of high-latitude quiet-time thermospheric winds using a Fabry-Perot interferometer at Tromsø, Norway, 2018 American Geophysical Union Fall Meeting, Washington, D.C., USA, 10–14 December 2018. (poster presentation)
13. Xu, H., K. Shiokawa, and S. Oyama, Study of quiet-time high-latitude thermospheric winds using a Fabry-Perot interferometer at Tromsoe: Averages and exceptional events, Japan Geoscience Union Meeting 2019, Chiba, Japan, 26–30

May 2019. (oral presentation)

14. *Xu, H., and K. Shiokawa, Spectral analysis of severe magnetic fluctuations at substorm onset in the near-Earth plasma sheet observed by THEMIS-D and –E, 2019 American Geophysical Union Fall Meeting, San Francisco, USA, 9–13 December 2019. (poster presentation)
15. Borude, R. R., Y. Guo, S. Tanaka, J. Luang-on, T. Tong, H. Xu, B. A. Szasz, Y. Sasai, H. Tanaka, D. Ishihara, K. Tamura, H. Nagano, H. Kaneda, and M. Kutsumizu, Design and Development of Japanese Graphite-based Thermal Straps for Space Missions, The 61th Space Sciences and Technology Conference, Niigata, Japan, 25–27 October 2017. (conference paper)

Ⅲ. Awards

1. Japan Geoscience Union 2016 Outstanding Student Presentation Award: Japan Geoscience Union Meeting 2016, Chiba, Japan, 22–26 May 2016.
2. Japan Geoscience Union 2019 Outstanding Student Presentation Award: Japan Geoscience Union Meeting 2019, Chiba, Japan, 26–30 May 2019.

* Contents in these papers and presentations are included in this thesis.